

Syracuse University

SURFACE

Dissertations - ALL

SURFACE

August 2017

Pattern Formation in Active Nematics

Prashant Mishra
Syracuse University

Follow this and additional works at: <https://surface.syr.edu/etd>



Part of the [Physical Sciences and Mathematics Commons](#)

Recommended Citation

Mishra, Prashant, "Pattern Formation in Active Nematics" (2017). *Dissertations - ALL*. 787.
<https://surface.syr.edu/etd/787>

This Dissertation is brought to you for free and open access by the SURFACE at SURFACE. It has been accepted for inclusion in Dissertations - ALL by an authorized administrator of SURFACE. For more information, please contact surface@syr.edu.

Abstract

This thesis presents analytical and numerical studies of the nonequilibrium dynamics of active nematic liquid crystals. Active nematics are a new class of liquid crystals consisting of elongated rod-like units that convert energy into motion and spontaneously organize in large-scale structures with orientational order and self-sustained flows. Examples include suspensions of cytoskeletal filaments and associated motor proteins, monolayers of epithelial cells plated on a substrate, and bacteria swimming in a nematic liquid crystal. In these systems activity drives the continuous generation and annihilation of topological defects and streaming flows, resulting in spatio-temporal chaotic dynamics akin to fluid turbulence, but that occurs in a regime of flow of vanishing Reynolds number, where inertia is negligible. Quantifying the origin of this nonequilibrium dynamics has implications for understanding phenomena ranging from bacterial swarming to cytoplasmic flows in living cells.

After a brief review (Chapter 2) of the properties of equilibrium or passive nematic liquid crystals, in Chapter 3 we discuss how the hydrodynamic equations of nematic liquid crystals can be modified to account for the effect of activity. We then use these equations of active nemato-hydrodynamics to characterize analytically the nonequilibrium steady states of the system and their stability. We supplement the analytical work with numerical solution of the full nonlinear equations for the active suspension and construct a phase diagram that identifies the various emergent patterns as a function of activity and nematic stiffness. In Chapter 4 we compare results obtained with two distinct hydrodynamic models that have been employed in previous studies. In both models we find that the chaotic spatio-temporal dynamics in the regime of fully developed active turbulence is controlled by a single active scale determined by the balance of active and elastic stresses. This work provides a unified understanding of apparent discrepancies in the previous literature and demonstrate that the essential physics is robust to the choice of model. Finally, in Chapter 5 we examine the dynamics of a compressible active nematic on a substrate. When frictional damping dominates over viscous dissipation, we eliminate flow in favor of active stresses to obtain a minimal model with renormalized elastic constants driven negative by activity. We show that spatially inhomogeneous patterns are selected via a mechanism analogous to that responsible for modulated phases at an equilibrium Lifshitz point.

Pattern Formation in Active Nematics

by

Prashant Mishra

B.S., Indian Institute of Science Education & Research, Mohali, 2012

M.S., Indian Institute of Science Education & Research, Mohali, 2012

DISSERTATION

submitted in partial fulfillment of the requirements for the degree of

Doctor of Philosophy in Physics

Syracuse University

August 2017

Copyright © Prashant Mishra 2017

All Rights Reserved

Acknowledgements

I would like to express my gratitude to my adviser Prof. M. Cristina Marchetti who guided me through my PhD research and introduced me to many interesting topics in Soft Condensed Matter Physics. I am also thankful to Prof. Mark J. Bowick for guidance and support he provided at various stages of my research. I would also like to thank the other members of the defense committee: Peter R. Saulson, Alan Middleton, Joseph D. Paulsen, Jennifer M. Schwarz and Yi Wang for taking time out of their busy schedules to read and critique my work. I am grateful to the Syracuse University Soft-Matter program, faculties and staff specifically Michelle and Patty who helped me time to time in my research with their continuous feedback and support.

It has been a pleasure to share my office with Adam and Mike and I thank them for a productive and supportive environment around. I would like to specially mention my friend, flatmate and colleague, Kazage for numerous academic and non-academic advises and discussions. I also want to thank my parents and wife Pooja for helping me at various stages of my life and guiding me in making crucial decisions. Last but not the least, I thank my friends Raghav, Sourav, Nouman, Anam, Ogan, Nikhil, Subhra and Twinkle in no particular order for keeping me sane with their continuous support and all the good times we spent together.

*Dedicated to my parents whose relentless sacrifice made
all I have possible*

Contents

Abstract	i
Acknowledgements	iv
List of Figures	ix
List of Tables	xvi
1 Introduction	1
1.1 Introduction	1
1.2 Classification of Active Systems	2
1.2.1 Classification based on Symmetry	3
1.2.2 Classification based on forces on the medium	4
1.2.3 Classification Based on damping	4
1.3 Experimental motivation	6
1.4 Thesis Outline	9
2 Passive Nematic Liquid Crystals	11
2.1 Introduction	11
2.2 Order parameter tensor	13
2.3 Landau free energy	14
2.4 Topological defects	17
2.5 Nematic-hydrodynamics	20
2.5.1 Dynamics of density	20
2.5.2 Dynamics of momentum density	21
2.5.3 Dynamics of order parameter tensor	21
3 Hydrodynamics of active nematics	23
3.1 Introduction	23
3.2 Active nematodynamics	24
3.2.1 Governing Equations	24
3.2.2 Linear Stability	27
3.2.3 Dimensionless Units and Numerical Methods	28

3.3	Dynamics of an isolated disclination	29
3.4	Annihilation dynamics of defect pairs	37
3.5	Defect proliferation	43
3.5.1	Relaxation Oscillations	44
3.5.2	Wall formation and unzipping	46
3.5.3	Turbulence	48
3.6	Discussion and Conclusions	51
Appendix A		54
A.1	Active backflow of $+1/2$ disclinations	54
A.2	Active backflow of $-1/2$ disclinations	56
4	Correlation Lengths in active nematics	58
4.1	Introduction	58
4.2	Models	61
4.2.1	Numerical details	65
4.3	Characteristic length scales	66
4.3.1	Model length scales	67
4.3.2	Emergent length scales	68
4.3.3	Scaling hypothesis	69
4.3.4	Form of the scaling function	71
4.4	Results	72
4.4.1	Correlation lengths	73
4.4.1.1	Extensile active matter	74
4.4.1.2	Contractile active matter.	76
4.4.2	Kinetic energy and enstrophy	76
4.5	Discussion	79
4.6	Acknowledgment	80
Appendix B		81
B.1	Flow-aligning Parameter	81
5	Active Nematics on a Substrate	84
5.1	Introduction	84
5.2	Active Nematics on a Substrate	87
5.3	Linear stability of homogeneous states and “multicritical point”	92
5.3.1	Isotropic state - $r < 1$	92
5.3.2	Ordered state - $r > 1$	95
5.4	Numerical results: kink walls, defect alignment and turbulence	98
5.5	Comparison to previous work	104
5.6	Conclusion and Discussion	106
5.7	Acknowledgments	109
Appendix C		110
C.1	Overdamped nematic in $2d$: General equations	110

C.2 Linear Modes for general flow coupling parameters	112
Bibliography	116
6 CV	128

List of Figures

1.1	Collective motion in (a) Microtubules bundles [1] at subcellular scale, (b) myxobacteria colony [2] at micro scale, and (c) fish school at macro scale.	2
1.2	(a) Polar active particle, (b) apolar active particle, (c) self propelled rod, (d) polar order of polar particles, (e) nematic order of apolar particles, (f) nematic order of polar particles.	3
1.3	(a) Actomyosin behaving like contractile system, (b) microtubule-kinesin bundle behaving like extensile system.	4
1.4	(a) Disclinations forming in MT bundles due to nematic symmetry of MT bundle in Dogic's group experiments [3, 4], (b) Microtubule-Kinesin polar rods leading to aster and vortex formation in Nedelec <i>et. al.</i> [5] due to polar symmetry in an individual MT.	6
1.5	(A) Microtubule-Kinesin polar rods leading to aster formation in Nedelec <i>et. al.</i> [5], (B) microtubule-kinesin bundle formation due to PEG in Dogic's group experiments [3, 4].	9
2.1	(a) Nematic LCs in an isotropic state with each unit having random orientation, (b) Nematic LCs in nematic state with average ordering in the x direction.	12
2.2	The angle θ^i between molecular axis and the director \mathbf{n}	14
2.3	(a) Twist deformation, (b) Bend deformation, (c) Splay deformation.	16
2.4	(a) -1 defect structure ($\oint d\theta = -2\pi$) or asters in polar system , (b) +1 defect structure ($\oint d\theta = 2\pi$) or vortices in polar systems, (c) +1/2 defect structure ($\oint d\theta = \pi$) in nematic suspension, (d) -1/2 defect structure ($\oint d\theta = -\pi$) in nematic suspension. The green clockwise circle signifies the direction in which the loop integration is performed.	18

3.1	Schematic representation of the region where an active nematic is linearly unstable to splay (green) and to bend (gray) fluctuations in the plane of the alignment parameter λ and the activity $\alpha = c_0^2 \alpha_2$. The unstable regions are bounded by the critical activity given in Eq. (3.5). Flow tumbling extensile nematic with $ \lambda < 1$ are unstable to bend when active stresses are extensile ($\alpha < 0$) and to splay when active stresses are contractile ($\alpha > 0$). Conversely, strongly flow aligning ($ \lambda \gg 1$) are unstable to splay when active stresses are extensile ($\alpha < 0$) and to bend when active stresses are contractile ($\alpha > 0$).	28
3.2	Example of a $+1/2$ (left) and $-1/2$ (right) disclination. The solid red lines are tangent to the director field $\mathbf{n} = (\cos \theta_d, \sin \theta_d)$ with $\theta_d = k\phi$ and $k = \pm 1/2$. The background shows the active backflow associated with the disclinations and obtained by solving the Stokes equation (3.12) with no-slip boundary conditions on a circle (dashed black line). The intensity of the background color is proportional to the magnitude of the flow velocity. The white streamlines are given by Eq. (3.15).	29
3.3	Snapshots of a disclination pair shortly after the beginning of relaxation. (Top) Director field (black lines) superimposed on a heat map of the nematic order parameter and (bottom) flow field (arrows) superimposed on a heat map of the concentration for an extensile system with $\alpha = -0.8$ (a),(c) and a contractile system with $\alpha = 0.8$ (b),(d). In the top images the color denotes the magnitude of the nematic order parameter S relative to its equilibrium value $S_0 = \sqrt{1 - c^*/c_0} = 1/\sqrt{2}$. In the bottom images the color denotes the magnitude of the concentration c relative to the average value $c_0 = 2c^*$. Depending on the sign of α , the backflow tends to speed up ($\alpha > 0$) or slow down ($\alpha < 0$) the annihilation process by increasing or decreasing the velocity of the $+1/2$ disclination. For α negative and sufficiently large in magnitude, the $+1/2$ defect reverses its direction of motion (c) and escapes annihilation.	38
3.4	Schematic representation of the effective attractive/repulsive interaction promoted by the active backflow. Depending on the sign of the active stress α , $+1/2$ disclinations self-propel in the direction of their “tail” (contractile) or “head” (extensile). Based on the mutual orientation of the defects, this can lead to an attractive or repulsive interaction.	40
3.5	Defect pair production in an active suspension of microtubules and kinesin (top) and the same phenomenon observed in our numerical simulation of an extensile nematic fluid with $\gamma = 100$ and $\alpha = -2$. The experimental pictures are reprinted with permission from T. Sanchez et al., Nature (London) 491, 431 (2012). Copyright 2012, Macmillan.	40

3.6	Defect trajectories and annihilation times obtained from a numerical integration of Eqs. (3.1) for various γ and α values. (a) Defect trajectories for $\gamma = 5$ and various α values (indicated in the plot). The upper (red) and lower (blue) curves correspond to the positive and negative disclination, respectively. The defects annihilate where the two curves merge. (b) The same plot for $\gamma = 10$. Slowing down the relaxational dynamics of the nematic phase increases the annihilation time and for $\alpha = -0.8$ reverses the direction of motion of the $+1/2$ disclination. (c) Defect separation as a function of time for $\alpha = 0.8$ and various γ values. (d) Annihilation time normalized by the corresponding annihilation time obtained at $\alpha = 0$ (i.e., t_a^0). The line is a fit to the model described in the text.	42
3.7	Phase diagram showing the various flow regimes of an active nematic obtained by varying activity α and rotational friction γ for both contractile ($\alpha > 0$) and extensile ($\alpha < 0$) systems. The dashed lines bounding the region where the homogeneous ordered state (H) is stable are the boundaries of linear stability given in Eq. (3.5). With increasing activity, the system exhibits relaxation oscillations (O), non-periodic oscillations characterized by the formation and unzipping of walls (W), and turbulence (T).	44
3.8	Dynamical states obtained from a numerical integration of Eqs. (3.1) with $\gamma = 20$ and various values of activity for an extensile system. (a) Average nematic order parameter versus time. The black line for $\alpha = -0.3$ identifies the relaxation oscillations regime with the labels (b), (c) and (d) marking the times corresponding to the snapshots on the top-left panel. The red line for $\alpha = -0.8$ indicates the non-periodic oscillatory regimes characterized by the formation of walls (e) and the unzipping of walls through the unbinding of defect pairs: (f) and (g). The symbols \bullet and \triangle mark the positions of $+1/2$ and $-1/2$ disclinations respectively. The blue line for $\alpha = -1.2$ corresponds to the turbulent regime in which defects proliferate: (h), (i) and (j). In all the snapshots, the background colors are set by the magnitude of the vorticity ω and the order parameter S rescaled by the equilibrium value $S_0 = 1/\sqrt{2}$, while the solid lines indicate velocity (top) and director field (bottom). Movies displaying the time evolution of each state are included as the Supplementary Material.	45
3.9	A magnification of the snapshot of Fig. 3.8f, showing the creation of a $+1/2$ (\bullet) and a $-1/2$ (\triangle) defect pair along a wall or $\alpha = -0.8$ and $\gamma = 20$. The black arrows indicate the flow velocity, while the background color is related with the local vorticity. The wall is also the boundary between a pair of vortices of opposite circulation. The flow field of opposite-signed vortices adds at the wall, yielding a region of high shear that promotes defect unbinding.	48

3.10	Defects area fraction $N\pi a^2/L^2$ as a function of the active Ericksen number $\text{Er}_\alpha = \alpha\gamma L^2/(\eta K)$ for contractile (symbols in red tones) and extensile (symbols in blue tones) systems. In both cases the area fraction saturates when the activity increase is compensated by a drop of the order parameter which effectively reduces the injected active stress.	49
4.1	Nematic correlation function C_θ defined in (4.12) obtained from Model II for an extensile system in the regime of spatio-temporally chaotic behavior for $(\ell_Q/L)^2 = 5 \times 10^{-6}$ and activities in the range $\alpha/G_Q = -0.4$ (red) to -12.8 (blue). Inset: Unscaled data, demonstrating our definition $C_\theta(\ell_\theta) = \frac{1}{2}$. Main: the same data collapse onto a single curve when rescaled by the active length ℓ_α	70
4.2	Results from Model II for the nematic correlation length ℓ_θ (empty symbols) and defect spacing ℓ_d (filled symbols) as functions of the dimensionless activity $ \alpha /G_Q$ for an extensile nematic ($\alpha < 0$). (a) Lengthscales vs $ \alpha $ for various values of the microscopic correlation length: $(\ell_Q/L)^2 = 2 \times 10^{-6}$ (red circles), 5×10^{-6} (green squares), and 1×10^{-5} (blue triangles). The remaining parameter values are given in Table 4.2. At small activity we see saturation due to finite size effects. (b) The curves collapse when ℓ_θ and ℓ_d are rescaled by ℓ_Q . In both frames the black dashed lines show $(\alpha /G_Q)^{-1/2}$. In Fig. 4.2a we also mark the power law $(\alpha /G_Q)^{-1/4}$ obtained by Thampi <i>et al.</i> as a purple dot-dashed line. (c,d) Representative snapshots of $(n_x n_y)^2$ for (c) $ \alpha /G_Q = 0.1$ and (d) $ \alpha /G_Q = 6.4$. We set $(\ell_Q/L)^2 = 1 \times 10^{-5}$ in both snapshots. Defects of topological charge $\pm 1/2$ are identified by green dots (+) and red squares (-). For videos see supplementary material.	72
4.3	Results from Model I for the nematic correlation length ℓ_θ (empty symbols) and defect spacing ℓ_d (filled symbols) as functions of the dimensionless activity $ \alpha \gamma/G_Q\eta$ for an extensile nematic ($\alpha < 0$). (a) Length scales vs $ \alpha $ for various values of the viscosity ratio: $\gamma/\eta = 10$ (red circles), 20 (green squares), 30 (blue triangles), and 40 (magenta diamonds). The values of the other parameters are given in Table 4.2. The black dashed lines denote a slope of $-1/2$. (b,c) Representative snapshots of the alignment tensor for $\eta/\gamma = 20$ in (b) the low activity regime ($ \alpha /G_Q = 20$) with low defect density and (c) the high activity regime ($ \alpha /G_Q = 100$) with high defect density. The color scale represents the magnitude S of the order parameter and the black lines denote the local orientation of the director field. Topological defects with charge $\pm 1/2$ are shown as green dots (+) and red squares (-).	73

4.4	Velocity (ℓ_v , filled symbols) and vorticity (ℓ_Ω , empty symbols) correlation lengths, normalized by ℓ_Q for (a) an extensile ($\alpha < 0$) and (b) a contractile ($\alpha > 0$) system. We explore several values of the viscosity ratio: $\gamma/\eta = 10$ (red circles), 20 (green squares), 30 (blue triangles), and 40 (magenta diamonds). Frame (c) shows the defect spacing ℓ_d (filled symbols) and the director correlation length ℓ_θ (empty symbols) for a contractile ($\alpha > 0$) active nematic as a function of $\alpha\gamma/G_Q\eta$ for the same set of values of γ/η . All lengths scale as $(\alpha\gamma/G_Q\eta)^{-1/2}$. The black dashed lines represent a slope of $-1/2$.	75
4.5	Scaling of kinetic energy (frames (a) and (c)) and enstrophy (frames (b) and (d)) with activity for both Models I and II. The left figure displays the results obtained from Model I by varying the viscosity ratio γ/η as shown. The right figure displays the results obtained from Model II by varying the nematic correlation length ℓ_Q/L . The inset of frame (d) shows the scaling collapse of the kinetic energy when plotting v_{rms}^2/ℓ_Q^2 against activity. In frame (d), data is shown for two numerical resolutions: dashed lines for $N = 1024$, and solid lines for $N = 2048$.	77
5.1	Phase diagram in the $(r, \tilde{\alpha})$ plane obtained by linear stability analysis. The vertical black line at $r = 1$ is the mean-field transition between the disordered and ordered nematic states. The disordered state ($r < 1$) becomes unstable via an isotropic instability at the value of activity given in Eq. (5.12) (orange line). The ordered state ($r > 1$) first becomes unstable to the growth of bend fluctuations of the director field (blue line, Eq. (5.20) for $\psi = 0$). We also show the lines corresponding to the change in sign of the growth rate of splay fluctuations of the director (dark green line, Eq. (5.20) for $\psi = \pi/2$) and the magnitude of the order parameter (purple line, Eq. (5.22)). These additional instability lines correlate with the onset of more complex spatial structures with increasing activity, as suggested by the shading of the various regions, and eventually the onset of active turbulence (no shading). All the instability boundaries meet at a multicritical point where the uniform isotropic, uniform nematic and modulated phases coexist. Inset: the dispersion relation Ω_I (Eq. (5.11)) that controls the growth of order parameter fluctuations for $r < 1$ as a function of wavevector for three values of $ \tilde{\alpha} = 10, 13.26, 17$ (from bottom to top). At the transition only one critical mode $q = q_c^I$ is unstable. Above the transition the unstable modes lie in a band $q_-^I < q < q_+^I$.	89

5.2	Numerical phase diagram and snapshots of the various steady states for $\tilde{\kappa} = 10$ and $\lambda = 1.5$. <i>Left panel:</i> Numerical phase diagram in the $(r, \tilde{\alpha})$ plane. The vertical black line at $r = 1$ is the mean-field I-N transition from the isotropic ($r < 1$) to the nematic ($r > 1$) state. The symbols refer to various steady state configurations obtained by numerical solution of the nonlinear equations and quantified as described in the text. Open symbols are used for states with $r < 1$ and filled symbols for states with $r > 1$, as follows: uniform isotropic state (open black diamonds), uniform nematic (filled black diamonds), kink walls with defects (green stars), kink walls with no defects (blue circles), bend modulations (filled magenta triangles), turbulent state (red squares). The solid lines denote the various linear stability boundaries described in Fig. 5.1. Figures (a-f) show typical snapshots of the various states: kinks walls with (a and movie S1 in SI) and without (b and movie S2 in SI) defects for $r < 1$; (c and movie S3 in SI) bend modulations, (d and movie S4 in SI) kink walls with defects, (e and movie S5 in SI) kink walls with no defects, and (f and movie S6 in SI) turbulent state. Snapshots (c-f) are for $r > 1$. The color scale describes the magnitude of the order parameter S (the mean field value is $S_0 = 0.78$ in (c) to (f)). The black lines denote the direction of the director. Each snapshot also shows a blow up of the structure in the upper right corner. Disclination defects, when present, are denoted by green filled triangles ($-1/2$) and black filled circles ($+1/2$), with a short black solid line indicating the tail of the comet-like $+1/2$ defect. In the extensile case considered here the $+1/2$ defects move in the direction of the black dot.	93
5.3	Numerical phase diagram in the $(\tilde{\kappa}, \tilde{\alpha})$ plane for $r = 2$. The lines are the linear stability boundaries discussed in section 5.3: bend instability (blue line), splay instability (orange line), instability of magnitude of order parameter (red line). The various symbols have same meaning as in Fig. 5.2.	98

5.4	<p>(a) $\langle S \rangle$ as a function of activity. The top three curves correspond to $r > 1$ and show the decay of $\langle S \rangle$ with increasing activity from its mean-field value $S_0 = \sqrt{(r-1)/r}$ at zero activity. The bottom three curves correspond to $r < 1$, where $\langle S \rangle$ ramps up sharply from its low activity value of zero at the onset α_{cI} of the linear instability. The curves through the data are a guide to the eye. (b) The evolution with activity of the two measure of nematic order $\langle Q \rangle$ (red crosses) and $\langle S \rangle$ (blue squares) for $r = 4$, $\tilde{\kappa} = 10$ and $\lambda = 1.5$. The shading denotes the various regimes as estimated from the numerics. At low activity the system is in a uniform nematic state (light green) and $\langle Q \rangle = \langle S \rangle = S_0 = 0.86$. In the region of bend modulations (white) $\langle S \rangle$ remains close to its maximum value, while $\langle Q \rangle$ drops sharply, remaining close to zero in all subsequent regimes. The slight increase of $\langle Q \rangle$ near the transition from KW to turbulence reflects the alignment of KW in this region. (c) Number of defects as a function of time for six values of activity for $r = 4$: $\tilde{\alpha} = 6, 7$, corresponding to KW with defects (green curves), $\tilde{\alpha} = 20, 30$, corresponding to defect-free KW (blue curves), and $\tilde{\alpha} = 40, 50$, corresponding to the turbulent state (red curves).</p>	100
5.5	<p>(a) Profiles of the angle θ of the director with the direction of mean order for <i>bend</i> (blue curve, $\tilde{\alpha} = 3$) and <i>kink walls</i> (red curve, $\tilde{\alpha} = 20$), $\tilde{\kappa} = 10$ and $\lambda = 1.5$. The director profiles for both deformations are shown at the top of the figure. (b) Width of kink walls versus activity for $r = 2, 3, 4$, $\tilde{\kappa} = 10$ and $\lambda = 1.5$. The dashed line has slope $-1/2$.</p>	101
5.6	<p>Snapshots at (a) $t = 92\tau$, (b) $t = 143\tau$ and (c) $t = 170\tau$ showing the transient nematic alignment of defects for $r = -1$, $\tilde{\alpha} = 14$, $\tilde{\kappa} = 10$ and $\lambda = 1.5$(see movie S7 in SI). These structures are obtained for values of activity close to the boundary of linear stability of the uniform mean-field isotropic state, which is at $\alpha_{cI} = 13.2$ for the parameters used here. The defects are highlighted using the same convention as described in the caption of Fig. 5.2.</p>	103
B1	<p>Polar plot of the growth rate of the most unstable mode (this is the mode that for $\psi = 0, \pi/2$ describes fluctuations in the director $\sim \Delta Q_{xy}$) as a function of the angle ψ for fixed $q = 0.7$, chosen such that all directions are unstable, and extensile systems. For both, incompressible (blue curve) and compressible (red curve) flows, the growth rate is largest for $\psi = 0, \pi$, corresponding to bend fluctuations. The parameter values used for the figure are $\lambda_1 = 1.5$, $\lambda_3 = 1.5$, $\lambda_R = 1$, $\lambda_C = 1$ and $\tilde{\alpha} = -20.0$, with units chosen as in the main text.</p>	115

List of Tables

4.1	Summary of the various model parameters and their dimensions. The choices for mass $[M]$ (or equivalently stress $[\sigma] = [M][L]^{d-2}[T]^{-2}$), length $[L]$ and time $[T]$ in each model are also indicated.	64
4.2	Summary of the dimensionless parameters and their values in both models. The velocity scale $V = \ell_Q G_Q / \eta$ in our units.	66

Chapter 1

Introduction

1.1 Introduction

Understanding the mechanical and statistical properties of “active matter” [2] has been a topic of great interest for last few decades in the community of condensed matter physics. Active systems are composed of self-driven units, active particles. Each unit converts stored free energy into systematic movement. Active particles are often elongated and their direction of self-propulsion is set by their own anisotropy, rather than fixed by an external field. Elongated active particles can order in states with long-range orientational order, forming “living liquid crystal” phases. Examples of such active systems that can exhibit orientational order include bacterial suspensions, the cell cytoskeleton, and in-vitro suspension of cytoskeleton filament and associated motor proteins. The length scales of active matter range from the sub-micron scale to the macro scale, as shown in Fig 1.1. There are many phenomena occurring in active matter at all scales that are still a mystery to us. Due to the complex structure and far-from-equilibrium nature of active systems, it is hard to model them in terms of a small number of physical

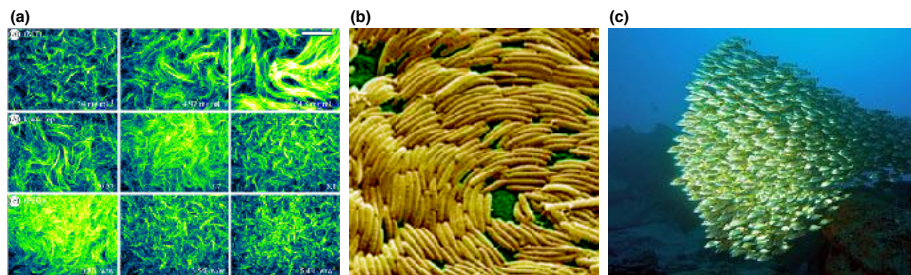


FIGURE 1.1: Collective motion in (a) Microtubules bundles [1] at subcellular scale, (b) myxobacteria colony [2] at micro scale, and (c) fish school at macro scale.

quantities. Nonetheless, global principles, such as conservation laws and symmetries, constrain the possible dynamical behavior of active matter [2].

It is well established that the dynamics of collective systems can be very different from that of an individual unit. Even collections of multiple passive units can create system-wide ordering in the process of finding a stable state, e.g., atoms forming liquids or solids. External forces at boundaries, such as a shear stress, can drive these passive systems out of equilibrium but as soon as the constraints are relaxed, passive systems go back to their equilibrium state. Active matter, in contrast, is maintained out of equilibrium by a sustained energy input. Novel effects that have been predicted theoretically or observed in simulations and experiments include spontaneous laminar flow [6, 7, 8], large density fluctuations [9, 10, 11], unusual rheological properties [12, 13, 14], excitability [15, 16], low Reynolds number “turbulence” [15, 16, 17, 18, 19, 20, 21] and flocking [22, 23, 24, 25].

1.2 Classification of Active Systems

Active systems can be classified according to the symmetry of individual units and the type of interaction with the surrounding medium.

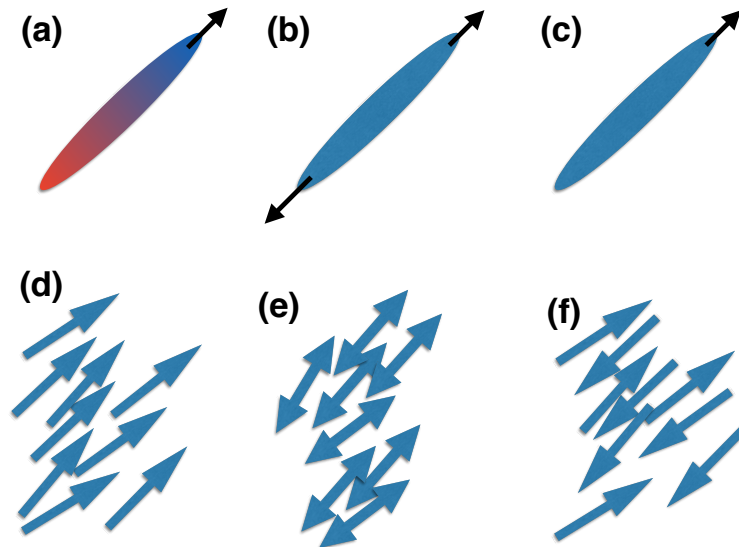


FIGURE 1.2: (a) Polar active particle, (b) apolar active particle, (c) self-propelled rod, (d) polar order of polar particles, (e) nematic order of apolar particles, (f) nematic order of polar particles.

1.2.1 Classification based on Symmetry

Ordered liquid crystalline phases of active matter can be classified according to their symmetry. Many active particles have a head and a tail, hence are intrinsically polar, such as birds and bacteria [26, 27]. These polar particles can form states with polar or ferromagnetic order, as shown in Figure 1.2d. Such ordered state has nonzero mean motion, i.e., it is a flocking state. Polar active particles can also form apolar or nematic states by aligning in opposite directions on the same axis. [3]. If the direction of the mean order is denoted by a unit vector \mathbf{n} , the ordered state is invariant under $\mathbf{n} \rightarrow -\mathbf{n}$ and has zero mean velocity. Then the system is in an apolar or nematic state, as shown in Figure 1.2f. We can also get a nematic state through ordering of intrinsically apolar active units, as shown in Figure 1.2e, such as vibrated rods [11], melanocytes [28] and some fibroblasts [29].

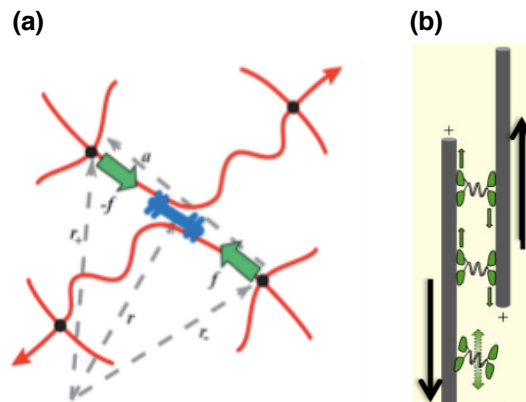


FIGURE 1.3: (a) Actomyosin behaving like contractile system, (b) microtubule-kinesin bundle behaving like extensile system.

1.2.2 Classification based on forces on the medium

Active systems can be classified by the nature of the forces the active units exert on their environment. Such forces are internal forces, so the total force exerted by an active particle on the medium is zero. When we write down the distribution of active force density $f(r)$ in terms of a multipole expansion, the leading terms would then be a dipole as the linear term being the net force is zero.

These dipoles can be contractile (see Fig. 1.3a), as in actomyosin networks or in migrating cell layers, or extensile (see Fig. 1.3b), as in suspensions of microtubule bundles or in most bacteria [2]. In the context of swimming microorganisms or artificial swimmers, units that exert extensile forces on the surrounding fluid are known as pushers, while those that exert contractile forces are known as pullers. Most bacteria are pushers, while the alga *Chlamydomonas* is an example of a puller. The extensile or contractile nature of active stresses can affect the stability of ordered states [30]

1.2.3 Classification Based on damping

Active particles move through a medium or on a substrate that provides frictional damping and mediates interactions. Systems where the frictional damping

is negligible compared to viscous dissipation are referred to as “wet”. In this case the medium mediates long-range hydrodynamic interactions between the active units. Systems where dissipation is mainly controlled by friction are referred to as “dry”. In “wet” systems, such as suspension of bipolar catalytic rods and swimming bacteria in bulk, the total momentum is conserved, which means momentum density is a slow, conserved variable and long-range hydrodynamic interactions between nearby active units play a vital role in the dynamics. In “dry” systems such as bacteria gliding on a surface [31], animal herds on land [32], or vibrated granular rods on a plate [33, 11, 9], the momentum of the active systems is not conserved because it is dissipated into the substrate. In systems dominated by friction, momentum density is a fast variable and hydrodynamic interactions may be important depending on the length scales of the system. For active particles in a viscous fluid of viscosity η and frictional drag γ , hydrodynamic flows can be neglected for length scales larger than $\sqrt{\eta/\gamma}$.

We will focus on the rich dynamics of active liquid crystals with nematic symmetry. We consider both contractile and extensile systems in our study. We will also explore both the “wet” and “dry” range of active systems.

A useful theoretical framework to describe the macroscopic properties of active matter is provided by generalized hydrodynamics - a coarse-grained description of the large-scale, long-time behavior of the system in terms of a small number of continuum fields. The evolution of these fields is governed by a set of continuum or hydrodynamic equations that can be obtained by modifying the hydrodynamics of passive fluids [5, 34] to include new nonequilibrium terms that arise from activity [35, 36, 7, 37, 15, 16, 2].

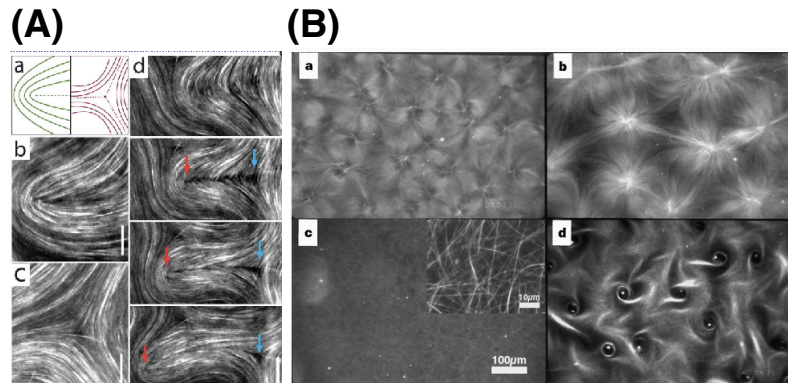


FIGURE 1.4: (a) Disclinations forming in MT bundles due to nematic symmetry of MT bundle in Dogic's group experiments [3, 4], (b) Microtubule-Kinesin polar rods leading to aster and vortex formation in Nedelec *et. al.* [5] due to polar symmetry in an individual MT.

1.3 Experimental motivation

The theoretical interest [36, 38, 39, 40, 41, 42, 30] in active nematics was first fueled by the observation of spontaneously flowing and turbulent states in suspensions of microtubule-kinesin bundles [3, 43] by the group of Zvonimir Dogic at Brandeis University. Other recent experimental realizations were obtained from the Lavrentovich's lab by immersing living swimming bacteria (specifically *E. coli*) in a lyotropic liquid crystal [44], and from the Silberzan's lab by plating dense layers of fibroblasts on substrates [29]. Microtubule bundles and *E. coli* exert active extensile force dipoles on their surroundings, which, in turn, couple to orientational order and induce spontaneous flows and self-sustained turbulent dynamics with proliferation of topological defects.

Topological defects are inhomogeneous configurations of the order field that provide a distinctive signature of liquid crystalline order and have been extensively studied in passive nematics. For passive nematics, defects may be generated

through boundary conditions, externally applied fields, or via sufficiently rapid quenches from the disordered to the ordered state [45, 46, 47]. When the constraints are removed or the system is given time to equilibrate, the defects ultimately annihilate and the system reaches the homogeneous ordered state that minimizes the free energy. The structure of the topological defects is intimately related to the broken symmetry of the ordered state and effectively provides a “fingerprint” of such a symmetry. When the ordered state has ferromagnetic (polar) symmetry, the lowest energy defect configurations are vortices and asters (monopoles) (see Fig. 1.4b), while in states with nematic symmetry, disclinations (see Fig. 1.4a), are possible [34] and have the lowest energy. The structure of the topological defects therefore provides an important tool for classifying the broken symmetry of liquid crystalline states.

In active liquid crystals, in contrast to passive ones, defect configurations can occur spontaneously in the bulk and be continuously regenerated by the local energy input, as demonstrated in experiments [28, 3, 44, 29]. While the aster and vortex defects that occur in polar active systems [5, 48] have been studied for some time [35, 36, 27, 26], the properties of defects in active nematics have only recently become the focus of experimental and theoretical attention. Disclinations have been identified in monolayers of vibrated granular rods [11], in active nematic gels assembled *in vitro* from microtubules and kinesins, in dense cell monolayers [28, 29], and in living liquid crystals obtained by injecting bacteria in chromonic liquid crystals [44]. In bulk suspensions of microtubule bundles the defects were shown to drive spontaneous flows [3]. When confined at an oil/water interface, furthermore, the same suspensions form a two-dimensional active nematic film, with self-sustained flows resembling cytoplasmic streaming and the continuous creation and annihilation of defect pairs [3].

Recent work by Giomi et al [49] and others [18, 38, 19, 20, 21] had begun to systematically examine the effect of activity on the dynamics of disclinations in

a nematic liquid crystalline film. They demonstrated that $+1/2$ disclinations in active liquid crystals behave like self-propelled particles with an active speed proportional to activity. The direction of active motion is controlled by the tensile or contractile nature of the active stresses. For certain relative orientations of pairs of defects of opposite strength, this self propulsion can overcome the equilibrium repulsive interaction among pairs of opposite-sign defects, allowing for dynamical states with an average sustained concentration of defect-antidefect pairs. In related work, Thampi *et al.* [18] suggested that the mean distance between defects in these turbulent states may be strongly correlated with the correlation length of fluctuations in the flow velocity, and only weakly dependent on activity.

In this thesis, I will mainly model the active material used in the experiments by Dogic's group [4]. This consists of microtubule (MT) filaments linked by clusters of motor proteins from the kinesin family. Individual MTs are polar. In early experiments by Nedelec *et al.* [5] and Surrey *et al.* [48], active mixtures of individual MT and kinesin were reported to have asters and spirals like defect structures (see Fig. 1.4B) demonstrating the polar nature of the system. In Dogic's experiment, however, due to the depletion mechanism, after adding a non-adsorbing polymer Poly Ethylene Glycol (PEG), these filaments form bundles (see Fig. 1.5b). Kinesin motors convert the chemical energy from the hydrolysis of ATP into mechanical work to exert force on the MTs and drive the system far from equilibrium. Kinesins are assembled into multi-motor clusters by streptavidin. These clusters can simultaneously bind and move along multiple MTs, displacing MTs within a bundle relative to each other, so that the bundle is an active unit [3]. Individual MTs are polar, and kinesin motors always move towards the $+$ end of the microtubule. As a result motor-induced sliding of aligned MTs depends on their polarity. If MTs are of the same polarity then there will not be any induced sliding but if MTs are of the opposite polarity then kinesin clusters generate sliding forces. Active MT bundles in contrast, are on average composed

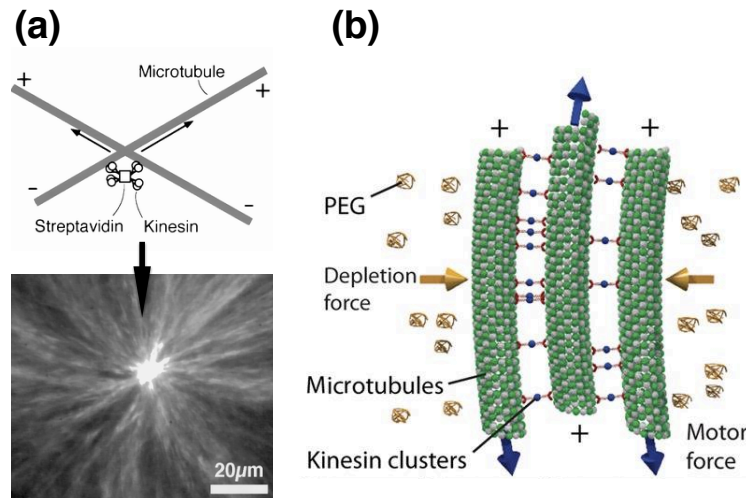


FIGURE 1.5: (A) Microtubule-Kinesin polar rods leading to aster formation in Nedelec *et. al.* [5], (B) microtubule-kinesin bundle formation due to PEG in Dogic's group experiments [3, 4].

of equal number of oppositely directed filaments and are apolar active units that exert extensile forces on the surrounding medium. Stabilizing these MT bundles at a 2D flat oil-water interface using a surfactant gives rise to an active 2D nematic fluid with fast streaming flows and defect unbinding. The nematic nature of Dogic's MT suspension is demonstrated by the appearance of half-integer charge disclinations (see Fig. 1.4A). Understanding the structure and dynamics of defects in these active systems can be an important method to understand the dynamics of the whole system.

1.4 Thesis Outline

In this thesis, we provide a theoretical and computational study of active nematics and of their complex dynamics. We will focus on pattern formations, including the proliferation of topological defects and their characterization.

In chapter 2, we review the dynamics of passive nematic liquid crystals and introduce the notion of topological defects and their properties.

In chapter 3, we present the results of a systematic numerical study of active nematic LC and of the various flow regimes induced by activity. Each regime is characterized in terms of flow patterns and defect proliferation. The chaotic regime exhibits a steady number of defects that persists in time.

In chapter 4, we show that the chaotic spatio-temporal dynamics in the regime of fully developed active turbulence is controlled by a single active length scale determined by the balance of active and elastic stresses, regardless of whether the active stress is extensile or contractile in nature.

In chapter 5, we consider a dry active nematic fluid, where the energy input from active stresses is balanced solely by frictional damping. By eliminating the flow velocity in the favor of active stresses we obtain a single equation for the nematic order parameter, with elastic constant renormalized by activity. We show that activity can drive such elastic constants to negative values, providing a mechanism for pattern formation capable of describing in a unified manner all the spatio-temporal structures obtained in previous models. A remarkable phenomenon reported by several authors is the orientational ordering of the axes of the comet-like $+1/2$ disclinations. In experiments in suspensions of microtubule bundles the $+1/2$ defects were observed to organize in nematically ordered states. In our model we have also observed these defect-ordered structures.

Chapter 2

Passive Nematic Liquid Crystals

2.1 Introduction

Liquid crystals (LCs) as the name suggests are an intermediate state of matter. They have properties of both liquids and crystals. They flow like fluids, but they also have some crystalline properties such as strong anisotropy in their response to external fields. LCs can be formed by molecules with anisotropic shapes, like rods or discs. The simplest LC is a liquid of elongated rod-like molecules that can form *isotropic* or *nematic* phases [50, 51]. In the isotropic state, the molecules have random position and orientation (see Fig. 2.1a) and the system is an isotropic fluid with no positional nor orientational order. By decreasing the temperature or increasing the density one can drive the transition to nematic state where, the molecules align along a preferred orientation while retaining random positions (see Fig. 2.1b) [50, 51].

If we consider a fluid with thin hard rods, we will realize that, at very low density rods can easily orient in any random direction thus remaining in the isotropic phase. But if we increase the density it becomes increasingly difficult for rods to orient in a random direction. A fluid of hard rods undergoes a density driven

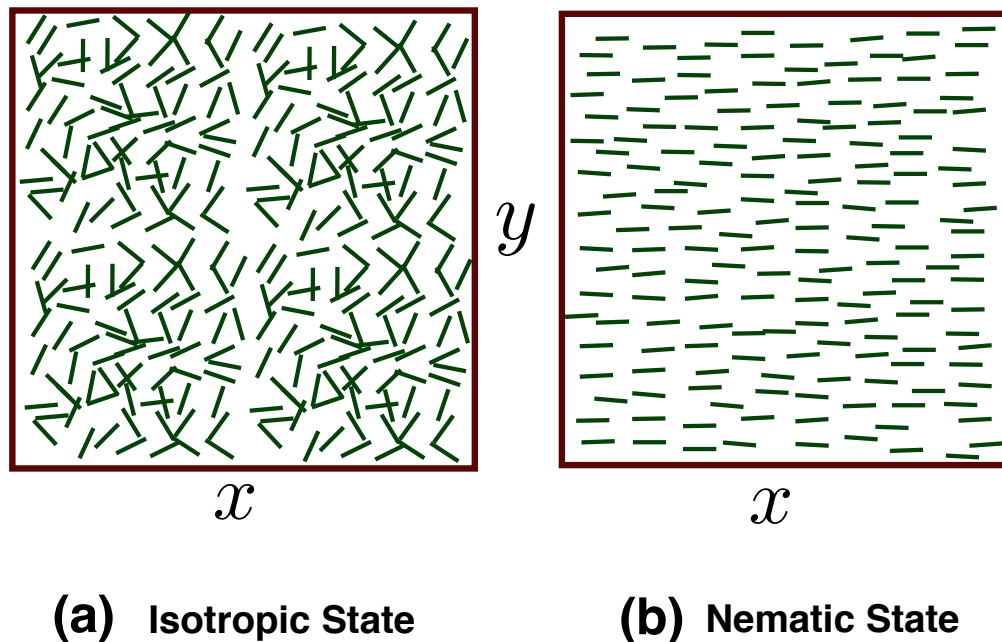


FIGURE 2.1: (a) Nematic LCs in an isotropic state with each unit having random orientation, (b) Nematic LCs in nematic state with average ordering in the x direction.

transition to orientationally ordered anisotropic phase with uniaxial symmetry *i.e.*, a nematic phase. In fact, Onsager proved that this phase transition from the isotropic state (I) to the nematic state (N) does indeed happen [51]. Onsager's theory about this IN phase transition is based on the effect of excluded volume associated with arrangement of hard rods on the entropy of the system [50, 51]. In order to find the steady state, we need to minimize the free energy. Since the potential energy in the case of hard rods is constant, we can achieve free energy minimization by maximizing the system's entropy. The entropy of our system has two contributions, *translational entropy* and *orientational entropy*. The IN phase transition exists due to the competition between these two contributions. Above a critical density ρ_{IN} , rods tend to align in a preferred orientation. This makes the negative contribution due to *orientational entropy* smaller than the positive contribution due to *translational entropy*. Hence, the net entropy of the

fluid increases. So, for $\rho < \rho_{IN}$ the system remains in isotropic phase, while for $\rho > \rho_{IN}$ the system transitions to a nematic phase.

2.2 Order parameter tensor

To characterize nematic order, let us first introduce a unit vector \mathbf{u}^i oriented along the axis of i th rod-shaped molecule which describes its orientation. Since the nematic molecules either have a center of inversion or equal probability of pointing parallel or anti-parallel to any given direction, both \mathbf{u}^i and $-\mathbf{u}^i$ are equivalent. For this reason, it is not useful to introduce a vector order parameter for liquid crystals analogous to the magnetization in a ferromagnet because its average value vanishes in the nematic phase. We therefore need a second rank tensor to characterize nematic [50]. We require the order parameter to be zero in the isotropic phase but non zero in the nematic phase. We construct the order parameter from the symmetric traceless tensor [50, 51] formed from \mathbf{u}^i as following,

$$Q_{\alpha\beta}(\mathbf{r}) = \left\langle \frac{1}{N} \sum_i (u_{\alpha}^{(i)} u_{\beta}^{(i)} - \frac{1}{3} \delta_{\alpha\beta}) \right\rangle, \quad (2.1)$$

where the sum is over all the N molecules in a small but macroscopic volume located at the point \mathbf{r} ; indexes $\alpha, \beta = (x, y, z)$ and $\langle \dots \rangle$ represents the average over all particles. Let \mathbf{Q} be the tensor with components $Q_{\alpha\beta}$. Since \mathbf{u}^i is a unit vector, $\text{Tr}[\mathbf{Q}] = 0$. In the ordered state the average order parameter tensor, \mathbf{Q} is not zero. For simple uniaxial nematic LCs, we can write \mathbf{Q} as [50],

$$Q_{\alpha\beta} = S(n_{\alpha} n_{\beta} - \frac{1}{3} \delta_{\alpha\beta}). \quad (2.2)$$

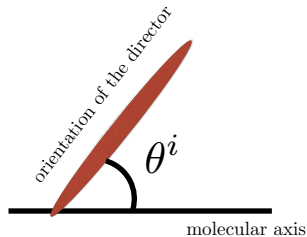


FIGURE 2.2: The angle θ^i between molecular axis and the director \mathbf{n}

where, the unit vector \mathbf{n} , called the Frank director, specifies the direction of spontaneously broken symmetry of $Q_{\alpha\beta}$ and $S = \frac{1}{2}\langle(3 \cos^2 \theta^i - 1)\rangle$ is the order parameter with $S = 0$ in the isotropic and $S \neq 0$ in the nematic, and θ^i is the angle between the molecular axis and the director \mathbf{n} (see Fig. 2.2).

2.3 Landau free energy

We can now construct a Landau free energy [52, 50, 51] for nematic LCs. The free energy density must be invariant under all rotations thus can only be function of the scalar combination of $\text{Tr}[\mathbf{Q}^p]$, where $p = 2, 3 \dots$ that is,

$$\begin{aligned} f_b &= \frac{A}{2} \left(\frac{3}{2} \text{Tr}[\mathbf{Q}^2] \right) - B \left(\frac{9}{2} \text{Tr}[\mathbf{Q}^3] \right) + C \left(\frac{3}{2} \text{Tr}[\mathbf{Q}^2] \right)^2 \\ &= \frac{A}{2} S^2 - B S^3 + C S^4 \end{aligned} \quad (2.3)$$

where $A = a(\rho - \rho^*)$, B and C are constant, positive, and independent of density. The cubic term in the free energy density leads to an asymmetry in f as a function of S and the emergence of secondary minimum at finite S. That means that there is a critical density ρ_{IN} above ρ^* , there is a first-order transition at ρ_{IN} , where the system goes from the disordered or the isotropic phase to the ordered or the nematic phase. We can find out the critical density ρ_{IN} by minimizing the free energy by making first order derivative of free energy density f_b with respect to

the order parameter S zero at critical density ρ_{IN} and the second order derivative with respect to the order parameter S positive [50, 51]. That is,

$$\frac{\partial f_b}{\partial S} = (A - 3 B S + 4 C S^2)S = 0 \quad (2.4)$$

We take the root with largest magnitude among $S_c = \{0, \frac{3 B \pm \sqrt{9 B^2 - 16 A C}}{8 C}\}$. By requiring $\frac{\partial^2 f_b}{\partial S^2} > 0$ at the critical point, we can find the component A at critical density ρ_{IN} , $A_c = a(\rho_{IN} - \rho^*) = \frac{9B^2}{16 C}$. The form of the critical density ρ_{IN} can then be written as following,

$$\rho_{IN} = \rho^* + \frac{9B^2}{16 a C} \quad (2.5)$$

In 2d, however, $\text{Tr}[\mathbf{Q}^3]$ is identically zero because \mathbf{Q} is symmetric and traceless. The free energy then becomes,

$$f_{b_{2d}} = \frac{A}{2} S^2 + C S^4 \quad (2.6)$$

Now when we minimize the free energy with respect to the order parameter S , we get $S_c = \{0, \sqrt{\frac{-A}{4C}}\}$. The second order derivative of the free energy with respect to S at critical density $\frac{\partial^2 f_{b_{2d}}}{\partial S^2}|_{S_c} = A + 12 C S^2 = -2 A$. In this case we find a continuous phase transition from the isotropic to the nematic phase at $A = 0$ *i.e.* $\rho_{IN} = \rho^*$. The system exists in the isotropic phase for $A > 0$ and it transitions to the nematic phase for $A < 0$ [51].

So far we have only considered the free energy associated with homogeneous state. We now examine the role of spatially inhomogeneous fluctuations in the nematic state. To lowest order in gradients of \mathbf{Q} , the free energy density is then given by $f = f_b + f_Q$, with the elastic energy f_Q in terms of \mathbf{Q} [40] as follows,

$$f_Q = \frac{L_1}{2} (\partial_\alpha Q_{\beta\gamma})^2 + \frac{L_2}{2} (\partial_\alpha Q_{\alpha\gamma})(\partial_\beta Q_{\beta\gamma}) + \frac{L_3}{2} Q_{\alpha\beta} (\partial_\alpha Q_{\gamma\epsilon})(\partial_\beta Q_{\gamma\epsilon}) \quad (2.7)$$

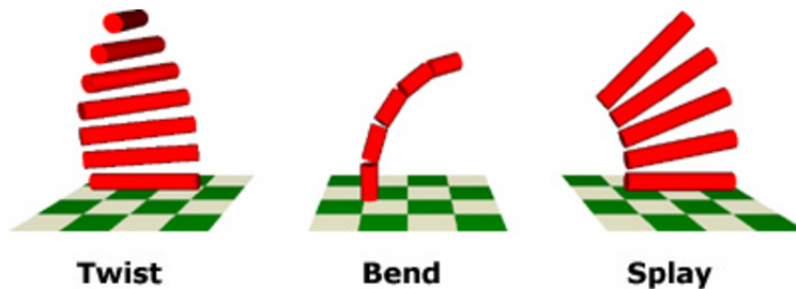


FIGURE 2.3: (a) Twist deformation, (b) Bend deformation, (c) Splay deformation.

where L_1, L_2 and L_3 are coefficients to the distortion costs in gradients of \mathbf{Q} .

Taking into consideration that \mathbf{n} is a unit vector, assuming the system is deep in the nematic phase, the order parameter S can be assumed to be constant S_0 throughout the system, so that only the distortions in the director \mathbf{n} will be important here. The elastic free energy of fluctuating nematic phase becomes,

$$f_n = \frac{1}{2} \int d^d x \{ K_1 (\nabla \cdot \mathbf{n})^2 + K_2 [\mathbf{n} \cdot (\nabla \times \mathbf{n})]^2 + K_3 [\mathbf{n} \times (\nabla \times \mathbf{n})]^2 \} \quad (2.8)$$

Above form of free energy is also known as Frank free energy [50, 51] where K_1, K_2 and K_3 are Frank elastic constants that measure the deformation cost. K_1 measures the energy cost of *splay* deformations (see Fig. 2.3c), corresponding to nonzero $\nabla \cdot \mathbf{n}$, K_2 measures *twist* (see Fig. 2.3a), with nonzero $\mathbf{n} \cdot (\nabla \times \mathbf{n})$, and K_3 measures *bend* (see Fig. 2.3b), with nonzero $\mathbf{n} \times (\nabla \times \mathbf{n})$. The elastic constants K_1, K_2 and K_3 have units of energy/length. In 2D, however, K_2 does not play a role because twist does not occur as $\mathbf{n} \cdot (\nabla \times \mathbf{n})$ is identically zero.

Comparison between Eq. 2.7 and Eq. 2.8 using $Q_{\alpha\beta} = S_0(n_\alpha n_\beta - \delta_{\alpha\beta}/3)$ gives the following relations between the L_i 's and the Frank constants,

$$L_1 = \frac{3K_2 - K_1 + K_3}{6S_0^2}; \quad L_2 = \frac{K_1 - K_2}{S_0^2}; \quad L_3 = \frac{K_3 - K_1}{2S_0^3} \quad (2.9)$$

Furthermore for simplification we will consider below the one-elastic constant limit

so that $K_1 = K_2 = K_3 = K$ hence $L_2 = L_3 = 0$ and $L_1 = \frac{K}{3S_0^2}$. In 2d, however, with one-elastic constant $K_1 = K_3 = K$ approximation we get $L_3 = 0$ and $L_1 = K/S_0^2$. Since deep in the nematic phase, S_0 is constant, so for simplification, we will assume $L_1 = K$ without loss of generality. We can then write the elastic energy in terms of gradient of \mathbf{Q} as following,

$$f_Q = \frac{K}{2} |\nabla \mathbf{Q}|^2 \quad (2.10)$$

Adding Eq. 2.10 to the Eq. 2.3 discussed above results in the full form of the Landau free energy density as following,

$$f_{LdG} = \frac{A}{2} \text{Tr} [\mathbf{Q}^2] - B \text{Tr} [\mathbf{Q}^3] + C \text{Tr} [\mathbf{Q}^2]^2 + \frac{K}{2} |\nabla \mathbf{Q}|^2 \quad (2.11)$$

2.4 Topological defects

In the nematic state, orientational symmetry is broken spontaneously leading to a very rich physics [50, 51]. Even though the system may carry a global nematic order, at the local level it can still exhibit inhomogeneous configurations in the order fields. Topological defects are spatially inhomogeneous configurations of the order parameter field that cannot be eliminated via a continuous deformation.

The presence of the topological defects not only changes the physical properties in their vicinity, but also increases the overall free energy of the system. Consequently, an ideal ordered medium is free of defects. However, the influence of the external fields, surfaces, or a lowering of the symmetry (isotropic to nematic transition) can spontaneously and/or controllably create and stabilize topological defects [51]. The physics of topological defects is also very rich and had been studied in regards to cosmology and condensed matter system equally for a long period of time [51]. Consider a planar structure in which the director is

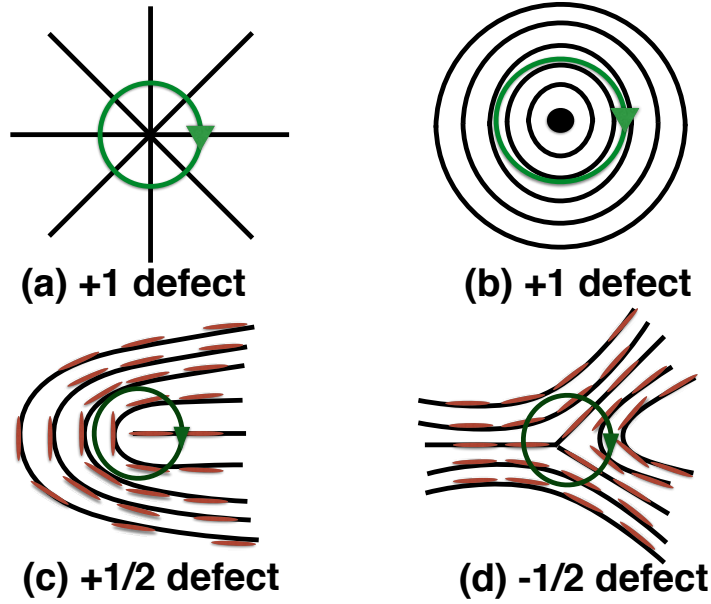


FIGURE 2.4: (a) -1 defect structure ($\oint d\theta = -2\pi$) or asters in polar system, (b) +1 defect structure ($\oint d\theta = 2\pi$) or vortices in polar systems, (c) +1/2 defect structure ($\oint d\theta = \pi$) in nematic suspension, (d) -1/2 defect structure ($\oint d\theta = -\pi$) in nematic suspension. The green clockwise circle signifies the direction in which the loop integration is performed.

confined to the xy plane (the z axis being normal to the film). For elastically isotropic (one-elastic constant approximation) system with director components as $n_x = \cos \phi, n_y = \sin \phi, n_z = 0$, the Landau free energy reduces to $F = \frac{K}{2}(\nabla\phi)^2$. Using Eq. 2.18, we can arrive at the steady state solution of the ϕ by solving,

$$0 = \frac{1}{\gamma} H_{ij} \quad (2.12)$$

Since, $H_{ij} = -\frac{\partial F}{\partial \phi} = \frac{K}{2} \nabla^2 \phi$. Substituting H_{ij} to Eq. 2.12 we get a Laplace equation $\nabla^2 \phi = 0$. Simple solutions of this Laplace equation will be $\phi = 0, \phi = s\alpha + c$, where $\alpha = \tan^{-1}(y/x)$ and c is a constant. The director configuration around the disclination can be described by non-zero solution of ϕ as the director orientation changes by $2k\pi$, on going round the loop around the core of the defect [51].

A mapping from some loop Γ in real space onto the order parameter space such that physical order parameter remains single-valued in a complete circuit of Γ can

be used to characterize these defects [50]. For the polar state, this implies

$$\oint d\theta = \oint_{\Gamma} \frac{d\theta}{ds} ds = 2k\pi \quad (2.13)$$

where k is called the winding number and $k = 0, \pm 1, \dots, s$ [50, 51]. In 2d the line integral about the core is taken in the counterclockwise direction. These defects are called *vortices* (see Fig. 2.4a,b). In the polar state, vortices are lowest energy defect configurations [50, 51].

For the nematic phase, since positive and negative directions of the director are equivalent, physical configurations in the nematic are invariant under inversion of the director ($\mathbf{n} \rightarrow -\mathbf{n}$), and the order parameter space is the unit circle with opposite points identified (i.e. $\theta = 0$ and $\theta = \pi$ are equivalent). Because of this, there is a topologically stable defect in which θ changes by $\pm\pi$ on the circuit enclosing the core. Hence k in Eq. 2.13, can also attain half integer values, $k = 0, \pm 1/2, \pm 1, \dots, \pm 3/2, \dots$ [50, 51] for the nematic state. These defects with half-integral winding number are not possible in polar state. Since nematic defects involve rotations, they are often called *disclinations* (see Fig. 2.4c,d). In the nematic state, disclinations are lowest energy defect configurations [45, 46, 47, 53].

The structure of topological defects is intimately related to the broken symmetry of the ordered state and effectively provides a “fingerprint” of such a symmetry. A topological defect is in general characterized by a core region (*e.g.*, a point or a line) where the order is destroyed and a far field region where an elastic variable changes very slowly in the space.

Topological defects may be generated by applying external forces on boundaries or applying electric field in the bulk of the system. In equilibrium, opposite sign defects attract each other and ultimately annihilate leading to a uniform ordered state [50, 51].

2.5 Nemato-hydrodynamics

Next we discuss the hydrodynamics of equilibrium nematic LCs. Physical properties exhibited by the nematic phase, such as unusual flow properties or its response to boundary forces as well as electric and magnetic fields can be studied by regarding liquid crystal as a continuous medium [51]. We will closely follow the continuum theory laid out by Ericksen and Leslie [51], formulated on the basis of general conservation laws and constitutive equations describing the mechanical behavior of the nematic state. Here we construct the continuum model phenomenologically but it has been shown that it can be derived from microscopic models [50, 51]. At large length scales and long time we describe the dynamics of the system in terms of flow fields, *i.e.* ones whose fluctuation becomes long lived at long wavelength. These correspond to conserved quantities, the total density of the system ρ , the momentum density $\rho\mathbf{v}$ and the nematogen concentration c . Additionally, we also consider the dynamics of the nematic order tensor \mathbf{Q} [50]. From now on, we will restrict ourselves to 2d nematics. We will also assume that the system is incompressible.

2.5.1 Dynamics of density

We consider a concentration c of nematogens of mass M and length ℓ , suspended in a solvent of density ρ_s . The total density of the system, $\rho = Mc + \rho_s$ is conserved hence satisfies a continuity equation, given by,

$$\frac{\partial \rho}{\partial t} = \nabla \cdot (\rho \mathbf{v}) \quad (2.14)$$

We assume that the fluid is incompressible or $\rho = \text{constant}$, which means $\nabla \cdot \mathbf{v} = 0$. The concentration c , of nematogens obeys a diffusion equation:

$$\frac{Dc}{Dt} = \partial_i [D_{ij} \partial_j c], \quad (2.15)$$

where $D/Dt = \partial_t + \mathbf{v} \cdot \nabla$ is the material derivative and $D_{ij} = D_0 \delta_{ij} + D_1 Q_{ij}$ is the anisotropic diffusion tensor [54].

2.5.2 Dynamics of momentum density

The dynamics of the momentum density is governed by the Navier-Stokes equation, given by,

$$\rho \frac{Dv_i}{Dt} = \eta \nabla^2 v_i - \partial_i p + \partial_j \sigma_{ij}, \quad (2.16)$$

where η is the shear viscosity, p is the pressure, and σ_{ij} is the stress tensor. The elastic stress tensor is, $\sigma_{ij} = -\lambda S H_{ij} + Q_{ik} H_{kj} - H_{ik} Q_{kj}$. The molecular tensor $H_{ij} = -\delta F_{LdG} / \delta Q_{ij}$ is the driving force for the relaxation dynamics of the nematic LC with $F_{LdG} = \int dA f_{LdG}$ [54], where f_{LdG} is given by Eq. 2.11. For 2D case, the term associated with constant B is identically zero in Eq. 2.11 hence,

$$f_{LdG} = \frac{A}{2} \text{Tr}(\mathbf{Q})^2 + \frac{C}{4} \text{Tr}(\mathbf{Q}^2)^2 + \frac{K}{2} |\nabla \mathbf{Q}|^2 \quad (2.17)$$

The coefficients A and C determine the location of continuous transition from homogeneous isotropic state to a homogeneous nematic state in 2D.

2.5.3 Dynamics of order parameter tensor

Finally, the dynamics of the nematic order parameter tensor Q_{ij} is governed by,

$$\frac{DQ_{ij}}{Dt} = \lambda S u_{ij} + Q_{ik} \omega_{kj} - \omega_{ik} Q_{kj} + \frac{1}{\gamma} H_{ij}, \quad (2.18)$$

where $u_{ij} = (\partial_i v_j + \partial_j v_i)/2$ and $\omega_{ij} = (\partial_i v_j - \partial_j v_i)/2$ are the symmetric and antisymmetric parts of velocity gradient, corresponding to strain rate and vorticity tensor respectively. The parameter γ is an orientational viscosity and λ is the nematic alignment parameter. In Eq. 2.18 first three terms, on the right hand side couple flow and order. The last term represents the relaxation dynamics due to the molecular tensor H_{ij} .

Chapter 3

Hydrodynamics of active nematics

This chapter is based on the article “Defect dynamics in active nematics” published in “Phil. Trans. R. Soc. A:2014 372 20130365” by Luca Giomi, Mark J. Bowick, Prashant Mishra, Rastko Sknepnek, and M. Cristina Marchetti. I was responsible for generating the simulation results discussed in section 5 of the paper.

3.1 Introduction

In this chapter we focus on the rich dynamics of active liquid crystals with nematic symmetry. We consider both extensile [3, 44] and contractile [29] systems. Previous work has highlighted the rich dynamics that arises in active nematics from the interplay of activity, orientational order and flow [6, 7, 8, 15, 26, 16]. More recently it was suggested that topological defects play an important role in mediating and driving turbulent-like active flows [3, 49, 18, 19, 20, 21].

We first review the hydrodynamic description of active nematics and the instabilities of the homogeneous ordered state. In Section 3.5 we present the results of a systematic numerical study of the various flow regimes induced by activity, as summarized in the phase diagram shown in Fig. 3.7. Each regime is characterized in terms of flow patterns and defect proliferation. The chaotic regime exhibits a steady number of defects that persist in time. This is made possible by active flows that drive directed motion of the comet-like $+1/2$ defects, generating, for certain relative orientations of two opposite sign defects, an effective repulsive interaction between the pair. The mechanisms for this active defect dynamics are analyzed in Sections 3.3 and 3.4, where we discuss individual defect dynamics and pair annihilation in active nematics, respectively. We conclude with a brief discussion highlighting open questions.

3.2 Active nematodynamics

3.2.1 Governing Equations

We consider a uniaxial active nematic liquid crystal in two dimensions. The two-dimensional limit is appropriate to describe the experiments by Sanchez *et al.* [3], where the microtubule bundles confined to a water-oil interface form an effectively two-dimensional dense nematic suspension, but also of considerable interest in its own right. The hydrodynamic equations of active nematic liquid crystals have been derived by coarse-graining a semi-microscopic model of cytoskeletal filaments crosslinked by clusters of motor proteins [39]. They can also simply be obtained from the hydrodynamic equations of passive systems by the addition of nonequilibrium stresses and currents due to activity [35, 36, 7, 37, 15, 16, 2]. We consider here an incompressible suspension where the total density ρ of active bundles and solvent is constant. The equations are formulated in terms of the concentration c

of active units, the flow velocity \mathbf{v} of the suspension and the nematic tensor order parameter $Q_{ij} = S(n_i n_j - \delta_{ij}/2)$, with \mathbf{n} the director field. The alignment tensor Q_{ij} is traceless and symmetric, and hence has only two independent components in two dimensions. The constraint of constant density ρ requires $\nabla \cdot \mathbf{v} = 0$. The hydrodynamic equations are given by [15]

$$\frac{Dc}{Dt} = \partial_i [D_{ij} \partial_j c + \alpha_1 c^2 \partial_j Q_{ij}] , \quad (3.1a)$$

$$\rho \frac{Dv_i}{Dt} = \eta \nabla^2 v_i - \partial_i p + \partial_j \sigma_{ij} , \quad (3.1b)$$

$$\frac{DQ_{ij}}{Dt} = \lambda S u_{ij} + Q_{ik} \omega_{kj} - \omega_{ik} Q_{kj} + \frac{1}{\gamma} H_{ij} , \quad (3.1c)$$

where $D/Dt = \partial_t + \mathbf{v} \cdot \nabla$ indicates the material derivative, $D_{ij} = D_0 \delta_{ij} + D_1 Q_{ij}$ is the anisotropic diffusion tensor, η the viscosity, p the pressure, λ the nematic alignment parameter, and γ the rotational viscosity. Here $u_{ij} = (\partial_i v_j + \partial_j v_i)/2$ and $\omega_{ij} = (\partial_i v_j - \partial_j v_i)/2$ are the strain rate and vorticity tensor, respectively, representing the symmetric and antisymmetric parts of the velocity gradient. The molecular field $H_{ij} = -\delta F_{\text{LdG}}/\delta Q_{ij}$ embodies the relaxational dynamics of the nematic obtained from the variation of the two-dimensional Landau-de Gennes free energy $F_{\text{LdG}} = \int dA f_{\text{LdG}}$ [34], with

$$f_{\text{LdG}} = \frac{1}{2} A \text{Tr} [\mathbf{Q}^2] + \frac{1}{4} C (\text{Tr} [\mathbf{Q}^2])^2 + \frac{1}{2} K |\nabla \mathbf{Q}|^2 , \quad (3.2)$$

where K is an elastic constant with dimensions of energy. For simplicity we restrict ourselves here to the one-elastic constant approximation to the Frank free energy: i.e. equal bend and splay moduli. The coefficients A and C determine the location of the continuous transition from a homogeneous isotropic state with $S = 0$ to a homogeneous nematic state with finite value of S , given by $S = \sqrt{-2A/C}$ (where we have used $\text{Tr} [\mathbf{Q}^2] = S^2/2$). We are interested here in a system where the transition is driven by the concentration of nematogens, as is the case for a

fluid of hard rods of length ℓ that exhibits an isotropic-nematic (IN) transition at a concentration $c^* = 3\pi/2\ell^2$ in two dimensions. Noting that A and C have dimensions of energy density (in two dimensions), we choose $A = K(c^* - c)/2$ and $C = Kc$ [16]. This gives $S = S_0 = \sqrt{1 - c^*/c_0}$ in a homogeneous state of density c_0 , so that $S_0 = 0$ for $c_0 \ll c^*$ and $S_0 \approx 1$ for $c_0 \gg c^*$. The ratio $\sqrt{K/|A|}$ defines a length scale that corresponds to the equilibrium correlation length of order parameter fluctuations and diverges at the continuous IN transition [46]. Here we restrict ourselves to mean values of concentration well above c^* , where this equilibrium correlation length is microscopic and is of the order of the size ℓ of the nematogens, which will be used as our unit of length in the numerical simulation. Finally, the stress tensor $\sigma_{ij} = \sigma_{ij}^r + \sigma_{ij}^a$ is the sum of the elastic stress due to nematic elasticity,

$$\sigma_{ij}^r = -\lambda S H_{ij} + Q_{ik} H_{kj} - H_{ik} Q_{kj} , \quad (3.3)$$

where for simplicity we have neglected the Eriksen stress, and an active contribution, given by [2]

$$\sigma_{ij}^a = \alpha_2 c^2 Q_{ij} , \quad (3.4)$$

which describes stresses exerted by the active particles. The sign of α_2 depends on whether the active particles generate contractile or extensile stresses, with $\alpha_2 > 0$ for the contractile case and $\alpha_2 < 0$ for extensile systems. Activity yields also a curvature-induced current given by the last term on the right hand side of Eq. (3.1a), $\mathbf{j}^a = -\alpha_1 c^2 \nabla \cdot \mathbf{Q}$, that drives active units from regions populated by fast moving particles to regions of slow moving particles. The c^2 dependence of the active stress and current is appropriate for systems where activity arises from pair interactions among the filaments via crosslinking motor proteins. The active parameters α_1 and α_2 will be treated here as phenomenological quantities. In microscopic models they are found to depend on the concentration of active

crosslinkers and on the consumption rate of adenosine triphosphate (ATP) [55, 56].

3.2.2 Linear Stability

The hydrodynamic equations of an active nematic have two homogeneous stationary solutions, with $c = c_0$ and $\mathbf{v} = \mathbf{0}$. For $c_0 < c^*$ the homogeneous state is disordered with $S_0 = 0$. For $c_0 > c^*$ the homogeneous solution is an ordered nematic state with $S_0 = \sqrt{1 - c^*/c_0}$. The linear stability of the ordered state has been studied in detail for the case of a $L \times L$ periodic domain [15, 16]. It is found that above a critical activity the homogenous state is unstable to a laminar flowing state. This instability corresponds to the spontaneous flow instability well-studied in a channel geometry [6, 8, 40]. The critical activity value associated with the instability of the homogeneous state is given by [16]

$$\alpha_2^\pm = \pm \frac{4\pi^2 K [2\eta + \gamma S_0^2 (1 \mp \lambda)^2]}{\gamma c_0^2 L^2 S_0 (1 \mp \lambda)}. \quad (3.5)$$

For $|\alpha_2| > |\alpha_2^+|$ the system is subject to spontaneous splay deformations characterized by the instability of the first transverse mode. For $|\alpha_2| > |\alpha_2^-|$ on the other hand, the instability is determined by the first longitudinal mode corresponding to bending deformations. Note that the sign of α_2^\pm depends both on the sign of the fraction and the sign of the term $1 \mp \lambda$ at the denominator. Thus flow-aligning nematics ($|\lambda| > 1$) are unstable to splay under the effect of an extensile active stress ($\alpha_2 < \alpha_2^+ < 0$) and to bending under the effect of a contractile active stress ($\alpha_2 > \alpha_2^- > 0$). Vice versa, flow-tumbling nematics ($-1 < \lambda < 1$) are unstable to bending under the effect of an extensile active stress ($\alpha_2 < \alpha_2^- < 0$) and to splay under the effect of a contractile active stress ($\alpha_2 > \alpha_2^+ > 0$). In this paper we focus exclusively on flow-tumbling systems and discuss both the cases of extensile and contractile stresses.

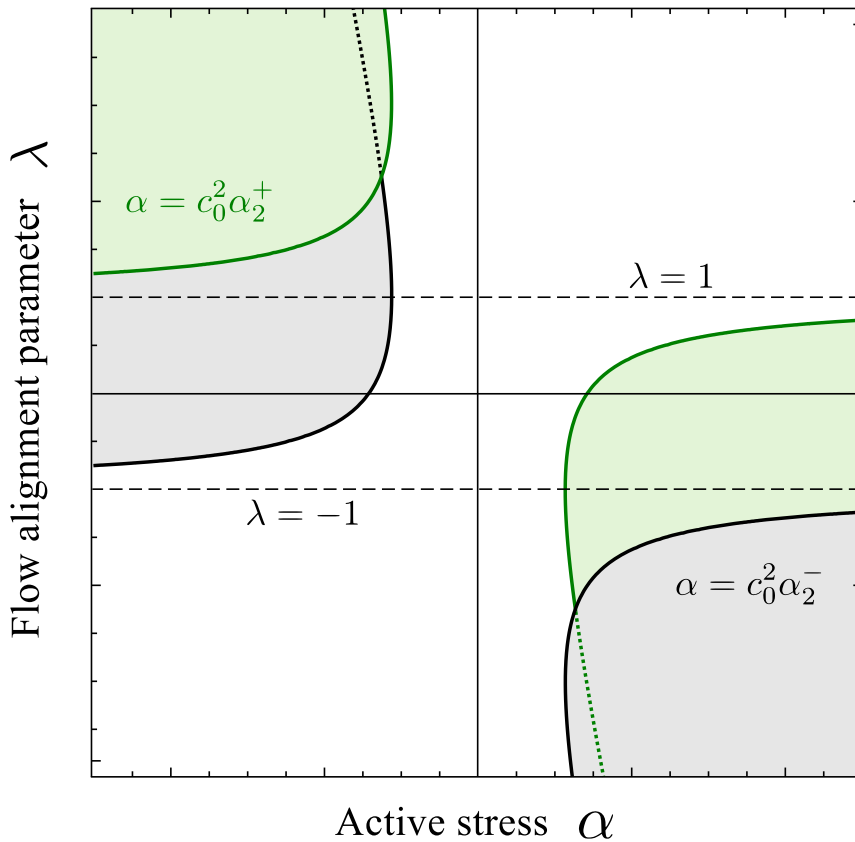


FIGURE 3.1: Schematic representation of the region where an active nematic is linearly unstable to splay (green) and to bend (gray) fluctuations in the plane of the alignment parameter λ and the activity $\alpha = c_0^2 \alpha_2$. The unstable regions are bounded by the critical activity given in Eq. (3.5). Flow tumbling extensile nematic with $|\lambda| < 1$ are unstable to bend when active stresses are extensile ($\alpha < 0$) and to splay when active stresses are contractile ($\alpha > 0$). Conversely, strongly flow aligning ($|\lambda| \gg 1$) are unstable to splay when active stresses are extensile ($\alpha < 0$) and to bend when active stresses are contractile ($\alpha > 0$).

3.2.3 Dimensionless Units and Numerical Methods

To render Eqs. (3.1) dimensionless, we scale distances by the length of the active nematogens ℓ , set by the critical concentration c^* , stresses by the elastic stress of the nematic phase $\sigma = K/\ell^2$ and time by $\tau = \eta\ell^2/K$ representing the ratio between viscous and elastic stress. In these dimensionless units we take $\alpha_1 = |\alpha_2|/2$ and we introduce

$$\alpha = \alpha_2 c_0^2, \quad (3.6)$$

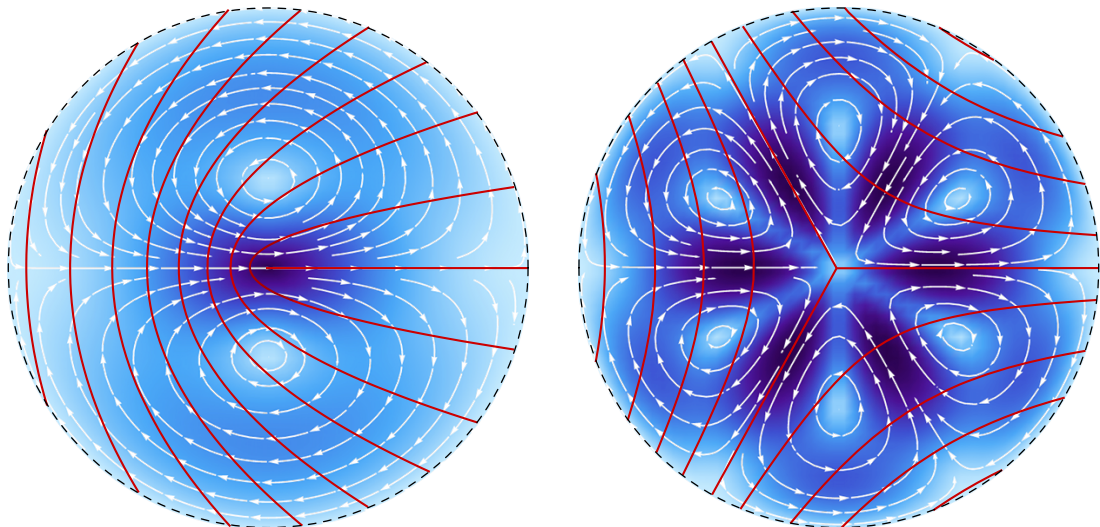


FIGURE 3.2: Example of a $+1/2$ (left) and $-1/2$ (right) disclination. The solid red lines are tangent to the director field $\mathbf{n} = (\cos \theta_d, \sin \theta_d)$ with $\theta_d = k\phi$ and $k = \pm 1/2$. The background shows the active backflow associated with the disclinations and obtained by solving the Stokes equation (3.12) with no-slip boundary conditions on a circle (dashed black line). The intensity of the background color is proportional to the magnitude of the flow velocity. The white streamlines are given by Eq. (3.15).

representing the fundamental scale of active stress. This will serve as the control parameter throughout this work.

The numerical calculations presented in Sec. 3.4 and 3.5 are performed via finite differences on a collocated grid of 256^2 points. The time integration was performed via a fourth order Runge-Kutta method with time step $\Delta t = 10^{-3}$. Except where mentioned otherwise, the numerical calculations described in this section use the parameter values $D_0 = D_1 = 1$ (simplification), $\lambda = 0.1$ (flow tumbling regime), $c_0 = 2c^*$ (corresponding to $S_0 = 0.707$) and $L = 20$.

3.3 Dynamics of an isolated disclination

Topological defects are spatially inhomogeneous configurations of the director field that cannot be transformed continuously into a uniform state. In equilibrium, defects can occur upon quench from the disordered into the ordered phase or upon

application of external electric or magnetic fields. Geometry or suitable boundary conditions can also be used to generate and maintain defects in the system. For instance, in a spherical nematic droplet with boundary condition such that the director is normal to the droplet surface, the equilibrium configuration consists of a radial director field with a point defect at the center of the droplet. In the absence of such constraints or external fields, when the system is allowed enough time to equilibrate, defects of opposite sign always annihilate and the system settles into the uniform equilibrium state [57, 58].

In two dimensions defects are point-like. The strength of a disclination depends on how much the director field rotates around the defect core in one loop. In two dimensions, this can be expressed in terms of a single scalar field θ representing the angle formed by the director $\mathbf{n} = (\cos \theta, \sin \theta)$ with the horizontal axis of a Cartesian frame. This gives

$$\oint d\theta = 2\pi k, \quad (3.7)$$

where the integral is calculated along an arbitrary contour enclosing the defect. The integer k is called strength of the defect and is analogous to the winding number of vortex defects in polar systems. In two-dimensional uniaxial nematics the lowest energy defect configurations consists of half-strength disclinations with $k = \pm 1/2$. In the presence of an isolated defect located at the origin, a solution $\theta = \theta_d$ that minimizes the energy (3.2) and satisfies the constraint (3.7) is given by

$$\theta_d = k\phi, \quad (3.8)$$

with ϕ the usual polar angle. The corresponding energy is given by

$$F = \pi K k^2 \log(R/a) + \epsilon_c, \quad (3.9)$$

where R is the size of the system and a is the core radius, defined as the radius of the region in the immediate proximity of the defect where the order parameter

drops from its equilibrium value to zero. The quantity ϵ_c is the contribution to the total energy due to the normal defect core.

Point defects in nematic liquid crystals have several particle-like features. Like charged particles, opposite-sign defects attract and same-sign defects repel ([34] and Sec. 3.4). It is well established that the dynamics of an isolated disclination that evolves according to Eqs. (3.1) can be cast in the form of an overdamped equation of motion, given by

$$\zeta \left(\frac{d\mathbf{r}}{dt} - \mathbf{v} \right) = \mathbf{F}, \quad (3.10)$$

where \mathbf{r} is the defect position, \mathbf{F} is the net force acting on the defect, due to interaction with other defects or externally imposed perturbations, and \mathbf{v} the local flow velocity at the position of the defect, which includes both external and self-generated flows. Finally, ζ is an effective drag coefficient proportional to the rotational friction γ in Eq. (3.1c) and possibly space-dependent.

In the absence of fluid flow, an isolated disclination moves only in response to an externally imposed distortion and relaxes to the minimal energy texture θ_d given in Eq. (3.8). Following Denniston [53], one can then set $\theta = \theta_d + \theta_{\text{ext}}$, where θ_{ext} expresses the departure from the optimal defective configuration θ_d , and calculate the energy variation with respect to a small virtual displacement of the defect core. For small deformations, this gives $\mathbf{F} = -2\pi k K \nabla_{\perp} \theta_{\text{ext}}$, with $\nabla_{\perp} = (-\partial_y, \partial_x)$, and

$$\zeta = \pi \gamma k^2 \int_{\text{Er}}^{\infty} dx K_1^2(x) I_1(2x) \approx 226 \pi \gamma k^2, \quad (3.11)$$

where K_1 and I_1 are Bessel functions and $\text{Er} = \gamma a |\dot{\mathbf{r}}| / K$ is the Ericksen number at the length scale of the defect core. The second equality in Eq. (3.11) implies $a \approx 0$, while at finite core radius introduces a dependence of the effective friction ζ on the defect velocity. We refer the reader to Refs. [53, 59, 60] for details.

The hydrodynamic coupling between the local orientation of the director and the flow gives rise to a self-generated flow, known as *backflow*, that in turn advects the defect core. When the dynamics of the flow is much faster than the orientational dynamics of the director, and in the absence of external forces, one can neglect \mathbf{F} in Eq. (3.10) and calculate the flow velocity \mathbf{v} from the Stokes equation,

$$\eta \nabla^2 \mathbf{v} - \nabla p + \mathbf{f} = \mathbf{0}, \quad \nabla \cdot \mathbf{v} = 0, \quad (3.12)$$

where $\mathbf{f} = \mathbf{f}^a + \mathbf{f}^e = \nabla \cdot (\boldsymbol{\sigma}^a + \boldsymbol{\sigma}^r)$ is the force arising from the active and elastic stresses acting in the system. In the case of isolated defects this scenario is generally realistic for $\eta/\gamma \ll 1$ and even in a system containing multiple defects this purely advective dynamics continues to hold as long as the defects are sufficiently far apart (see Sec. 3.4). The general case in which both \mathbf{v} and \mathbf{F} are non-zero was discussed by Kats *et al.* [61].

In the remainder of this section we consider the regime in which $\eta/\gamma \ll 1$ and calculate the backflow due to the stresses arising in the presence of isolated $k = \pm 1/2$ disclinations. Let us then consider a $\pm 1/2$ disclination located at the origin of a circular domain of size R . The domain might represent either the entire system or, more realistically, the defect-free portion of the system surrounding a given central defect. We will refer to this as the *range* of a defect. Because of the linearity of the Stokes equation, the solution of Eq. (3.12) can be written as $\mathbf{v} = \mathbf{v}^0 + \mathbf{v}^a + \mathbf{v}^e$, where \mathbf{v}^0 is the solution of the homogeneous Stokes equation, while \mathbf{v}^a and \mathbf{v}^e are the flows produced by the active and elastic force, respectively. The solution can be expressed as the convolution of the two-dimensional Oseen tensor with the force per unit area,

$$v_i(\mathbf{r}) = \int dA' G_{ij}(\mathbf{r} - \mathbf{r}') f_j(\mathbf{r}'), \quad (3.13)$$

where G_{ij} is the two-dimensional Oseen tensor [62], given by

$$G_{ij}(\mathbf{r}) = \frac{1}{4\pi\eta} \left[\left(\log \frac{\mathcal{L}}{r} - 1 \right) \delta_{ij} + \frac{r_i r_j}{r^2} \right], \quad (3.14)$$

with \mathcal{L} a length scale adjusted to obtain the desired behavior at the boundary. Taking $\mathbf{n} = (\cos k\phi, \sin k\phi)$, with $k = \pm 1/2$, and assuming uniform concentration and nematic order parameter outside the defect core, the body force due to activity can be calculated straightforwardly as

$$\mathbf{f}^a = \nabla \cdot \boldsymbol{\sigma}^a = \frac{\alpha}{2r} \begin{cases} \hat{\mathbf{x}} & k = +1/2, \\ -\cos 2\phi \hat{\mathbf{x}} + \sin 2\phi \hat{\mathbf{y}} & k = -1/2, \end{cases}$$

where, for simplicity, we have assumed $S_0 = 1$ outside the core. Using this in Eq. (3.13), and using (3.14), yields, after some algebraic manipulation,

$$\mathbf{v}_+^a(r, \phi) = \frac{\alpha}{12\eta} \{ [3(R-r) + r \cos 2\phi] \hat{\mathbf{x}} + r \sin 2\phi \hat{\mathbf{y}} \}, \quad (3.15a)$$

$$\mathbf{v}_-^a(r, \phi) = \frac{\alpha r}{12\eta R} \left\{ \left[\left(\frac{3}{4}r - R \right) \cos 2\phi - \frac{R}{5} \cos 4\phi \right] \hat{\mathbf{x}} - \left[\left(\frac{3}{4}r - R \right) \sin 2\phi + \frac{R}{5} \sin 4\phi \right] \hat{\mathbf{y}} \right\}. \quad (3.15b)$$

A plot of these flow fields is shown in Fig. 3.2. Setting $\mathbf{v} = \mathbf{v}_+^a(0, \phi)$ in Eq. (3.10) we find that active $+1/2$ disclinations self-propel at constant speed along their symmetry axis ($\hat{\mathbf{x}}$ in this setting), and their equation of motion can be written as

$$\zeta \frac{dA_+}{dt} = v_0 \hat{\mathbf{x}}, \quad (3.16)$$

where $v_0 = \alpha R / (4\eta)$. On the other hand, $\mathbf{v}_-^a(0, \phi) = \mathbf{0}$, and so $-1/2$ disclinations are not propelled by the active backflow, but rather move solely under the effect of the elastic force produced by other defects. It is crucial to notice that the self-propulsion velocity v_0 scales linearly with the active stress α and so disclinations

in contractile ($\alpha > 0$) and extensile ($\alpha < 0$) active nematic suspensions self-propel in opposite directions.

Equations (3.15) can be complemented with various kinds of boundary conditions, which, however, have no effect on the qualitative feature of the solution and, more importantly, on the dynamics of the defects. To illustrate this point we consider a slippery interface, such that $v_r(R, \phi) = 0$ and $\sigma_{r\phi}^a = -\xi v_\phi(R, \phi)$, where ξ is the coefficient associated with the frictional force exerted by the interface on the fluid. If the domain of Eq. (3.12) is interpreted as a container, then ξ is the actual frictional coefficient of the container wall. On the other hand, if the domain is interpreted as the *range* of a defect, then $\xi \sim \eta h$, where h is the thickness of the boundary layer between the ranges of neighboring defects. No-slip boundary conditions can be recovered in the limit $\xi \rightarrow \infty$.

A solution \mathbf{v}^0 of the homogeneous Stokes equation enforcing the boundary conditions for the active backflow induced by the $+1/2$ disclination can be found from the following biharmonic stream function

$$\psi_+ = (a_1 r + b_1 r^3) \sin \phi, \quad (3.17)$$

with a_1 and b_1 constants. The corresponding velocity field $\mathbf{v}_+^0 = (\partial_y \psi, -\partial_x \psi)$ is given by

$$\mathbf{v}_+^0(r, \phi) = [a_1 + b_1 r^2 (2 - \cos 2\phi)] \hat{\mathbf{x}} - b_1 r^2 \sin 2\phi \hat{\mathbf{y}}. \quad (3.18)$$

Then, setting $\hat{\mathbf{r}} \cdot \mathbf{v}_+(R, \phi) = 0$ and $\hat{\phi} \cdot \mathbf{v}_+(R, \phi) = -\sigma_{r\phi}^{a+}(R, \phi)/\xi = \alpha/(2\xi) \sin \phi$, with $\mathbf{v}_+ = \mathbf{v}_+^0 + \mathbf{v}_+^a$, and solving for a_1 and b_1 yields

$$a_1 = -\frac{\alpha R}{6\eta} + \frac{\alpha}{4\xi}, \quad b_1 = \frac{\alpha}{12\eta R} - \frac{\alpha}{4\xi R^2}.$$

The associated self-propulsion velocity v_0 in Eq. (3.16) then becomes

$$v_0 = \alpha \left(\frac{R}{12\eta} + \frac{1}{4\xi} \right), \quad (3.19)$$

or $v_0 = \alpha R/(12\eta)$ in the no-slip limit. Thus, as anticipated, incorporating the effect of the boundary only changes the speed of the defects, without altering their dynamics. Similarly, in the case of a $-1/2$ disclination, we can consider the biharmonic stream function

$$\psi_- = (a_3 r^3 + b_3 r^5) \sin 3\phi, \quad (3.20)$$

whose associated velocity field is given by

$$\begin{aligned} \mathbf{v}_-^0(r, \phi) = & \left[r^2(3a_3 + 4b_3 r^2) \cos 2\phi - b_3 r^4 \cos 4\phi \right] \hat{\mathbf{x}} \\ & - \left[r^2(3a_3 + 4b_3 r^2) \sin 2\phi + b_3 r^4 \sin 4\phi \right] \hat{\mathbf{y}}. \end{aligned} \quad (3.21)$$

Setting $\hat{\mathbf{r}} \cdot \mathbf{v}_-(R, \phi) = 0$ and $\hat{\boldsymbol{\phi}} \cdot \mathbf{v}_-(R, \phi) = -\sigma_{r\phi}^{\text{a-}}(R, \phi)/\xi = \alpha/(2\xi) \sin 3\phi$ and solving for a_3 and b_3 yields

$$a_3 = \frac{7\alpha}{240\eta R} + \frac{\alpha}{4\xi R^2}, \quad b_3 = -\frac{\alpha}{60\eta R^3} - \frac{\alpha}{4\xi R^4}.$$

Clearly this does not change the symmetry of the active backflow, and thus negative-charge disclinations are stationary.

In summary, half-strength disclinations in active nematic liquid crystals can be described as self-propelled particles with overdamped dynamics governed by an equation of the form (3.10). In the absence of external forces, or forces due to interactions with other defects, the disclination core is advected at constant speed by a self-generated backflow provided the dynamics of the flow is faster than the

relaxational dynamics of the director (i.e. $\eta/\gamma \ll 1$). As a result, positive disclinations travel along their symmetry axis at speed $v_0 \sim \alpha R/\eta$, while negative disclinations are stationary and move only as a consequence of their interaction with other disclinations. The direction of motion is controlled by the sign of the activity α , which in turns depends on whether the system is contractile ($\alpha > 0$) or extensile ($\alpha < 0$). Thus the comet-like $+1/2$ disclination travels in the direction of its “tail” in contractile systems and in the direction of its “head” in extensile systems. We note that active curvature currents in the concentration equation controlled by the parameter α_1 have a similar effect, as noted by Narayan *et al.* in a system of vibrated rods [11] and recently investigated by Shi and Ma through extensive numerical simulations [41]. Such curvature driven currents control the dynamics in systems with no momentum conservation, but are very small in the regime discussed here.

Special attention should be devoted to the fact that the self-propulsion speed v_0 depends linearly on the range R of a defect, this being defined as the defect-free portion of the system surrounding a defect (and possibly coinciding with the entire system). Although two-dimensional hydrodynamics is known to be plagued with anomalies, such as the Stokes paradox [63], this behavior does not result solely from the two-dimensionality of the problem. Point defects in three dimensions would also yield a similar behavior. To see this we note that the deviatoric part of the Oseen tensor scales like r^{2-D} , with D the space dimension. On the other hand, the active force $\mathbf{f}^a = \alpha \nabla \cdot \mathbf{Q}$ always scales like r^{-1} . The backflow velocity in D dimensions thus scales like $v^a \sim \int_0^R d^D r r^{2-D} r^{-1} = R$, regardless of the space dimension. In three dimensions disclinations are, however, line defects. In this case, denoting by ξ_d the persistence length of the disclinations, i.e., the length scale over which these line defects can be treated as straight lines, the length R controlling the flow velocity induced by a $+1/2$ defect would scale as $R \sim \xi_d \log(L/a)$, with L the system size and a the core radius. These results

could also be obtained on the basis of dimensional analysis by noting that \mathbf{v}^a is always proportional to α/η . Since α has dimensions of stress and η has dimensions of stress over time, the resulting velocity must also be proportional to a length scale. This length scale was first noted experimentally by Sanchez *et al.* [3] and investigated numerically by Thampi *et al.* [18, 20]. Its nature, however, remains elusive (see Sec. 3.5 for further discussion on this matter).

The growth of the flow field generated by a defect at large distances can also be cut off by a frictional force $\mathbf{f}_s = -\zeta_s \mathbf{v}$ as may arise from the fact that the nematic film is confined at an oil/water interface [64]. Such a frictional interaction with the subphase removes energy from the flow at the length scale $\ell_s = \sqrt{\eta/\zeta_s}$, thus controlling the decay of the velocity field. Finally, the limit where the friction dominates viscous forces corresponding to a no-slip Hele-Shaw geometry has been discussed in detail by Pismen [38]. In this case the flow generated by a single disclination is found to decay as $\sim r^{-3}$ at large distances from the defect.

3.4 Annihilation dynamics of defect pairs

In this section we discuss the annihilation of a pair of oppositely charged disclinations. The study of the annihilation dynamics of defect-antidefect pairs is a mature topic in the liquid crystals field and has been subject to numerous investigations [53, 59, 42, 65, 66, 67, 68]. In the simplest setting [34], one considers a pair of $k = \pm 1/2$ disclinations located at $\mathbf{r}_\pm = (x_\pm, 0)$ and separated by a distance $\Delta = x_+ - x_-$ (Fig. 3.3). The energy of the pair is given by

$$E_{\text{pair}} = 2\pi k^2 K \log(\Delta/a) + 2\epsilon_c . \quad (3.22)$$

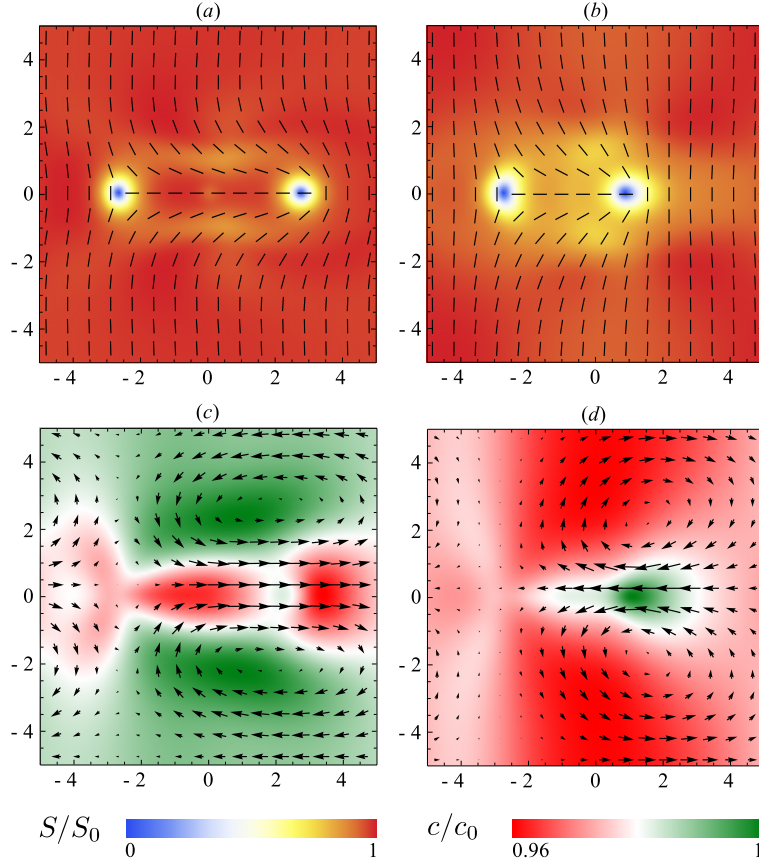


FIGURE 3.3: Snapshots of a disclination pair shortly after the beginning of relaxation. (Top) Director field (black lines) superimposed on a heat map of the nematic order parameter and (bottom) flow field (arrows) superimposed on a heat map of the concentration for an extensile system with $\alpha = -0.8$ (a),(c) and a contractile system with $\alpha = 0.8$ (b),(d). In the top images the color denotes the magnitude of the nematic order parameter S relative to its equilibrium value $S_0 = \sqrt{1 - c^*/c_0} = 1/\sqrt{2}$. In the bottom images the color denotes the magnitude of the concentration c relative to the average value $c_0 = 2c^*$. Depending on the sign of α , the backflow tends to speed up ($\alpha > 0$) or slow down ($\alpha < 0$) the annihilation process by increasing or decreasing the velocity of the $+1/2$ disclination. For α negative and sufficiently large in magnitude, the $+1/2$ defect reverses its direction of motion (c) and escapes annihilation.

Each defect experiences an elastic force of the form $\mathbf{F}_{\pm} = -(\partial E_{\text{pair}}/\partial x_{\pm}) \hat{\mathbf{x}}$ and thus, in the absence of backflow, Eq. (3.10) can be cast in the form

$$\frac{dx_{\pm}}{dt} = \mp \frac{\kappa}{x_+ - x_-}, \quad (3.23)$$

where $\kappa = 2\pi k^2 K/\zeta$. This yields

$$\frac{d\Delta}{dt} = -\frac{2\kappa}{\Delta}, \quad (3.24)$$

so that the distance between annihilating defects decreases as a square-root, $\Delta(t) \propto \sqrt{t_a - t}$, with t_a the annihilation time. More precise calculations have shown that the effective friction is itself a function of the defect separation [59, 60], $\zeta = \zeta_0 \log(\Delta/a)$, although this does not imply substantial changes in the overall picture. This simple model predicts that the defect and antidefect approach each other along symmetric trajectories and annihilate at $\Delta(0)/2$ in a time $t_a = \Delta^2(0)/4\kappa$. The backflow produced by the balance of elastic and viscous stresses [42, 68], as well as the anchoring conditions at the boundary [65], can produce an asymmetry in the trajectories of the annihilating defects or even suppress annihilation when the defects are initially far from each other or the anchoring is sufficiently strong.

To understand how activity changes the simple annihilation dynamics described so far, we have integrated numerically Eqs. (3.1) for an initial configuration of uniform concentration and zero flow velocity, with two disclinations of charge $\pm 1/2$ symmetrically located with respect to the center of the box along the x -axis. Fig. 3.3 shows a snapshot of the order parameter and flow field shortly after the beginning of the relaxation for both a contractile and extensile system, with $\alpha = \pm 0.8$ in the units defined in Sec. 3.2.3.

In contractile systems active backflow yields a net speed-up of the $+1/2$ defect towards its antidefect for the annihilation geometry shown in Fig. 3.3b. In extensile systems, with $\alpha < 0$, backflow drives the $+1/2$ defect to move towards its head, away from its $-1/2$ partner in the configuration of Fig. 3.3b, acting like an effectively *repulsive* interaction. If the initial positions of the defects are exchanged, the behavior is reversed. The effective attraction or repulsion between oppositely

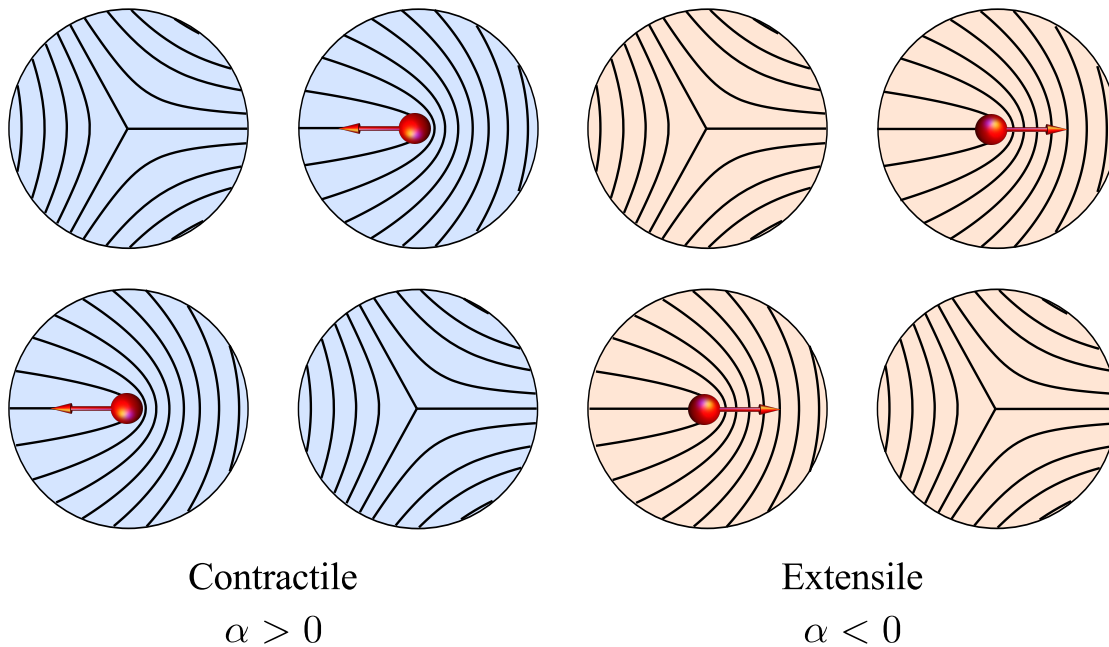


FIGURE 3.4: Schematic representation of the effective attractive/repulsive interaction promoted by the active backflow. Depending on the sign of the active stress α , $+1/2$ disclinations self-propel in the direction of their “tail” (contractile) or “head” (extensile). Based on the mutual orientation of the defects, this can lead to an attractive or repulsive interaction.

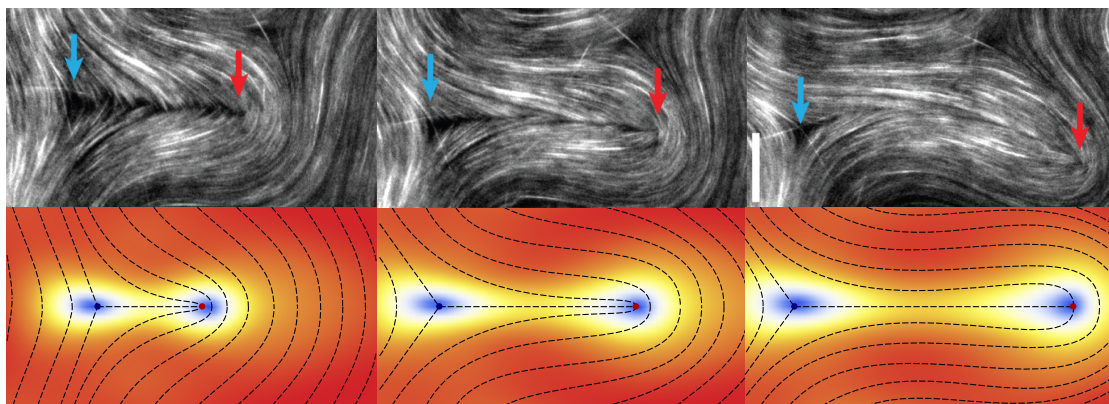


FIGURE 3.5: Defect pair production in an active suspension of microtubules and kinesin (top) and the same phenomenon observed in our numerical simulation of an extensile nematic fluid with $\gamma = 100$ and $\alpha = -2$. The experimental pictures are reprinted with permission from T. Sanchez *et al.*, *Nature (London)* 491, 431 (2012). Copyright 2012, Macmillan.

charged active defects is thus dictated by both the contractile or extensile nature of the active stresses, which determines the direction of the backflow, and the relative orientation of the defects, as summarized in Fig. 3.4. This effect has been observed in experiments with extensile microtubules and kinesin assemblies [3] and can be understood on the basis of the hydrodynamic approach embodied in

Eqs. (3.1). In Fig. 3.5 we have reproduced from Ref. [3] a sequence of snapshots showing a pair of $\pm 1/2$ disclinations moving apart from each other together with the same behavior observed in our simulations.

Figs. 3.6a and 3.6b show the trajectories of the active defects, with the red and blue line representing the $+1/2$ and $-1/2$ disclination respectively. The tracks end when the cores of the two defects merge. For small activity and small values of the rotational friction γ , the trajectories resemble those obtained for passive systems [42, 68]. At large values of activity, however, the asymmetry in defect dynamics becomes more pronounced, and when the activity dominates over orientational relaxation, the $+1/2$ disclination moves independently along its symmetry axis with a speed $v_0 \sim \alpha R/\eta$ (see Sec. 3.3) whose direction is dictated by the sign of α . This behavior is clearly visible in Fig. 3.6c, showing the defect separation $\Delta(t)$ as a function of time. For γ sufficiently large, the trajectories are characterized by two regimes. For large separation the dynamics is dominated by the active backflow, and thus $\dot{\Delta}(t) \propto -\alpha$ and $\Delta(t) \propto -\alpha t$. Once the defects are about to annihilate, the attractive force takes over, and the defects behave as in the passive case with $\Delta(t) \propto \sqrt{t_a - t}$.

This behavior can be understood straightforwardly from the basic concepts of active defect dynamics discussed in Sec. 3.3. Each defect in the pair travels in space according to Eq. (3.10), with \mathbf{v} given by $\mathbf{v}(x) = \mathbf{v}_+^a(x - x_+) + \mathbf{v}_-^a(x - x_-)$ and \mathbf{v}_\pm given in Eqs. (3.15) plus a suitable homogeneous solution of the Stokes equation that enforces the periodic boundary conditions. Next, we retain only the active contribution to the backflow and replace the flow profiles by their constant values at the core of the defect, with $\mathbf{v}_+(x_+) = v_0 \hat{\mathbf{x}} \propto \alpha$ and $\mathbf{v}_-(x_-) = \mathbf{0}$. This yields the following simple equation for the pair separation

$$\frac{d\Delta}{dt} = v_0 - \frac{2\kappa}{\Delta}. \quad (3.25)$$

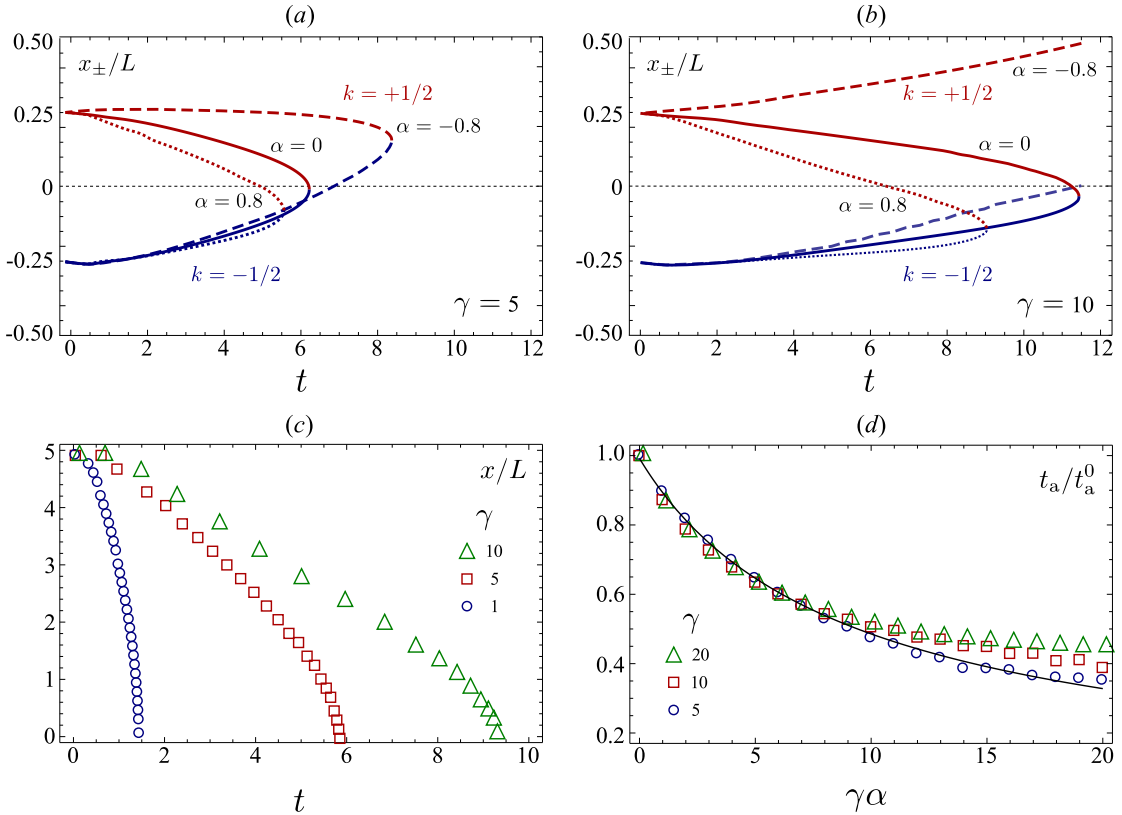


FIGURE 3.6: Defect trajectories and annihilation times obtained from a numerical integration of Eqs. (3.1) for various γ and α values. (a) Defect trajectories for $\gamma = 5$ and various α values (indicated in the plot). The upper (red) and lower (blue) curves correspond to the positive and negative disclination, respectively. The defects annihilate where the two curves merge. (b) The same plot for $\gamma = 10$. Slowing down the relaxational dynamics of the nematic phase increases the annihilation time and for $\alpha = -0.8$ reverses the direction of motion of the $+1/2$ disclination. (c) Defect separation as a function of time for $\alpha = 0.8$ and various γ values. (d) Annihilation time normalized by the corresponding annihilation time obtained at $\alpha = 0$ (i.e., t_a^0). The line is a fit to the model described in the text.

This equation explicitly captures the two regimes shown in Fig. 3.6(c) and described earlier. The solution takes the form

$$\Delta(t) = \Delta(0) + v_0 t - \frac{2\kappa}{v_0} \log \left[\frac{\Delta(t) - \frac{2\kappa}{v_0}}{\Delta(0) - \frac{2\kappa}{v_0}} \right]. \quad (3.26)$$

The pair annihilation time t_a is determined by $\Delta(t_a) = 0$ and is given by

$$t_a = -\frac{\Delta(0)}{v_0} - \frac{2\kappa}{v_0^2} \log \left[1 - \frac{v_0}{2\kappa} \Delta(0) \right]. \quad (3.27)$$

For passive systems ($\alpha = 0$) this reduces to $t_a^0 = \Delta^2(0)/4\kappa$. This predicts that the annihilation time, normalized to its value in passive systems, t_a/t_a^0 , depends only on $\Delta(0)v_0/2\kappa \sim \alpha\gamma$. Figure 3.6d shows a fit of the annihilation times extracted from the numerics to this simple formula. The model qualitatively captures the numerical behavior.

3.5 Defect proliferation

Pair annihilation is the fundamental mechanism behind defect coarsening in nematic liquid crystals [58]. Once this mechanism is suppressed by activity, as described in Sec. 3.4, the coarsening dynamics is replaced by a new steady state in which pairs of $\pm 1/2$ disclinations are continuously produced and annihilated at constant rate. The chaotic dynamics following from the continuous defect proliferation and annihilation results in a turbulent flow [49, 18, 19, 20, 21]. In this section we describe the onset of chaos and the proliferation of defects that are observed from numerical solutions of Eqs. (3.1) upon varying the activity parameter α and the rotational friction γ . As initial configurations we take a homogeneous state with the director field aligned along the x -axis and subject to a small random perturbation in density and orientation. The equations were then integrated from $t = 0$ to $t = 2 \times 10^3\tau$ (see Sec. 3.2.3 for a description of units).

Fig. 3.7 summarizes the various regimes obtained by exploring the (α, γ) -plane: 1) a homogeneous, quiescent ordered state; 2) a periodic flow marked by the emergence of relaxation oscillations; 3) a non-periodic oscillatory flow characterized by the formation of “walls” in the nematic phase and the unzipping of these walls through the unbinding of defect pairs; 4) a chaotic or “turbulent” state associated with a constant defect density. The latter three regimes are described in more detail in the following.

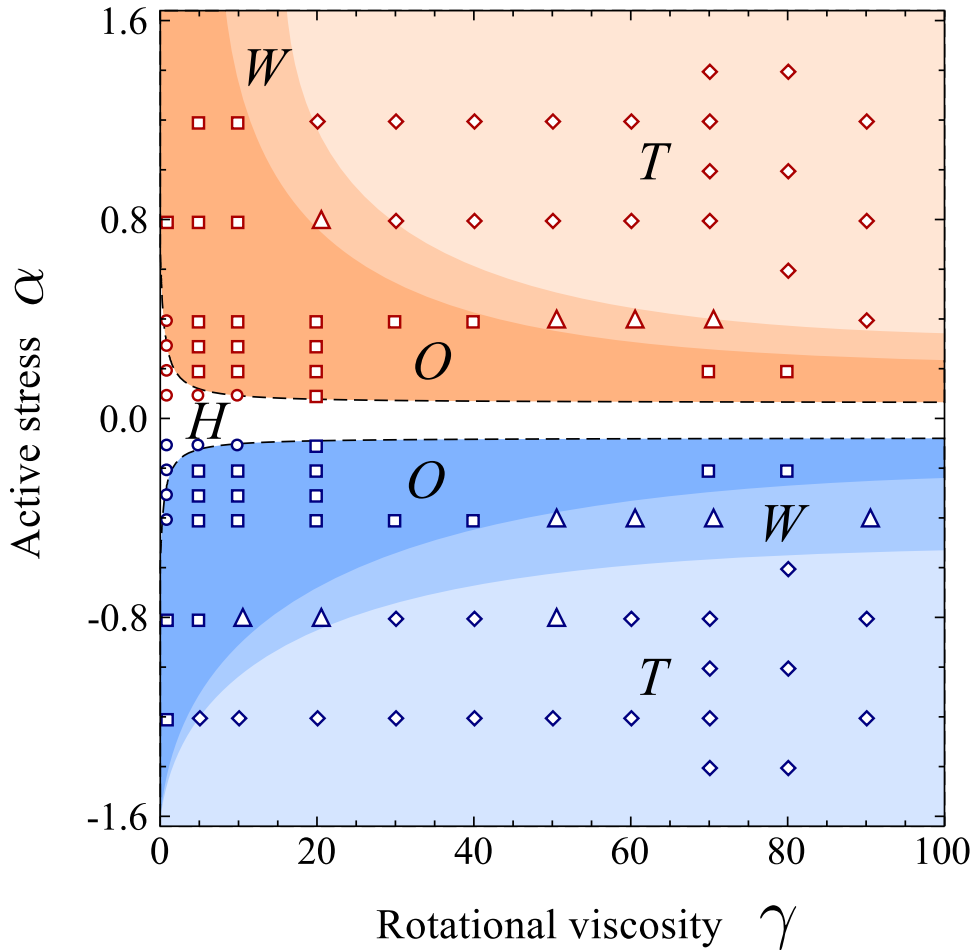


FIGURE 3.7: Phase diagram showing the various flow regimes of an active nematic obtained by varying activity α and rotational friction γ for both contractile ($\alpha > 0$) and extensile ($\alpha < 0$) systems. The dashed lines bounding the region where the homogeneous ordered state (H) is stable are the boundaries of linear stability given in Eq. (3.5). With increasing activity, the system exhibits relaxation oscillations (O), non-periodic oscillations characterized by the formation and unzipping of walls (W), and turbulence (T).

3.5.1 Relaxation Oscillations

As described in Refs. [15, 16], relaxation oscillations occur in active nematics when $|\alpha|$ exceeds α_2^\pm as the result of the competition of two time scales: the relaxation $\tau_p = \gamma \ell^2 / K$ of the nematic structure and the time scale $\tau_a = \eta / |\alpha|$ that controls the rate at which active stresses are injected in the system. When $\tau_p < \tau_a$, the microstructure can relax to accommodate the active forcing and the ordered state is stable. This is a quiescent state, with uniform order parameter. Conversely,

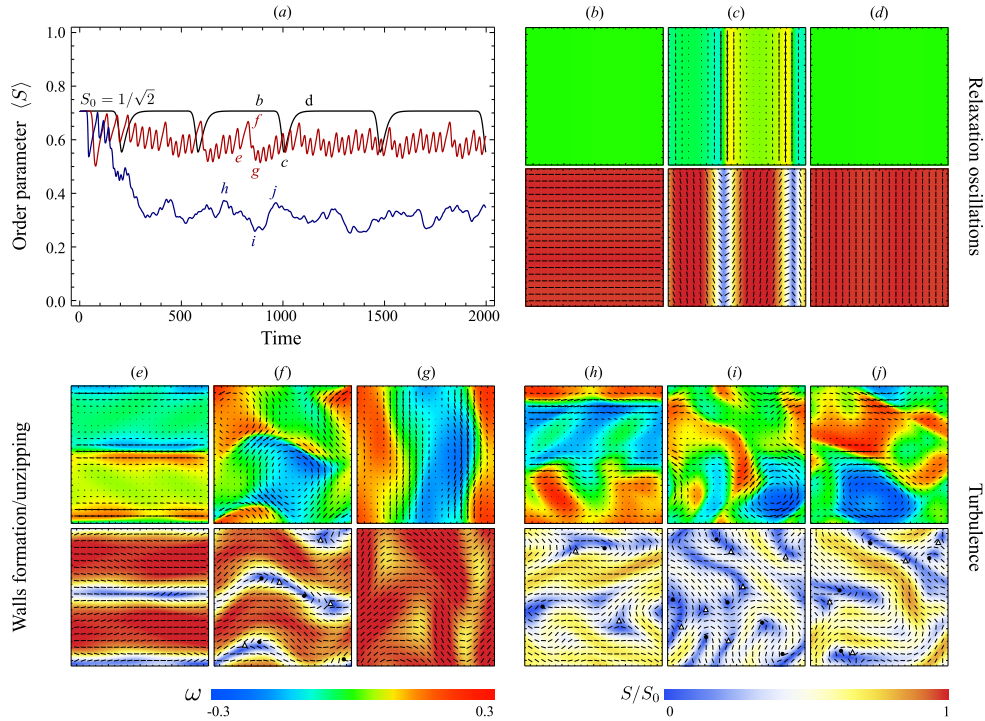


FIGURE 3.8: Dynamical states obtained from a numerical integration of Eqs. (3.1) with $\gamma = 20$ and various values of activity for an extensile system. (a) Average nematic order parameter versus time. The black line for $\alpha = -0.3$ identifies the relaxation oscillations regime with the labels (b), (c) and (d) marking the times corresponding to the snapshots on the top-left panel. The red line for $\alpha = -0.8$ indicates the non-periodic oscillatory regimes characterized by the formation of walls (e) and the unzipping of walls through the unbinding of defect pairs: (f) and (g). The symbols \bullet and \triangle mark the positions of $+1/2$ and $-1/2$ disclinations respectively. The blue line for $\alpha = -1.2$ corresponds to the turbulent regime in which defects proliferate: (h), (i) and (j). In all the snapshots, the background colors are set by the magnitude of the vorticity ω and the order parameter S rescaled by the equilibrium value $S_0 = 1/\sqrt{2}$, while the solid lines indicate velocity (top) and director field (bottom). Movies displaying the time evolution of each state are included as the Supplementary Material.

when $\tau_p > \tau_a$, the relaxation of the nematic structure lags behind the injection of active stresses, yielding various dynamical states with spatially and temporally inhomogeneous order parameters.

In this regime the dynamics consists of a sequence of almost stationary passive periods separated by active “bursts” in which the director switches abruptly between two orthogonal orientations (Fig. 3.8b-d). During passive periods, the particle concentration and the nematic order parameter are nearly uniform across the system, there is no appreciable flow, and the director field is either parallel or

perpendicular to the x direction (due to the initial conditions). Eventually this configuration breaks down and the director field rotates by 90° . The rotation of the director field is initially localized along narrow extended regions, generating flowing bands similar to those obtained in active nematic films [6] (Fig. 3.8c). The temporary distortion of the director field as well as the formation of the bands is accompanied by the onset of flow along the longitudinal direction of the bands, with neighboring bands flowing in opposite directions. The flow terminates after the director field rotates and a uniform orientation is restored. The process then repeats.

Depending on whether the active stress fueling the oscillatory dynamics is contractile or extensile, the rotation of the director occurs through an intermediate splay or bending deformation. During bursts, the nematic order parameter, otherwise equal to its equilibrium value, drops significantly (Fig. 3.8a, black line). Without this transient melting the distortions of the director field required for a burst are unfavorable for any level of activity.

The frequency of the oscillation is proportional to $k^2\alpha$, where $k = 2\pi/L$ is the wave number of the longest-wavelength mode to go unstable [15, 16]. In spite of the strong elastic deformation and the dramatic drop in the order parameter, this regime contains no unbound defects.

3.5.2 Wall formation and unzipping

For larger values of activity the bend and splay deformations of the director at the band boundaries become large enough to drive creation of defect pairs, as shown in Fig. 3.8e-g. The alignment of the bands again oscillates between two orthogonal directions (x - and y -axis for the initial condition used here), but the switching takes place through an intermediate more complex configuration with lozenge-shaped ordered regions. Defect pairs then unbind and glide along the

narrow regions separating two bands where elastic deformations and shear flows are largest. These regions of high distortion and shear rate are commonly referred to as “walls” in the liquid crystals literature [69]. Movies displaying the dynamics of wall unzipping and defect creation for both extensile and contractile systems are included as Supplementary Material.

The formation of walls and the “unzipping” of defects along the walls by the creation of pairs of $\pm 1/2$ disclinations has been discussed in detail by Thampi *et al.* [19] (see also Ref. [20] in this Themed Issue). Defect unbinding along the walls relaxes both the excess elastic energy and the high shear stresses present in these regions, where the nematic order parameter S is driven near zero. For this reason wall formation and unzipping occurs often at the boundary between pairs of vortices of opposite circulation (Fig. 3.9). In passive nematic liquid crystals the strong bending deformation that leads to the formation of walls, and precedes defect unbinding, requires an external action, such as an applied electric field or an externally imposed shear stress [70]. In active nematics, on the other hand, a similar complex spatiotemporal dynamics occurs spontaneously, driven by the *local* injection of active stresses, which are in turn balanced by spontaneous distortions and flows as described in Section 3.2.2. Wall formation and unzipping also combines here with the oscillatory dynamics described in Section 3.5.1 to give rise to the periodic creation and annihilation of topological defects that marks the transition to the turbulent regime.

Oscillating band structures of the type observed here are found in passive nematic fluids under externally applied shear flows and are precursors to rheochaos [71, 72]. They have been predicted theoretically [73] and observed experimentally [74] in suspensions of wormlike micelles, where the spatiotemporal dynamics is directly correlated to shear banding [75] and to stress/shear fluctuations at the shear band interface. In passive systems it has been argued that the route to rheochaos depends on whether the stress or the strain rate is controlled during the experiment.

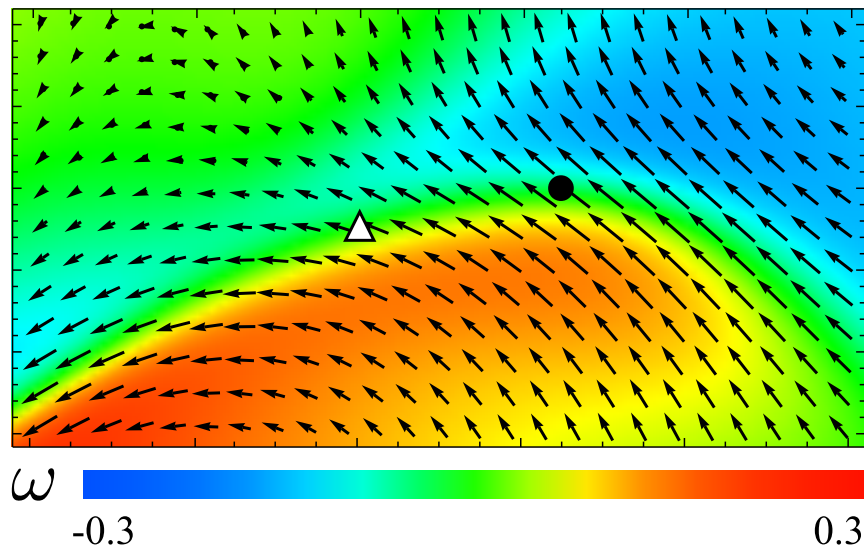


FIGURE 3.9: A magnification of the snapshot of Fig. 3.8f, showing the creation of a $+1/2$ (\bullet) and a $-1/2$ (\triangle) defect pair along a wall or $\alpha = -0.8$ and $\gamma = 20$. The black arrows indicate the flow velocity, while the background color is related with the local vorticity. The wall is also the boundary between a pair of vortices of opposite circulation. The flow field of opposite-signed vortices adds at the wall, yielding a region of high shear that promotes defect unbinding.

It would be interesting to analyze in more detail the route to chaos in this case.

3.5.3 Turbulence

At even higher activity the bands/walls structure begins to bend and fold and the dynamics becomes chaotic, resembling that of a “turbulent” fluid, as displayed in Fig. 3.8h-j and in the movies included as Supplementary Material. The system reaches a dynamical steady state where defect pairs are continuously created and annihilated, but their mean number remains on average constant in time. Due to topological charge conservation, at any time the system contains an equal number of positive and negative defects. Unlike in equilibrium systems, however, in active nematics it is possible for opposite-charge defects of certain orientations to repel instead of attracting (see Sec. 3.4). This allows the formation of a defect-filled steady state, with self-sustained flows and a constant mean number of defects.

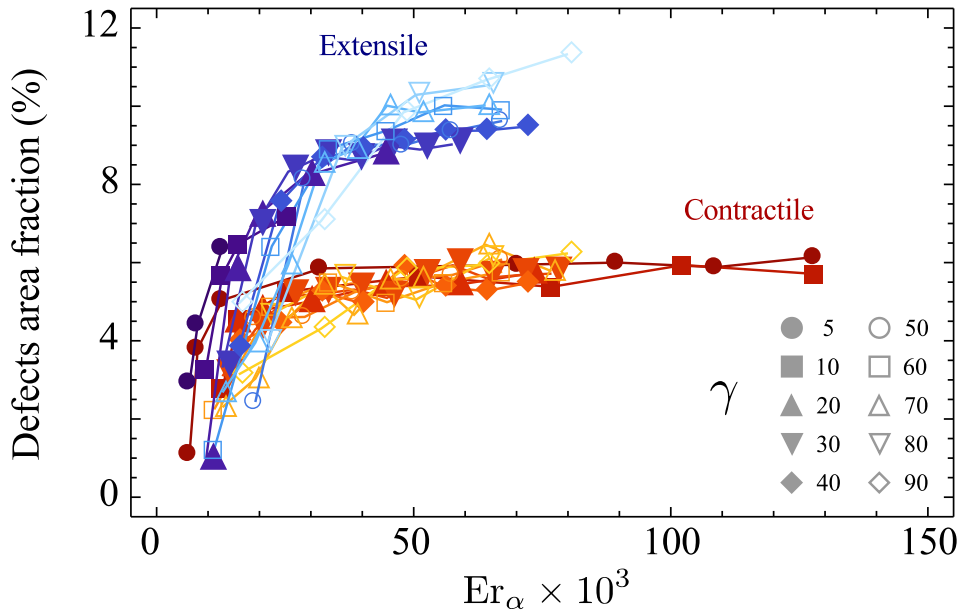


FIGURE 3.10: Defects area fraction $N\pi a^2/L^2$ as a function of the active Ericksen number $Er_\alpha = \alpha\gamma L^2/(\eta K)$ for contractile (symbols in red tones) and extensile (symbols in blue tones) systems. In both cases the area fraction saturates when the activity increase is compensated by a drop of the order parameter which effectively reduces the injected active stress.

The defect-filled dynamics observed in the system is similar to that obtained in a passive nematic subject to an externally imposed shear or to electrohydrodynamic instabilities [76]. In active nematics, however, defects are generated in the absence of any externally imposed forces or constraints, as a result of the spontaneous distortion induced by the active stresses. After formation the defects are convected by the swirling flow and interact with one another through distortional elasticity as well as hydrodynamically through the modifications the defects themselves induce on the flow field.

The sequence of flow regimes observed here is reminiscent of the evolution of the dynamics of sheared tumbling nematic polymers with increasing shear rate, known as the Ericksen number cascade [77]. In a nematic film sheared at a rate $\dot{\epsilon}$ between two plates separated by a distance h , the Ericksen number Er provides a dimensionless measure of the magnitude of viscous torques ($\sim \dot{\epsilon}$) relative to elastic torques arising from spatial gradients in the average molecular orientation

($\sim K/\gamma h^2$), with $\text{Er} = \dot{\epsilon}\gamma h^2/K$. This suggests the definition of an *active* Ericksen number Er_α where the active stress α takes the place of viscous stresses $\eta\dot{\epsilon}$. The active Ericksen number is then defined as $\text{Er}_\alpha = \alpha\gamma L^2/(\eta K)$. With this definition, Er_α can also be interpreted as the ratio of the time scale $\tau_p = \gamma L^2/K$ for the relaxation of an orientational deformation of the nematic order on the scale of the entire system to the time $\tau_a = \eta/\alpha$ controlling the injection of active stresses.

Fig. 3.10 shows a plot of the *area fraction* occupied by defects as a function of the active Ericksen number Er_α for both extensile and contractile systems. The area fraction is defined as the relative area occupied by the core of the defects, or $N\pi a^2/L^2$, with N the number of defects. The core radius a resulting from the hydrodynamic equations (3.1) is approximatively given by the size of the boundary layer between the position of a defect, where $S = 0$, and surrounding space, where $S = S_0$. This is proportional to the coefficient A in the Landau-de Gennes free energy (3.2)

$$a = \sqrt{\frac{K}{|A|}} \approx \frac{1}{\sqrt{|c_0 - c^*|}} \approx \ell. \quad (3.28)$$

For larger activity the reduction of the nematic order parameter due to the unbound defects compensates the activity increase by effectively reducing the injected local stress $\sigma^a \approx \alpha S$.

For the same magnitude of activity, extensile systems contain a larger mean number of defects than contractile ones. In both case defects pairs first unbind within the walls, which are regions of large bend and splay deformations in extensile and contractile systems, respectively. As the system evolves toward the regime of chaotic dynamics, the walls begin to deform largely via bend deformations in both systems [19, 20]. This asymmetry could be because the severe splay deformations localized at the walls lead to a more drastic reduction of the nematic order parameter. Thus contractile flow-tumbling nematics, whose spontaneous distortion

involves mostly splay deformations, are effectively less active than flow-tumbling extensile systems.

3.6 Discussion and Conclusions

We have presented a detailed analytical and numerical study of the mechanics of topological defects in active nematic liquid crystals. Topological defects are distinctive signatures of liquid crystals and profoundly affect their viscoelastic behavior by constraining the orientational structure of the fluid in a way that inevitably requires system-wide (global) changes not achievable with any set of local deformations. In ordered states of both passive and active nematics, the topological defects are fingerprints of the broken symmetry in the ordered state. In particular, the presence of strength $\pm 1/2$ defects clearly reveals the nematic nature of the orientational order, in contrast to systems with polar (ferromagnetic) symmetry where the lowest energy defects allowed have strength ± 1 . Active liquid crystals have the additional feature that defects act as local sources of motion, behaving as self-propelled particle-like objects (see Sec. 3.3). The direction of motion of the strength $+1/2$ defects provides, furthermore, a clear signature of the extensile or contractile nature of the active stresses, as the comet-like positive defects are advected towards their head in extensile systems and towards their tail in contractile ones. In passive liquid crystals defect dynamics is always transient, as oppositely charged defects attract and eventually annihilate. In active nematics, on the other hand, the interplay between active and viscous stresses, modulated by the director geometry induced by the defects, enriches the spectrum of defect-defect interactions by allowing for an effective repulsion between defects and anti-defects (see Sec. 3.4). For highly active systems this mechanism can arrest the process of coarsening, leading to a state where unbound pairs of

defects are continuously created and annihilated, but with their mean density constant in time (see Sec. 3.5). The chaotic dynamics originating from the continuous defect proliferation and annihilation results in spontaneous low Reynolds number turbulence, akin to the so-called director turbulence seen in sheared polymer and micellar nematics [77].

Several open questions remain concerning the defect dynamics of active nematics. The defect area fraction shown in Fig. 3.10 exhibits a crossover from growth at low activity to saturation at high activity, but an understanding of the length scales that control this behavior is still lacking. Both our work and work by Thampi *et al.* [20] suggest that the mean separation between defects in the turbulent regime coincides with the typical vortex size, but more work is needed to elucidate the behavior of this length scale with activity over a wide range of parameters. While defect generation in sheared nematics has been explained in terms of a simple rate equation that balances creation and annihilation [77], a similar simple model for active defects is still missing. On the basis of numerics, Thampi *et al.* have suggested that the defect creation rate should scale like the square of the activity [20], but no simple argument is available to understand this counterintuitive result. Finally, an important open question is the different behavior of extensile and contractile systems apparent from Fig. 3.10. The turbulent state of contractile systems is much less defective than that of extensile ones, suggesting that for equal magnitude of the activity α , contractile nematics are effectively “less active” than extensile ones. Some of these questions we will address in the next chapters.

Acknowledgment

We thank Zvonimir Dogić, Jean-Francois Joanny, Oleg Lavrentovich, and Tim Sanchez for several illuminating discussions. LG was supported by SISSA math-Lab. The work at Syracuse was supported by the National Science Foundation

through awards DMR-1305184 (MCM, PM) and DGE-1068780 (MCM) and by funds from the Soft Matter Program. MCM also acknowledges support from the Simons Foundation. Finally, MCM and MJB thank the KITP at the University of California, Santa Barbara, for support during the preparation of the manuscript.

Appendix A

A.1 Active backflow of $+1/2$ disclinations

Finding the backflow produced by the positive disclination reduces then to calculate the following two integrals:

$$I_1 = \int dA' \frac{1}{r'} \left(\log \frac{D}{|\mathbf{r} - \mathbf{r}'|} - 1 \right), \quad (\text{A.1a})$$

$$I_2 = \int dA' \frac{1}{r'} \frac{(r_i - r'_i)(x - x')}{|\mathbf{r} - \mathbf{r}'|^2}. \quad (\text{A.1b})$$

To calculate the first integral, we can make use of the following logarithmic expansion:

$$\log \frac{|\mathbf{r} - \mathbf{r}'|}{\mathcal{L}} = \log \left(\frac{r_{>}}{\mathcal{L}} \right) - \sum_{n=1}^{\infty} \frac{1}{n} \left(\frac{r_{<}}{r_{>}} \right)^n \cos[n(\phi - \phi')], \quad (\text{A.2})$$

where $r_{>} = \max(|\mathbf{r}|, |\mathbf{r}'|)$ and $r_{<} = \min(|\mathbf{r}|, |\mathbf{r}'|)$. The integral over the angle can be immediately carried out using the orthogonality of trigonometric functions: $\int_0^{2\pi} d\phi' \cos[n(\phi - \phi')] = \delta_{n0}$. The remaining radial integral is easy to compute:

$$\int dr' \log \left(\frac{r_{>}}{\mathcal{L}} \right) = r - R + R \log \left(\frac{R}{\mathcal{L}} \right). \quad (\text{A.3})$$

Thus:

$$I_1 = -2\pi \left[r + R \log \left(\frac{R}{\mathcal{L}} \right) \right].$$

To calculate the integral I_2 , we can make use of the fact that:

$$\frac{r_i - r'_i}{|\mathbf{r} - \mathbf{r}'|^2} = \frac{\partial}{\partial r_i} \log |\mathbf{r} - \mathbf{r}'|. \quad (\text{A.4})$$

Thus one can write:

$$I_2 = x \frac{\partial}{\partial r_i} \int dr' d\phi' \log |\mathbf{r} - \mathbf{r}'| - \frac{\partial}{\partial r_i} \int dr' d\phi' x' \log |\mathbf{r} - \mathbf{r}'|. \quad (\text{A.5})$$

The first integral is calculated straightforwardly from I_2 :

$$x \frac{\partial}{\partial r_i} \int dr' d\phi \log |\mathbf{r} - \mathbf{r}'| = \frac{2\pi x r_i}{r}. \quad (\text{A.6})$$

The second integral, on the other hand, can be computed with the help of the logarithmic expansion (A.2):

$$\int dr' d\phi' r \cos \phi' \log |\mathbf{r} - \mathbf{r}'| = -\pi \cos \phi \int_0^R dr' r' \frac{r_{<}}{r_{>}} = -\pi r \cos \phi \left(R - \frac{2}{3} r \right), \quad (\text{A.7})$$

where we have used again the orthogonality of trigonometric functions:

$$\int_0^{2\pi} d\phi' \cos n(\phi - \phi') \cos m\phi' = \pi \cos m\phi \delta_{nm}. \quad (\text{A.8})$$

Thus taking the derivative and combining with Eq. (A.6), yields:

$$I_2 = \frac{4\pi}{3} \frac{x r_i}{r} + \pi \left(R - \frac{2}{3} r \right) \delta_{ix}. \quad (\text{A.9})$$

Adding together I_1 and I_2 and switching to polar coordinates gives:

$$v_x = \frac{\alpha}{12\eta} \left\{ \left[3 \left(\frac{3R}{2} + 3R \log \frac{\mathcal{L}}{R} - r \right) + r \cos 2\phi \right] \right\}, \quad (\text{A.10a})$$

$$v_y = \frac{\alpha}{12\eta} r \sin 2\phi. \quad (\text{A.10b})$$

Setting $\mathcal{L} = R\sqrt{e}$ and expressing everything in polar coordinates one finally gets Eq. (3.15a).

A.2 Active backflow of $-1/2$ disclinations

The calculation of the active backflow associated with a negative disclination reduces to the calculation of the following integrals:

$$I_3 = \int dA' \frac{1}{r'} \left(\log \frac{\mathcal{L}}{|\mathbf{r} - \mathbf{r}'|} - 1 \right) [\sin 2\phi' \hat{\mathbf{y}} - \cos 2\phi' \hat{\mathbf{x}}] , \quad (\text{A.11})$$

$$I_4 = \int dA' \frac{1}{r'} \frac{r_i - r'_i}{|\mathbf{r} - \mathbf{r}'|^2} [(y - y') \sin 2\phi' - (x - x') \cos 2\phi'] . \quad (\text{A.12})$$

The first integral can be calculated with the help of the logarithmic expansion (A.2) as well as the orthogonality condition (A.8). This yields:

$$I_3 = \frac{1}{2} \pi r \left(\frac{4}{3} - \frac{r}{R} \right) (\sin 2\phi \hat{\mathbf{y}} - \cos 2\phi \hat{\mathbf{x}}) . \quad (\text{A.13})$$

To calculate I_4 we can use again Eq. (A.4). Thus:

$$\begin{aligned} I_4 = & y \frac{\partial}{\partial r_i} \int dr' d\phi' \log |\mathbf{r} - \mathbf{r}'| \sin 2\phi' - \frac{\partial}{\partial r_i} \int dr' d\phi' \log |\mathbf{r} - \mathbf{r}'| y' \sin 2\phi' \\ & - x \frac{\partial}{\partial r_i} \int dr' d\phi' \log |\mathbf{r} - \mathbf{r}'| \cos 2\phi' + \frac{\partial}{\partial r_i} \int dr' d\phi' \log |\mathbf{r} - \mathbf{r}'| x' \cos 2\phi' . \end{aligned} \quad (\text{A.14})$$

The first and third integral in Eq. (A.14) are respectively the opposite of the y and x of I_3 . The remaining two integrals, can be calculated straightforwardly using Eq. (A.2) and (A.8). This gives:

$$\int dr' d\phi' \log |\mathbf{r} - \mathbf{r}'| f_{\pm}(r', \phi') = -\frac{\pi}{2} \left[r \left(R - \frac{2}{3}r \right) \cos \phi \pm \frac{1}{3}r^2 \left(\frac{6}{5} - \frac{r}{R} \right) \cos 3\phi \right] , \quad (\text{A.15})$$

where $f_+(r', \phi') = x' \cos 2\phi'$ and $f_-(r', \phi') = y' \sin 2\phi'$. Combining I_3 and I_4 and switching to polar coordinates finally gives Eq. (3.15b).

Chapter 4

Correlation Lengths in active nematics

This chapter is based on my co-authored article “Correlation lengths in hydrodynamic models of active nematics” published in “Soft Matter, 2016,12, 7943-7952” by Ewan J. Hemingway, Prashant Mishra, M. Cristina Marchetti and Suzanne M. Fielding. I am the co-first author of this article. I was responsible for combining the generalized model equations for two models used in the literature. I was also responsible for the results related to the Model 1 discussed in the paper.

4.1 Introduction

In spite of previous theoretical work, including the one described in the previous chapter, discrepancies still existed in the literature over the nature of the characteristic length scales that control the spontaneous proliferation and annihilation of topological defects, and the resulting dynamics in the so-called turbulent state.

In particular, the dependence of such length scales on the strength of the active forcing, $|\alpha|$, remained unclear. A recent numerical study by Giomi [78] examined the statistics of the activity-driven turbulent phase in two-dimensional nematic films by measuring the distribution of vortex sizes for a selection of activities. This work provided evidence that the key physics is determined by a single active length scale, ℓ_α , proportional to $|\alpha|^{-1/2}$. In contrast, in a closely related work, but on a different continuum model of a quasi-2D nematic, Thampi *et al.* performed a detailed study that measured several orientational and hydrodynamical correlation lengths, suggesting that the length scale of structure in the fluid instead scales as $|\alpha|^{-1/4}$.

Additionally, previous work had considered two different, but related, models of active nematic liquid-crystal hydrodynamics that are commonly used in the literature on passive liquid crystal. Our group had considered a strictly 2D liquid crystal film where the mean-field isotropic-nematic transition is continuous. The group of Yeomans and collaborators had employed a 3D model where the isotropic-nematic transition is first order and adopted it to a layer geometry by neglecting spatial variation in the direction normal to the plane of the layer. These made it impossible to systematically compare the results and reconcile previous apparently conflicting reports. To resolve these conflicts we worked with Suzanne Fielding and her student E. J. Hemingway of Durham University to compare these models using two independently developed numerical codes. By varying the key dimensionless parameters over several decades, we obtained data to support the conjecture that, in both models, the mean defect spacing in the regime of full developed active turbulence is set by the length scale $\ell_\alpha \sim (K/|\alpha|)^{1/2}$, defined by the balance of active and elastic stresses. Here $|\alpha|$ is the magnitude of the active stress (commonly referred to as the activity) and K parametrizes the free energy penalty that results from spatial variations in the director field [7, 8, 2, 54, 78, 34]. We showed that this result holds for both extensile and contractile systems, in both the flow

aligning and the flow tumbling regimes. This active length scale also controls the onset of spontaneous laminar flow in an active film, a phenomenon that has been referred to in the literature as the spontaneous flow instability [6]. Our study provides the first explicit demonstration that distinct constitutive models produce the same emergent length scale, i.e., they both produce quantitatively consistent scaling relations. We also demonstrate a regime of less highly developed turbulence in which a weaker scaling $\ell_\alpha \sim |\alpha|^{-1/4}$ appears consistent with our numerical data.

In many experimental realizations active nematics are confined to quasi two-dimensional geometries, e.g., on the surface of lipid vesicles [43], in flattened water-in-oil droplets [3], or squeezed between parallel glass plates [44]. In any numerical study, it is important to define carefully the considered dimensionality. In what follows we denote by D the number of dimensions in which the relevant fields (nematic order parameter tensor, fluid velocity, *etc.*) are allowed to vary; and separately by d the number of dimensions in which the nematic director is allowed to develop non-zero components. We shall perform two different studies. In the first we take a strictly two-dimensional model of an active nematic sheet, in which the order parameter tensor Q is allowed to develop non-zero components only in the $x - y$ directions ($d = 2$); and physical quantities are likewise allowed to vary only in the $x - y$ plane ($D = 2$). In the second study we consider a three-dimensional nematic ($d = 3$) but in which all quantities are nonetheless still assumed to be spatially homogeneous in the direction of the layer thickness ($D = 2$). In the latter case the director can in principle point out of the simulated plane, a phenomenon that can arise, e.g., in passive liquid-crystals under an applied shear-flow[79], though in practice we do not observe this in our simulations. The chapter is structured as follows. In Section 4.2 we define the equations of motion for both models, and outline the parameter ranges that we explore for each. In Section 4.3, we define the observable length scales that can be used to

characterize the fluid structure, and discuss the physical reasoning behind their definition. The results of our study are presented in Section 4.4. In Section 4.5 we provide a comparison with other works and offer our conclusions.

4.2 Models

In $D = 2$ spatial dimensions we consider an incompressible uniaxial active nematic liquid crystal with a director that can orient in d dimensions, with $d = 2, 3$ in our two respective studies. The nematic orientational order is parametrized by a symmetric and traceless tensor field $Q_{ij} = \frac{Sd}{2}(n_i n_j - \frac{\delta_{ij}}{d})$, where S is the order parameter magnitude and the director \mathbf{n} is a headless unit vector that characterizes the direction of broken orientational symmetry. The nematic is embedded in an incompressible fluid of constant density, ρ , and constant viscosity, η . The fluid velocity field is denoted by \mathbf{v} . The associated pressure field p is determined by the incompressibility condition $\nabla \cdot \mathbf{v} = 0$.

The equations of motion for an active nematic are derived from the well-known hydrodynamic equations for a passive liquid-crystal [34]

$$\rho D_t \mathbf{v} = \eta \nabla^2 \mathbf{v} - \nabla p + \nabla \cdot \Sigma^T, \quad (4.1)$$

$$D_t \mathbf{Q} = 2[\mathbf{Q} \cdot \boldsymbol{\Omega}]^A + \mathbf{M}^{(d)}(\mathbf{D}, \mathbf{Q}) + \frac{1}{\gamma} \mathbf{H}, \quad (4.2)$$

where $D_t = (\partial_t + \mathbf{v} \cdot \nabla)$ is the material derivative and γ is a rotational viscosity. Here \mathbf{D} and $\boldsymbol{\Omega}$ denote the symmetric and antisymmetric parts of the rate of strain tensor $(\nabla \mathbf{v})_{ij} \equiv \partial_i v_j$, respectively, with $D_{ij} = \frac{1}{2}(\partial_i v_j + \partial_j v_i)$ and $\Omega_{ij} = \frac{1}{2}(\partial_i v_j - \partial_j v_i)$. For other tensors the transpose, symmetric, antisymmetric and traceless parts are denoted by the superscripts \dagger , S , A and T , respectively. For example, $[\mathbf{B}]^A = \frac{1}{2}[\mathbf{B} - \mathbf{B}^\dagger]$.

The relaxation dynamics of the alignment tensor in (4.2) is governed by the molecular field, $\mathbf{H} = -[\frac{\delta F}{\delta \mathbf{Q}}]^{ST}$, in which the Landau-de Gennes free energy [34], $F = \int dV(f_b + f_d)$, is the sum of contributions from a bulk free energy density

$$f_b = G_Q \left\{ \frac{A}{2} \text{Tr} [\mathbf{Q}^2] + \frac{B}{3} \text{Tr} [\mathbf{Q}^3] + \frac{C}{4} \text{Tr} [\mathbf{Q}^2]^2 \right\} , \quad (4.3)$$

and the distortion free energy density

$$f_d = \frac{K}{2} \partial_i Q_{jk} \partial_i Q_{jk} . \quad (4.4)$$

Here G_Q and K determine the bulk and distortion energy density scales respectively. For simplicity we have adopted the one-elastic constant approximation in the distortion free energy (Eq. 4.4).

The tensor $\mathbf{M}^{(d)}(\mathbf{B}, \mathbf{Q})$ is defined for an arbitrary tensor \mathbf{B} as

$$\begin{aligned} \mathbf{M}^{(d)}(\mathbf{B}, \mathbf{Q}) = & \frac{2}{d} \xi \mathbf{B} + \xi \{ \mathbf{B} \cdot \mathbf{Q} + \mathbf{Q} \cdot \mathbf{B} - \frac{2}{d} \mathbf{I} \text{Tr} [\mathbf{Q} \cdot \mathbf{B}] \} \\ & - 2\xi \mathbf{Q} \text{Tr} [\mathbf{Q} \cdot \mathbf{B}] , \end{aligned} \quad (4.5)$$

where

$$\xi = \frac{Sd}{(d-2)S+2} \lambda . \quad (4.6)$$

Here λ is the Leslie-Ericksen flow aligning parameter, which specifies how the nematic director responds to a shear flow: $|\lambda| > 1$ corresponds to flow-aligning nematics and $|\lambda| < 1$ corresponds to the flow-tumbling regime. (See Appendix A.)

The stress tensor Σ in (4.1) is the sum of passive liquid-crystal and active contributions, $\Sigma = \Sigma^Q + \Sigma^a$. The passive part of the stress tensor is given by

$$\Sigma^Q = 2[\mathbf{Q} \cdot \mathbf{H}]^A - \mathbf{M}^{(d)}(\mathbf{H}, \mathbf{Q}) - \nabla \mathbf{Q} : \frac{\delta F}{\delta \nabla \mathbf{Q}} . \quad (4.7)$$

In an active nematic there is an additional active stress contribution that arises from the dipolar forces exerted by active particles on their environment. This active stress is $\Sigma^a = \alpha \mathbf{Q}$, where $\alpha > 0$ describes contractile stresses and $\alpha < 0$ extensile stresses. In the passive limit $\alpha \rightarrow 0$, the equations just described reduce to those of a passive liquid-crystal.

So far, the model that we have presented encompasses both of the numerical studies performed. We now outline the specific choices for parameter values and dimensionality made in each of the two numerical studies separately, and discuss how these choices affects the form of the equations.

Model I (MI): This model describes a $D = 2$ dimensional nematic sheet with a $d = 2$ dimensional nematic order parameter. In this case the symmetric second rank tensor \mathbf{Q} has only two independent components and $\text{Tr}[\mathbf{Q}^3] = 0$ identically. In Model I the mean-field free energy ((4.3)) has coefficients $A = \frac{1-\Gamma}{2}$ and $C = \Gamma$, where Γ is a dimensionless parameter that controls the continuous transition from an isotropic to a nematic state, with the transition occurring at $\Gamma = 1$. The second term in (4.5) is also identically zero; the third term is of a higher order in \mathbf{Q} and can safely be neglected [75], so that $\mathbf{M}^{(2)}(\mathbf{B}, \mathbf{Q}) = \xi \mathbf{B}$. We also exclude the last term in (4.7) in Model I. We assume a constant density $\rho = 1$ for which the Reynolds number $Re = \rho V \ell_Q / \eta = 1$, where the velocity scale is $V = \ell_Q G_Q / \eta$. We choose $\Gamma = 2$ such that the system is deep in the nematic state, with $S_0 = 0.78$. According to (4.6), the system will be in the flow-aligning regime if $|\xi| > 0.78$ and in the flow-tumbling regime for $|\xi| < 0.78$. All results shown below for Model I correspond to $\xi = \pm 0.1$ (flow-tumbling regime). We also choose $\xi > 0$ for extensile systems ($\alpha < 0$) and $\xi < 0$ for contractile systems ($\alpha > 0$) to guarantee $\alpha \xi < 0$, a condition that is required in to observe the initial flow instability in the ordered state [54].

Model II (MII): This model considers a $D = 2$ dimensional layer of nematic

parameter	description	dimensions
α	activity	$[\sigma]$
K	Frank constant	$[\sigma][L]^2$ (= 1 in MI)
G_Q	energy density scale	$[\sigma]$ (= 1 in MI, MII)
γ	rotational viscosity	$[\sigma][T]$ (= 1 in MII)
ξ	alignment param.	[1]
Γ	IN control param.	[1]
η	solvent viscosity	$[\sigma][T]$ (= 1 in MI)
ρ	solvent density	$[M][L]^{-d}$
$L_x = L_y = L$	box size	$[L]$ (= 1 in MII)

TABLE 4.1: Summary of the various model parameters and their dimensions. The choices for mass $[M]$ (or equivalently stress $[\sigma] = [M][L]^{d-2}[T]^{-2}$), length $[L]$ and time $[T]$ in each model are also indicated.

liquid crystal described by the full $d = 3$ Landau free energy given in (4.3), thereby in principle allowing the director to explore all $d = 3$ dimensions. However it still neglects all spatial variations in the direction of the layer thickness, so taking $D = 2$ as noted above. In this case the free energy in (4.3) sets $A = 1 - \frac{\Gamma}{3}$, $B = -\Gamma$ and $C = \Gamma$, yielding a first order isotropic-nematic transition at $\Gamma = 2.7$. In the following we choose $\Gamma = 3$ which places us at the spinodal stability limit of the isotropic phase and well within the nematic state, with $S_0 = 0.6$. According to (4.6), the system will be in the flow-aligning regime for $|\xi| > 0.6$ and in the flow-tumbling regime for $|\xi| < 0.6$. In all simulations using Model II we have fixed $\xi = 0.7$, corresponding to a flow-aligning system. We consider only extensile systems with this model, i.e., values of $\alpha < 0$. Finally, in MII we take the limit of zero Reynolds number by setting $\rho = 0$.

The full list of nine parameters (for both models) is given in Table 4.1. We are

free to choose units of mass $[M]$, length $[L]$ and time $[T]$, or equivalently of stress $[\sigma] = [M][L]^{d-2}[T]^{-2}$, length $[L]$ and time $[T]$, and we have noted in Table 4.1 which quantities we chose to set equal to unity in each of the two studies. This leaves six dimensionless groupings that we summarize in Table 4.2, three of which are fixed throughout. Therefore even though we choose our units differently in the two different simulation studies, all results are presented and compared in a consistent adimensional way between the two models. We choose parameters that produce flow-tumbling behaviour in Model I and flow-aligning in Model II. Note that due to differences in parameter selections, the linear instability thresholds in the two models differ by a factor $O(10^3)$ ($\alpha_c/G_Q = 0.3 \rightarrow 0.4$ in Model I [54] and $\alpha_c/G_Q = 4 \times 10^{-5} \rightarrow 4 \times 10^{-4}$ in Model II [80]). Accordingly, the onset of the turbulent regime in each model is separated by a similar factor, requiring us to explore different ranges of dimensionless activity, as noted in Table 4.2. In particular, in Model II we explore the transition from small to large activities, whereas Model I focuses on larger activities still (i.e., deeper into the regime of fully developed active turbulence).

4.2.1 Numerical details

In order to demonstrate the robustness of our results with respect to numerical implementation, we use two independent codes (one for each model). In each case we perform simulations in a square box of side L with bi-periodic boundary conditions. The \mathbf{Q} dynamics in Model I is time-integrated numerically on a square grid of 128^2 points using a fourth order Runge-Kutta method, with a timestep $\Delta t = 10^{-3}$. Gradients of \mathbf{Q} are computed using a finite difference scheme. In Model II \mathbf{Q} is integrated numerically using a Euler time-stepping scheme of timestep in the range $\Delta t = 10^{-4} \rightarrow 10^{-2}$ on a grid of $256^2 \rightarrow 2048^2$ points (dependent on the magnitude of activity) and gradients of \mathbf{Q} are treated using a semi-implicit Fourier method. In Model II, the velocities are determined instantaneously from

parameter	description	MI value	MII value
<i>varied parameters</i>			
α/G_Q	dimensionless activity	$20 \leftrightarrow 10^3$	$0.05 \leftrightarrow 12.8$
$\frac{K}{L^2 G_Q} = \left(\frac{\ell_Q}{L}\right)^2$	ratio of micro- to macroscopic length scales	6.1×10^{-5}	$2 \times 10^{-6} \leftrightarrow 10^{-5}$
γ/η	ratio of viscosities	$10 \leftrightarrow 40$	0.567
<i>fixed parameters</i>			
ξ	alignment param.	± 0.1	0.7
Γ	IN control param.	2	3
$\text{Re} = \frac{\rho \ell_Q V}{\eta}$	Reynolds number	1	0

TABLE 4.2: Summary of the dimensionless parameters and their values in both models. The velocity scale $V = \ell_Q G_Q / \eta$ in our units.

the force balance equation, which we solve in Fourier space using a stream function formulation. In Model I, we integrate the Navier-Stokes equation ((4.1)) with the same scheme used for the order parameter equation to obtain the velocity at every time step. We have verified that our results are quantitatively unchanged upon decreasing the timestep or grid spacing.

4.3 Characteristic length scales

Irrespective of the specific details of the model used, we expect the resulting dynamics of the active nematic to be controlled by the interplay of key length- and time scales that govern the basic physics.

4.3.1 Model length scales

An inspection of the hydrodynamic equations and model geometry reveals three underlying length scales. The first is simply the system size L . The second arises from balancing the bulk and elastic-distortion free energy terms in Eqs. 4.3 and 4.4, to obtain the equilibrium nematic persistence length, which deep in the nematic state is given by

$$\ell_Q = \sqrt{\frac{K}{G_Q}}. \quad (4.8)$$

This is the length scale over which spatial correlations in the nematic field decay deep in the nematic phase, where it is proportional to the defect core radius. The third lengthscale arises by balancing the elastic stress $\sim K/\ell^2$ associated with a deformation over a length ℓ with the active stress scale $\sim |\alpha|$, to give the active length scale

$$\ell_\alpha = \sqrt{\frac{K}{|\alpha|}}. \quad (4.9)$$

To guarantee that any physics on these length scales ℓ_Q, ℓ_α is not contaminated by finite size effects, we focus on the regime in which $\ell_Q \ll L$ and $\ell_\alpha \ll L$.

Alternatively, from a dynamical viewpoint one might consider the system to be controlled by two timescales: the passive structural relaxation time $\tau_p = \gamma\ell^2/K$, which controls the relaxation of a distortion to the nematic order on a length scale ℓ , and the active time scale $\tau_\alpha = \eta/|\alpha|$, which controls the relative rates of injection of active stresses and stress decay via viscous dissipation. The length scale that results when these timescales are equated is then

$$\ell_\tau = \sqrt{\frac{K\eta}{\alpha\gamma}} = \ell_\alpha \sqrt{\frac{\eta}{\gamma}}. \quad (4.10)$$

4.3.2 Emergent length scales

The length scales discussed above were motivated by simple dimensional analysis of the model parameters and flow geometry. In our numerical simulations, we find that (for a high enough level of activity) an initially homogeneous state gives way to a spatio-temporally complicated state with defects in the nematic director field, and associated local flows in the velocity field, as found earlier by several authors [49, 18] and shown in the snapshots of Figs. 4.2 and 4.3. An important aim of the present work is to elucidate how the length scales associated with these emergent structures depend on the underlying model length scales just discussed. We denote these emergent length scales by the common symbol ℓ^* , but in fact there are multiple possible scales that we might choose to characterize the spatio-temporal dynamics, as we now describe.

- **Mean defect separation ℓ_d :** We define the mean defect separation

$$\ell_d = 1/\sqrt{n_d}, \quad (4.11)$$

where n_d is the areal density of defects, calculated by adapting the defect tracking method of Ref. [81].

- **Director correlation length ℓ_θ :** The normalised director correlation function defined as

$$C_\theta(R) = \frac{2\langle \mathbf{n}(\mathbf{R}) \cdot \mathbf{n}(\mathbf{0}) \rangle - 1}{2\langle \mathbf{n}(\mathbf{0}) \cdot \mathbf{n}(\mathbf{0}) \rangle - 1}. \quad (4.12)$$

This characterizes the probability that two director orientations a distance R apart are the same (respecting the fact that $\mathbf{n} \rightarrow -\mathbf{n}$ are equivalent for a nematic). Here and throughout, the angular brackets $\langle \cdot \rangle$ indicate an average over space and time. We then choose ℓ_θ to be the length at which $C_\theta(\ell_\theta) = \frac{1}{2}$, as in Fig. 4.1 (inset).

- **Velocity correlation length ℓ_v :** Analogously, the velocity correlation function,

$$C_v(R) = \frac{\langle \mathbf{v}(\mathbf{R}) \cdot \mathbf{v}(\mathbf{0}) \rangle}{\langle \mathbf{v}(\mathbf{0}) \cdot \mathbf{v}(\mathbf{0}) \rangle}, \quad (4.13)$$

defines the velocity correlation length ℓ_v according to $C_v(\ell_v) = \frac{1}{2}$.

- **Vorticity correlation length ℓ_ω :** Finally, we define the correlation function for the local vorticity, $\Omega = \partial_x v_y - \partial_y v_x$, as

$$C_\Omega(R) = \frac{\langle \Omega(\mathbf{R})\Omega(\mathbf{0}) \rangle}{\langle \Omega(\mathbf{0})\Omega(\mathbf{0}) \rangle}, \quad (4.14)$$

and define the vorticity correlation length ℓ_ω by $C_\Omega(\ell_\omega) = \frac{1}{2}$.

4.3.3 Scaling hypothesis

Simple dimensional analysis based on the model length scales discussed in Sec. 4.3.1 suggests that the length scales ℓ^* of Sec. 4.3.2 characterizing the emergent structures in the fluid (whether $\ell_d, \ell_\theta, \ell_v$ or ℓ_ω) should obey a simple scaling relation of the form

$$\frac{\ell^*}{\ell_Q} = F^* \left(\frac{\ell_\alpha}{\ell_Q}, \frac{L}{\ell_Q} \right), \quad (4.15)$$

where F^* is a general scaling function.

Previous simulation studies [7, 14, 80, 78, 19] have shown that all characteristic length scales, denoted generically by ℓ^* , decrease with increasing activity $|\alpha|$. At low activity, typically just a few defects are seen in the simulation box, as in the snapshots in Figs. 4.2c and 4.3b. At higher activity one obtains a state of fully developed turbulence with a much higher density of defects (Figs. 4.2d and 4.3c). In this highly turbulent regime we expect the emergent length scale ℓ^* to become much smaller than, and therefore independent of, the system size L . The above

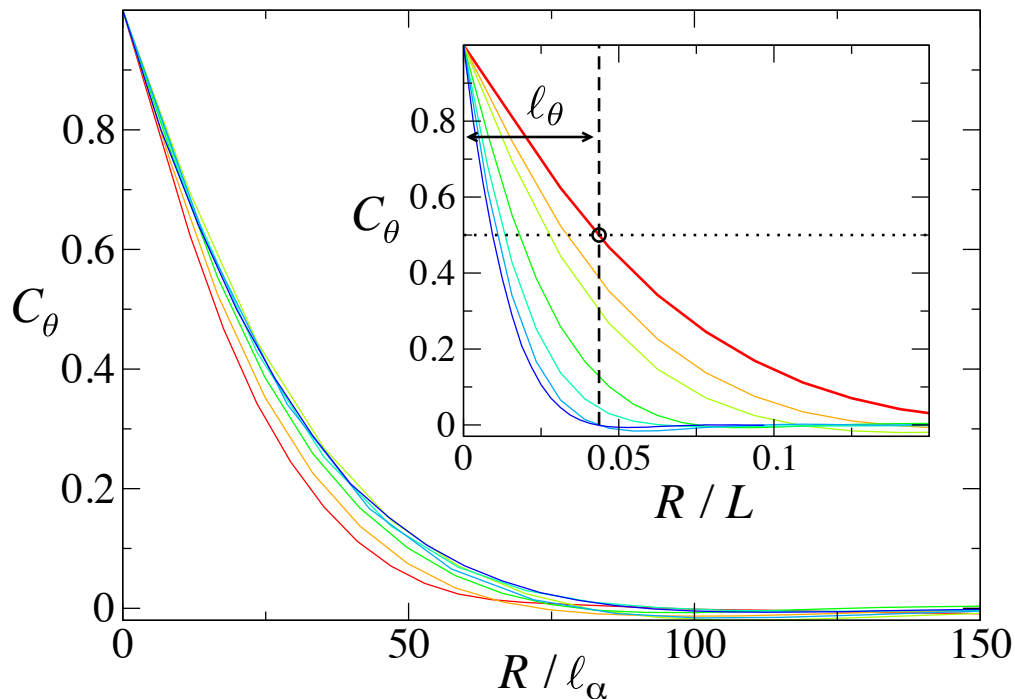


FIGURE 4.1: Nematic correlation function C_θ defined in (4.12) obtained from Model II for an extensile system in the regime of spatio-temporally chaotic behavior for $(\ell_Q/L)^2 = 5 \times 10^{-6}$ and activities in the range $\alpha/G_Q = -0.4$ (red) to -12.8 (blue). Inset: Unscaled data, demonstrating our definition $C_\theta(\ell_\theta) = \frac{1}{2}$. Main: the same data collapse onto a single curve when rescaled by the active length ℓ_α .

scaling form is then accordingly expected to reduce to

$$\frac{\ell^*}{\ell_Q} = F^* \left(\frac{\ell_\alpha}{\ell_Q} \right). \quad (4.16)$$

In our simulations all scaling law measurements are taken safely within this regime of fully developed turbulence, such that the emergent length scales are free of finite size effects. We also explicitly demonstrate that finite-size effects indeed return when ℓ_α/L is no longer small, as illustrated by the snapshot of Fig. 4.2c.

It is also worth noting that at extremely large activities the defect density could in principle become so large that the defect spacing approaches the microscopic length

scale ℓ_Q . In this regime we would expect ℓ^* to be unable to decrease further upon any additional increase in activity, and so to saturate. However our simulations do not reach this limit and the inequality $\ell_Q < \ell^* < L$ is always respected.

4.3.4 Form of the scaling function

Having proposed the existence of a scaling function in Eqn. 4.16, we now consider possible specific forms for this functional dependence of ℓ^* on the model parameters. Conflicting scaling laws for ℓ^* have been proposed in the existing literature [19, 82, 78]. While all of these studies agree that $\ell^* \propto K^{1/2} \propto \ell_Q$, there remains an apparent discrepancy over the scaling of ℓ^* with the activity.

Using Model II, Thampi *et al.* [19, 82] have proposed that $\ell^* \propto \alpha^{-1/4}$, which would correspond to F^* in Eqn. 4.16 having a square root dependence on its first argument. In contrast, using Model I Giomi [78] have suggested the relation $\ell^* \propto \alpha^{-1/2}$, which would correspond to a linear dependence of F^* on its first argument. A possible origin of this discrepancy is the differing dimensionality of the order parameter \mathbf{Q} between the two studies: while both have $D = 2$, Refs. [19, 82] had $d = 3$, whereas Ref. [78] had $d = 2$. This motivates us to compare numerical results for both $d = 2, 3$ within a single study. However our results below will rule out differences in d as a source of discrepancy. Another potential reason could be that the two studies in fact explored different parameter regimes given the high dimensionality of the parameter space in these models. Therefore in order to ascertain the generality of these scaling laws, we systematically explore wide ranges for the three relevant adimensional parameters $(\alpha/G_Q, \ell_Q/L, \gamma/\eta)$ for both models. Our results will show that both forms suggested by the earlier studies can indeed apply, each in a different regime: one in the regime of fully developed active turbulence, the other when the system size plays a non-trivial role.

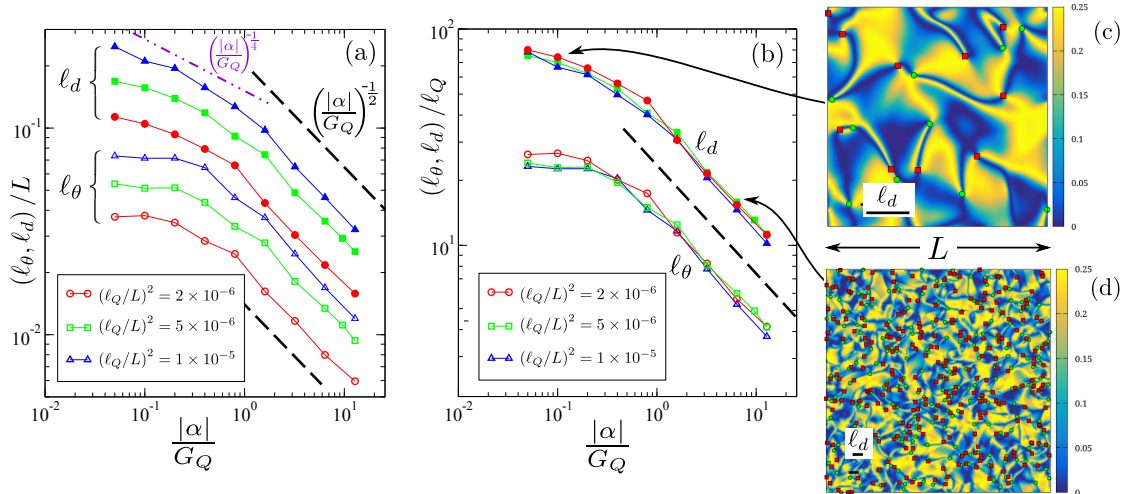


FIGURE 4.2: Results from Model II for the nematic correlation length ℓ_θ (empty symbols) and defect spacing ℓ_d (filled symbols) as functions of the dimensionless activity $|\alpha|/G_Q$ for an extensile nematic ($\alpha < 0$). (a) Lengthscales vs $|\alpha|$ for various values of the microscopic correlation length: $(\ell_Q/L)^2 = 2 \times 10^{-6}$ (red circles), 5×10^{-6} (green squares), and 1×10^{-5} (blue triangles). The remaining parameter values are given in Table 4.2. At small activity we see saturation due to finite size effects. (b) The curves collapse when ℓ_θ and ℓ_d are rescaled by ℓ_Q . In both frames the black dashed lines show $(|\alpha|/G_Q)^{-1/2}$. In Fig. 4.2a we also mark the power law $(|\alpha|/G_Q)^{-1/4}$ obtained by Thampi *et al.* as a purple dot-dashed line. (c,d) Representative snapshots of $(n_x n_y)^2$ for (c) $|\alpha|/G_Q = 0.1$ and (d) $|\alpha|/G_Q = 6.4$. We set $(\ell_Q/L)^2 = 1 \times 10^{-5}$ in both snapshots. Defects of topological charge $\pm 1/2$ are identified by green dots (+) and red squares (-).

For videos see supplementary material.

4.4 Results

We now present the results of our simulations. We focus on the regime of fully developed turbulence, corresponding to activity large enough to avoid finite system-size effects ($\ell_\alpha < L$) and yet small enough to avoid saturation of the defect spacing at the microscopic length ($\ell_d > \ell_Q$). We systematically explore the functional dependence of the emergent correlation lengths defined in Section 4.3.2 on the model parameters. Specifically in Model I we vary the activity, α/G_Q , and viscosity ratio, γ/η , keeping all other parameters fixed to the values in Table 4.2. In Model II we vary the activity α/G_Q and the nematic persistence length ℓ_Q/L , with all other parameters fixed to the values in Table 4.2. We will show that in the region of fully developed active turbulence all of the emergent length scales defined

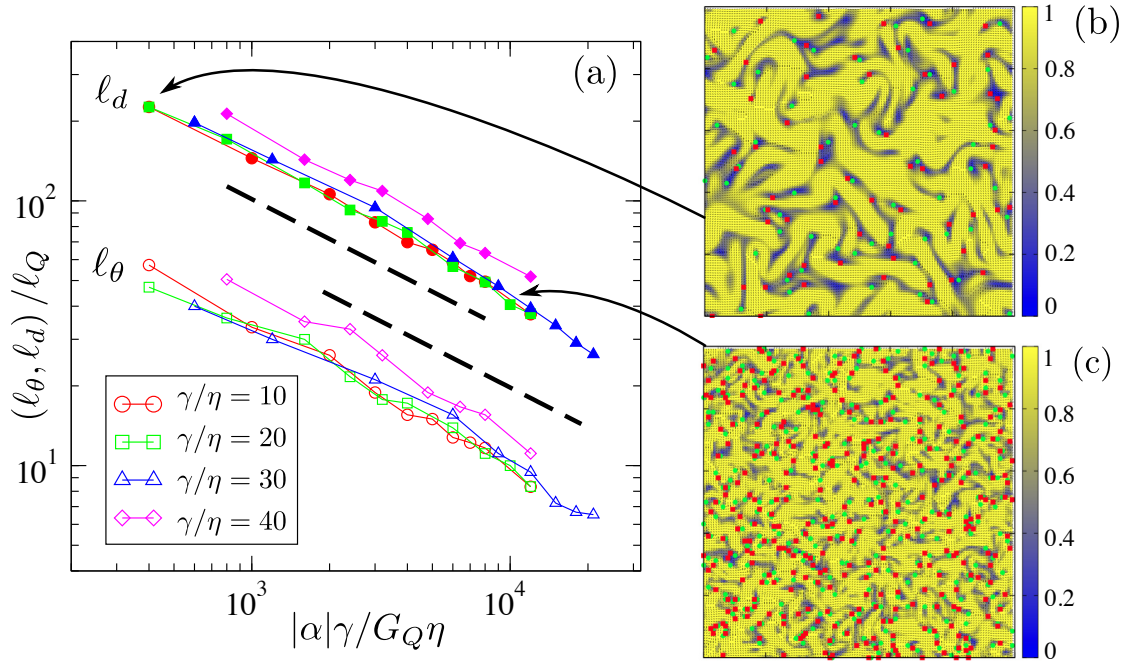


FIGURE 4.3: Results from Model I for the nematic correlation length ℓ_θ (empty symbols) and defect spacing ℓ_d (filled symbols) as functions of the dimensionless activity $|\alpha|\gamma/G_Q\eta$ for an extensile nematic ($\alpha < 0$). (a) Length scales vs $|\alpha|$ for various values of the viscosity ratio: $\gamma/\eta = 10$ (red circles), 20 (green squares), 30 (blue triangles), and 40 (magenta diamonds). The values of the other parameters are given in Table 4.2. The black dashed lines denote a slope of $-1/2$. (b,c) Representative snapshots of the alignment tensor for $\eta/\gamma = 20$ in (b) the low activity regime ($|\alpha|/G_Q = 20$) with low defect density and (c) the high activity regime ($|\alpha|/G_Q = 100$) with high defect density. The color scale represents the magnitude S of the order parameter and the black lines denote the local orientation of the director field. Topological defects with charge $\pm 1/2$ are shown as green dots (+) and red squares (-).

above scale with the active length $\ell_\alpha \sim |\alpha|^{-1/2}$, in both models. We will additionally demonstrate that a weaker exponent might be obtained in the regime of less well developed turbulence, where the typical size of the emergent structures is an appreciable fraction of the box size.

4.4.1 Correlation lengths

In this section, we present our results for the correlation lengths defined in Sec. 4.3.2. Our main focus will be on an extensile nematic, corresponding to $\alpha < 0$. We shall briefly discuss the contractile case at the end of this section.

4.4.1.1 Extensile active matter

Orientalional correlations. We begin by considering correlations in the nematic order parameter \mathbf{Q} . Figs. 4.2a and 4.3a shows the director correlation length ℓ_θ and the defect spacing ℓ_d as obtained from Model II and Model I, respectively. For sufficiently large activity α , we find that in both models both lengths obey a clear scaling law $\ell_d, \ell_\theta \sim (\alpha/G_Q)^{-1/2}$ (black dashed lines). Note that the defect spacing correlation length ℓ_d is consistently larger than ℓ_θ by a factor $\sim 2 - 3$. This is to be expected as correlations at the halfway point between two defects ($\ell_d/2$) should be similar to those at ℓ_θ .

At smaller activities (i.e., for $|\alpha|/G_Q \lesssim 1$) the data obtained with Model II show a saturation in the power law (leftmost data points in Fig. 4.2a). This can be attributed to that fact that the length scale of nematic structure now spans an appreciable fraction of the system size, as seen in the snapshots of Fig. 4.2c. It is possible that fitting a power law in this saturation regime could result in a less negative exponent than the $-1/2$ found in the regime of fully developed turbulence. Indeed we find that the scaling $|\alpha|^{-1/4}$ suggested by Thampi *et al.* (purple dashed dotted line in Fig. 4.2a) matches our data reasonably well in this regime.

The data in Fig. 4.2a also suggests that both ℓ_d and ℓ_θ scale linearly with ℓ_Q . We verify this scaling explicitly in Fig. 4.2b by plotting ℓ_d/ℓ_Q and ℓ_θ/ℓ_Q against activity. The data for various values of ℓ_Q collapse neatly onto a single curve, demonstrating a clear linear relation between both correlation lengths and ℓ_Q .

The data obtained with Model I shown in Fig. 4.3a focus on large activities and verify that in this regime the scaling of both ℓ_d and ℓ_θ with $(|\alpha|/G_Q)^{-1/2}$ holds regardless of the model used. (They do not probe the saturation with system size seen at lower activities in Model II.) Data obtained for different values of the viscosity ratio γ/η can be collapsed when plotted as shown in Fig. 4.3b, suggesting

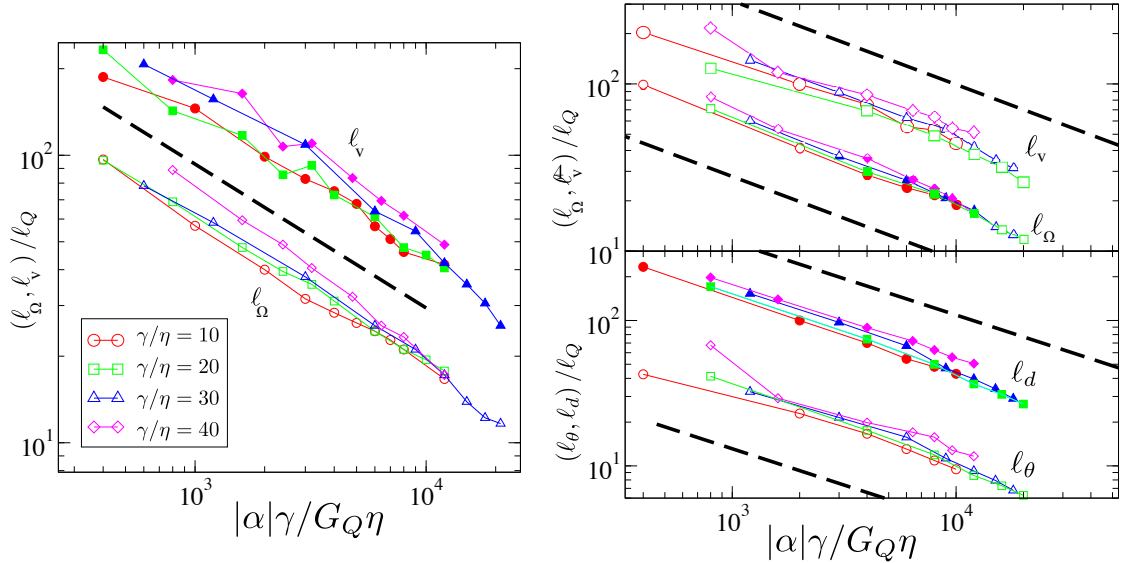


FIGURE 4.4: Velocity (l_v , filled symbols) and vorticity (l_Ω , empty symbols) correlation lengths, normalized by l_Q for (a) an extensile ($\alpha < 0$) and (b) a contractile ($\alpha > 0$) system. We explore several values of the viscosity ratio: $\gamma/\eta = 10$ (red circles), 20 (green squares), 30 (blue triangles), and 40 (magenta diamonds). Frame (c) shows the defect spacing l_d (filled symbols) and the director correlation length l_θ (empty symbols) for a contractile ($\alpha > 0$) active nematic as a function of $\alpha\gamma/G_Q\eta$ for the same set of values of γ/η . All lengths scale as $(\alpha\gamma/G_Q\eta)^{-1/2}$. The black dashed lines represent a slope of $-1/2$.

$l^*/l_Q \sim l_\tau/l_Q = [|\alpha|\gamma/(G_Q\eta)]^{-1/2}$, although the range of variation of the viscosity ratio is not sufficient to provide convincing evidence of scaling.

Taken together, the data obtained with the two models tests the functional dependence of the two nematic correlation lengths with respect to activity and the nematic persistence length l_Q . Once free of the system size, we find that both obey $l^*/l_Q \sim l_\alpha/l_Q$. Consistent with this scaling, replotting in Fig. 4.1 (main) the full director correlation function as a function of the rescaled coordinate R/l_α gives good data collapse. Additionally, the data obtained with Model I suggest a scaling $l^*/l_Q \sim (l_\alpha/l_Q)\sqrt{\gamma/\eta}$, but a larger range of γ values would be needed to verify this. Next we demonstrate that the same scaling form is observed for correlations lengths associated with the velocity field \mathbf{v} .

Velocity and vorticity correlation lengths. Using data obtained with Model I, we

explore the dependence of the velocity correlation length ℓ_v and the vorticity correlation length ℓ_ω (as defined in Section 4.3.2) on activity. In light of the results of the previous section, we directly plot both these lengths against the rescaled activity $|\alpha|\gamma/G_Q\eta$ (see Fig. 4.4a). As shown previously for the orientation correlation lengths, we again observe that both ℓ_v and ℓ_ω scale as $\sim (|\alpha|\gamma/G_Q\eta)^{-1/2}$, with all data sets falling approximately on a single curve. We stress that this behavior is different from that reported in Ref. [19], where it was argued that ℓ_v does not depend on activity, while ℓ_ω scale as $\alpha^{-1/4}$.

4.4.1.2 Contractile active matter.

So far we have presented data for extensile systems, corresponding to $\alpha < 0$. However many examples of contractile active matter are found in nature, e.g., suspensions of *Chlamydomonas* algae [83], or cytoskeletal actomyosin networks [84]. Therefore in order to further demonstrate the generality of our results, we now briefly consider the contractile case ($\alpha > 0$). Since the linear instability of the homogeneous state requires $\alpha\xi < 0$ [54], for contractile systems we use $\xi \rightarrow -\xi = -0.1$. Our data, shown in Figs. 4.4(b,c), support the idea that the defect spacing (ℓ_d), director correlation length (ℓ_θ), velocity (ℓ_v) and vorticity (ℓ_ω) correlation lengths are all controlled by a single active length scale $\ell_\alpha \sim |\alpha|^{-1/2}$.

4.4.2 Kinetic energy and enstrophy

The above scaling relations were obtained using the correlation functions defined in Section 4.3, which are normalised so that each function, e.g., $C_v(R)$, approaches unity as the separation distance $R \rightarrow 0$. (See Fig. 4.1.) The normalization constants themselves, however, (i.e., the denominators in Eqs. 4.13 and 4.14) also provide useful information as they are directly proportional to the mean kinetic

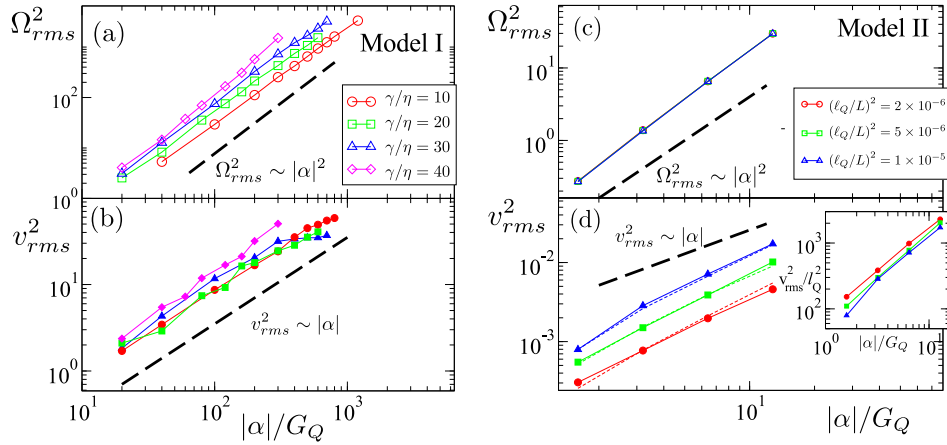


FIGURE 4.5: Scaling of kinetic energy (frames (a) and (c)) and enstrophy (frames (b) and (d)) with activity for both Models I and II. The left figure displays the results obtained from Model I by varying the viscosity ratio γ/η as shown. The right figure displays the results obtained from Model II by varying the nematic correlation length ℓ_Q/L . The inset of frame (d) shows the scaling collapse of the kinetic energy when plotting v_{rms}^2/ℓ_Q^2 against activity. In frame (d), data is shown for two numerical resolutions: dashed lines for $N = 1024$, and solid lines for $N = 2048$.

energy and enstrophy of the system, given by

$$E_k = \frac{1}{2} v_{rms}^2 = \frac{1}{2} \langle \mathbf{v}(\mathbf{r}) \cdot \mathbf{v}(\mathbf{r}) \rangle, \quad (4.17)$$

$$E_s = \frac{1}{2} \Omega_{rms}^2 = \frac{1}{2} \langle \Omega(\mathbf{r}) \Omega(\mathbf{r}) \rangle, \quad (4.18)$$

where the angular brackets $\langle \cdot \rangle$ again denote an average over space and time. These quantities can be obtained experimentally, for instance by using particle image velocity (PIV) to quantify the flow fields of active liquids, as done by Dunkel *et al.* [85] in suspensions of extensile *B. subtilis* bacteria. We now use our earlier findings to motivate the expected scaling relation of these flow properties with activity, and then verify our predictions with further numerical data from both models.

Using simple dimensional analysis, the characteristic velocity of activity-induced shear flows associated with distortion of the local nematic order over a length scale

ℓ^* can be obtained from the force balance condition ((4.1)) as

$$v \sim |\alpha| \ell^* / \eta. \quad (4.19)$$

Our results indicate that for sufficiently large values of activity the physics is controlled by a single active length scale ℓ^* , with $\ell^* \sim |\alpha|^{-1/2}$. Using this in (4.19), we find $v \sim |\alpha|^{1/2}$ and $\langle v_{rms}^2 \rangle \sim |\alpha|$. The scaling of the vorticity can be estimated as $\omega \sim v/\ell^*$, which gives an enstrophy $\Omega_{rms}^2 \sim |\alpha|^2$.

This scaling is consistent with the findings of Ref. [78] in which the author examined the typical size of vortex structures in the regime of spatio-temporal chaotic dynamics using what we refer to here as Model I and found that both the vortex size and the defect spacing appear to scale with the active lengthscale ℓ_α . Further evidence for this scaling can be found in the experiments of Ref. [85], which found that $\Omega_{rms}^2 = v_{rms}^2 / (\ell^*)^2$ where ℓ^* is the characteristic vortex size: assuming that $\ell^* \sim \ell_\alpha$, this implies that $\Omega_{rms}^2 \sim |\alpha| v_{rms}^2$ as we have argued above. Our proposed scaling is not, however, in agreement with the findings of Ref. [18, 82]. In those studies it was found that $v_{rms}^2 \sim |\alpha|^2$ and $\Omega_{rms}^2 \sim |\alpha|^2$, a result that cannot seemingly be reconciled with the simple assumption that $\Omega \sim v/\ell_\alpha$.

In order to appraise these conflicting scaling laws, we perform simulations with both Model I and Model II and measure the kinetic energy (v_{rms}^2 , see Figs. 4.5a, b) and enstrophy (Ω_{rms}^2 , Figs. 4.5c, d). The data from both models clearly obey our expected scaling laws $v_{rms}^2 \sim |\alpha|$ and $\Omega_{rms}^2 \sim |\alpha|^2$ (black dashed lines). With Model I our choice of units means that increasing the rotational viscosity γ is equivalent to reducing the solvent viscosity η . Our dimensional analysis in (4.19) suggests that increasing γ/η should increase the characteristic velocity. We indeed observe this trend in our data in Figs. 4.4b, although simulations over a larger range of γ/η would be required to determine the exact scaling. By the same analysis, we also expect that v_{rms}^2 should be proportional to ℓ_Q^2 for fixed G_Q , since

$v_{rms}^2 \sim (\alpha \ell^*/\eta)^2 \sim (|\alpha|G_Q/\eta^2)\ell_Q^2$. Our data from Model II explores several values of ℓ_Q , and plotting v_{rms}^2/ℓ_Q^2 against activity indeed leads to a reasonable curve collapse (Fig. 4.4d inset). Consistent with the findings of Giomi[78], we observe no appreciable dependence of Ω_{rms}^2 on ℓ_Q . This follows again from the scaling, $\Omega_{rms}^2 \sim v_{rms}^2/\ell^{*2} \sim (\alpha/\eta)^2$.

4.5 Discussion

Using two distinct continuum models that have been studied extensively within the literature, we have performed a detailed numerical study of an active nematic to examine the scaling with activity of a number of structural and hydrodynamic correlation lengths, including the mean defect spacing. Our findings are consistent with the suggestion first put forward in Ref. [78] that in the regime of fully developed active turbulence defect proliferation, and the associated turbulent-like dynamics of the active nematic, are controlled by a single length scale $\ell_\alpha \sim |\alpha|^{-1/2}$. This is also the length scale that controls the onset of spontaneous flow instability of active films [6, 7, 40]. Our numerical data from both models show that all measures of correlation length considered scale with this length scale, for both extensile and contractile systems.

Two caveats must, however, be applied. First, for extremely large activities (i.e., $\ell_\alpha \sim \ell_Q$) activity-induced deformations below the nematic persistence length ℓ_Q are expected to be suppressed. Secondly, at low activities, structures can form that span the system size, and correlation lengths will correspondingly saturate, (i.e., $\ell_\alpha \sim O(L)$). We have explicitly demonstrated this system-size saturation in our simulations, a result that reconciles the apparently conflicting power-law exponents previously reported in the literature.

Finally, to further support our findings, we have calculated the average kinetic energy and average enstrophy of the system, quantities that are readily obtainable from experiment. Our numerical results show that the scaling of these quantities with activity is consistent with a simple dimensional analysis based on the assumption that the physics is controlled by the single length scale ℓ_α .

Our results show that the key scaling relations hold for both strictly 2D and quasi-2D models. Encouragingly, this implies that such models capture the dynamics of active nematics in a generic way, i.e., independent of the specifics of the model. How our results would compare with the equivalent fully-3D simulation of an active nematic remains an interesting open question.

4.6 Acknowledgment

We thank Mark Bowick for introducing us to Ref. [81] (that describes a method for defect tracking) and Luca Giomi for writing the code used to study Model I. We thank them both and Mike Cates for invaluable discussions. MCM and PM were supported by the National Science Foundation through award DMR-1305184 and by the Syracuse Soft Matter Program. EJH thanks EPSRC for a Studentship. SMF's and EJH's research leading to these results has received funding from the European Research Council under the European Union's Seventh Framework Programme (FP7/2007-2013) / ERC grant agreement number 279365. The authors thank the KITP at the University of California, Santa Barbara, where they were supported through National Science Foundation Grant No. NSF PHY11-25925.

Appendix B

B.1 Flow-aligning Parameter

We include here a comparison between the tumbling parameter ξ used here and the Leslie-Erickson (LE) tumbling parameter λ (where $|\lambda| > 1$ corresponds to flow-aligning regime and $|\lambda| < 1$ corresponds to flow-tumbling regime). This comparison is presented in Appendix B of Ref. [7] for the case $d = 3$, but to our knowledge has not been displayed before for the case $d = 2$.

In d dimensions the nematic tensor \mathbf{Q}_{ij} of a uniaxial nematic can be written as

$$Q_{ij} = \frac{d}{(I/\Delta I)} S(n_i n_j - \frac{1}{d} \delta_{ij}), \quad (\text{B.1})$$

where I and ΔI are the sum and difference, respectively of the two principal values of the moment of inertia tensor of uniaxial nematogens. In our case we use $I/\Delta I = 2$ that corresponds to needle-like molecules[86].

We write the dynamical equation for the alignment tensor in d dimension using the notation of Olmsted[75],

$$\begin{aligned} \frac{DQ_{ij}}{Dt} &= \Omega_{ik}Q_{kj} - Q_{ik}\Omega_{kj} + \beta_1 D_{ij} + \frac{1}{\beta_2} H_{ij} \\ &+ \beta_5 \{ Q_{ik}D_{kj} + D_{ik}Q_{kj} - \frac{2}{d} \delta_{ij} \mathbf{D} : \mathbf{Q} \} \\ &+ \beta_6 \{ Q_{ik}H_{kj} + H_{ik}Q_{kj} - \frac{2}{d} \delta_{ij} \mathbf{H} : \mathbf{Q} \}, \end{aligned} \quad (\text{B.2})$$

where $\beta_1, \beta_2, \beta_5$ and β_6 are parameters that couple order and flow.

Substituting the expression given in (B.1) for the alignment tensor into the dynamical equation (B.2), and assuming S to be constant, we obtain an equation for the director,

$$\begin{aligned} \dot{n}_i &= (\boldsymbol{\Omega} \times \hat{\mathbf{n}})_i + \left[\frac{(I/\Delta I)^2}{2\beta_2(dS)^2} + \frac{(1 - \frac{2}{d})(I/\Delta I)\beta_6}{2dS} \right] h_i \\ &+ \left[\frac{(I/\Delta I)\beta_1}{dS} + \left(1 - \frac{2}{d} \right) \beta_5 \right] n_j D_{ij}. \end{aligned} \quad (\text{B.3})$$

Comparing (B.3) to the Leslie-Erickson equation [75],

$$\dot{n}_i = (\boldsymbol{\Omega} \times \hat{\mathbf{n}})_i + \frac{1}{\gamma_1} h_i + \lambda n_j D_{ij}, \quad (\text{B.4})$$

we identify the correspondence between the Olmsted coefficients β_i and the Leslie-Erickson coefficients as

$$S\lambda = \frac{(I/\Delta I)}{d} \beta_1 + \frac{(d-2)}{d} \beta_5 S + O(S^2), \quad (\text{B.5})$$

$$\frac{S^2}{\gamma_1} = \frac{(I/\Delta I)^2}{2\beta_2 d^2} + \frac{(1 - \frac{2}{d})(I/\Delta I)}{2d} \beta_6 S + O(S^2). \quad (\text{B.6})$$

Using $I/\Delta I = 2$ in (B.5), we obtain

$$\lambda = \frac{2}{d} \frac{\beta_1}{S} + \frac{(d-2)}{d} \beta_5. \quad (\text{B.7})$$

Finally, for the case $\beta_1 = \beta_5 = \xi$, we find

$$\xi = \begin{cases} \lambda S & \text{for } d = 2 \\ \frac{3S}{S+2}\lambda & \text{for } d = 3 \end{cases} \quad (\text{B.8})$$

The $d = 3$ case was previously reported in Ref. [7].

Chapter 5

Active Nematics on a Substrate

This chapter is based on the article “Negative stiffness and modulated states in active nematics” published in “Soft Matter, 2016,12, 8214-8225” by Pragya Srivastava, Prashant Mishra and M. Cristina Marchetti. My contribution to this article was equal to the first author’s. I was responsible for working through the linear stability analysis and the numerical analysis of the model used in the paper. I also numerically compared our results with previously published work.

5.1 Introduction

Confinement has profound effects on active fluids. It damps the flow [87, 88] and it suppresses the generic instability of unbound systems described in Chapter 3 resulting in a finite activity threshold for the onset of spontaneously flowing

states [6, 89]. Frictional damping due to confinement plays a key role in experimental realizations of active systems. In bacterial suspensions channel confinement was shown to stabilize vortex structures, leading to a state with a steady unidirectional circulation [90].

In confined nematics the energy input from active stresses is dissipated both via viscous flows that mediate hydrodynamic interactions between the active units and via friction with a substrate. Systems where viscous dissipation dominates so that frictional damping is negligible and momentum is conserved are referred to as ‘wet’, while those where dissipation is mainly controlled by friction are referred to as ‘dry’. Previous work has examined both wet [49, 18, 82, 19] and dry [91, 41, 92, 20, 93] systems, as well as the crossover between the two [94], revealing a rich dynamics driven by orientational instabilities and by the unbinding and proliferation of topological defects. A detailed summary of recent work most closely related to ours is given in Section 5.5. A remarkable phenomenon reported by several authors is the orientational ordering of the axes of the comet-like $+1/2$ disclinations. In experiments in suspensions of microtubule bundles the $+1/2$ defects were observed to organize in nematically ordered states [4]. Numerical studies of dry systems have reported both nematic [92] and polar [4, 91] order of the defect orientations and a remarkable defect-ordered state accompanied by a flow-vortex lattice at the crossover between wet and dry regimes [94]. This range of results indicates that more work is needed to understand what controls the nature of defect ordering in these systems.

Finally, the dynamics of dry polar [17] and nematic [92] active fluids has also been studied via minimal models where pattern formation is driven by diffusive currents in the order parameter equations, with the assumption of a negative order parameter stiffness, which provides an appealing and simple explanation for the instability mechanisms. Recently, it has been shown that in systems with polar symmetry

such a negative stiffness can arise from competing aligning and antialigning interactions [95] or from the interplay of polar alignment and intermediate range hydrodynamic interactions [96].

In this chapter, we consider a dry active nematic fluid, where the energy input from active stresses is balanced solely by frictional damping. By eliminating the flow velocity in favor of active stresses we obtain a single equation for the nematic order parameter, with elastic constant renormalized by activity. We show that activity can drive such elastic constants to negative values, providing a mechanism for pattern formation capable of describing in a unified manner all the spatio-temporal structures obtained in previous models. A linear stability analysis of the homogeneous isotropic and ordered states highlights the analogy with the onset of modulated states at a Lifshitz point in equilibrium systems and identifies the length scales that control stable patterns. We construct a linear stability phase diagram (Fig. 5.1) and show that all linear stability boundaries meet at a single point that plays the role of a nonequilibrium multicritical point. The linear analysis is supported by numerical integration of the nonlinear equations that yield a succession of spatially and temporally inhomogeneous structures of growing complexity with increasing activity.

In Section 5.2 we introduce the hydrodynamic model of a dry active nematic and show that it can be reduced to a single equation for the nematic order parameter tensor by eliminating the flow. We then discuss the linear stability phase diagram in Section 5.3, and present the results of the numerical integration of the non-linear equations in Section 5.4. We conclude with a comparison with previous work and a brief discussion.

5.2 Active Nematics on a Substrate

We consider a thin layer of active nematic liquid crystal on a substrate providing frictional damping. This geometry is motivated by experiments on suspensions of microtubule bundles at an oil water interface [3, 4], although it does not incorporate the full hydrodynamics of the system as described for instance in Ref. [21]. We focus on high density of active units and consider an effective one-component fluid description, as done in much of the previous literature [97, 14]. We assume a constant density, but do not enforce incompressibility, i.e., $\nabla \cdot \mathbf{v} \neq 0$. This can be realized in systems where density conservation is broken, for instance, by birth/death processes or because active units can enter or leave the nematic layer through the surrounding bulk fluid. The long-wavelength dynamics is then formulated in terms of the nematic tensor order parameter \mathbf{Q} , of components $Q_{ij} = S \left(n_i n_j - \frac{\delta_{ij}}{2} \right)$ with \mathbf{n} the director field, and the flow velocity, \mathbf{v} . The absence of the incompressibility constraint allows us to directly eliminate the flow to obtain a minimal model in terms of \mathbf{Q} dynamics only. We have also verified that imposing incompressibility only changes the location of the linear stability boundaries between the various regimes, but leaves the results qualitatively unchanged (see Appendix B).

The dynamics is then governed by an equation for the alignment tensor, coupled to the Stokes equation describing local force balance,

$$(\partial_t + \mathbf{v} \cdot \nabla) \mathbf{Q} = \mathbf{S}(\mathbf{Q}, \mathbf{A}) + \frac{1}{\gamma} \mathbf{H}, \quad (5.1)$$

$$\Gamma \mathbf{v} = \eta \nabla^2 \mathbf{v} + \alpha \nabla \cdot \mathbf{Q}. \quad (5.2)$$

The first term on the right hand side of Eq. (5.1) is a symmetric traceless tensor that describes the coupling of orientation and flow. In two dimensions it is given

by

$$\mathbf{S} = \lambda \left(\mathbf{D} - \frac{1}{2} \text{Tr} \mathbf{D} \right) + \mathbf{Q} \cdot \boldsymbol{\omega} - \boldsymbol{\omega} \cdot \mathbf{Q} - \lambda \mathbf{Q} \text{Tr}[\mathbf{Q} \cdot \mathbf{D}], \quad (5.3)$$

where \mathbf{D} and $\boldsymbol{\omega}$ are the symmetric and antisymmetric strain rate tensors, $D_{ij} = (A_{ij} + A_{ji})/2$ and $\omega_{ij} = (A_{ij} - A_{ji})/2$, with $A_{ij} = \partial_i v_j$ and λ the nematic flow alignment parameter. It should be noted that the presence of a substrate breaks Galilean invariance. As a result, the coefficients of the convective term on the left hand side of Eq. (5.1) and of the coupling of orientation to vorticity in Eq. (5.3) are not required to be unity. In addition, activity will modify the value of all parameters coupling orientation and flow. The general form of the \mathbf{Q} equation is given in Appendix A. Here to decrease the number of parameters we have taken the coefficients of the advective and vorticity coupling to be 1 and have introduced a single flow coupling parameter λ as appropriate for passive $2d$ nematics. Note that with this choice λ is known to be finite in the limit where the strength S of nematic order vanishes [98, 99, 86].

The second term on the right hand side of Eq. (5.1) is the molecular field, $\mathbf{H} = -(\delta F / \delta \mathbf{Q})^T$, where the superscript T denotes the traceless part of the tensor, γ is the rotational friction, and F is the Landau-de Gennes free energy of a two-dimensional nematic [34], given by

$$F = \frac{1}{2} \int_{\mathbf{r}} \left\{ A(1-r) \text{Tr} \mathbf{Q}^2 + Ar (\text{Tr} \mathbf{Q}^2)^2 + K (\partial_i Q_{jk})^2 + \kappa (\partial_i \partial_j Q_{kl})^2 \right\}. \quad (5.4)$$

The first two terms in Eq. (5.4), with $A > 0$ an energy density scale, control the isotropic-nematic transition in the passive system, which is continuous in mean-field in two dimensions. The transition occurs at $r = 1$. For $r < 1$ the ground state of the free energy is a disordered state with $S = 0$. For $r > 1$ the ground state is an ordered nematic state with $S = S_0 = \sqrt{(r-1)/r}$. The third term in F is the elastic energy cost for deformation of the order parameter, with K a Frank constant. For simplicity we use a single elastic constant approximation

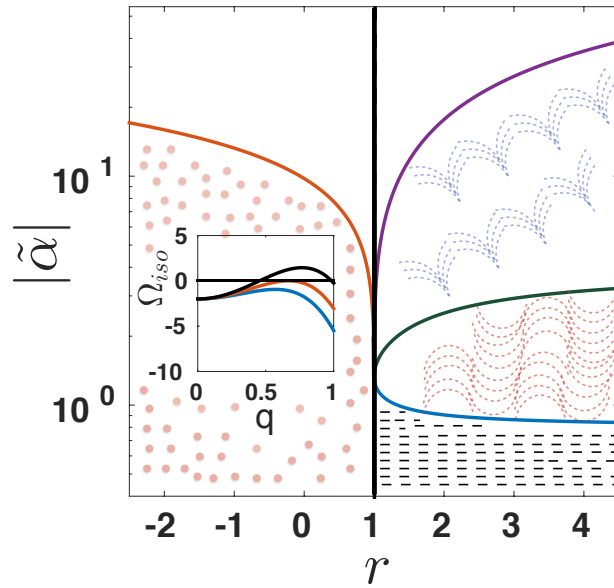


FIGURE 5.1: Phase diagram in the $(r, |\tilde{\alpha}|)$ plane obtained by linear stability analysis. The vertical black line at $r = 1$ is the mean-field transition between the disordered and ordered nematic states. The disordered state ($r < 1$) becomes unstable via an isotropic instability at the value of activity given in Eq. (5.12) (orange line). The ordered state ($r > 1$) first becomes unstable to the growth of bend fluctuations of the director field (blue line, Eq. (5.20) for $\psi = 0$). We also show the lines corresponding to the change in sign of the growth rate of splay fluctuations of the director (dark green line, Eq. (5.20) for $\psi = \pi/2$) and the magnitude of the order parameter (purple line, Eq. (5.22)). These additional instability lines correlate with the onset of more complex spatial structures with increasing activity, as suggested by the shading of the various regions, and eventually the onset of active turbulence (no shading). All the instability boundaries meet at a multicritical point where the uniform isotropic, uniform nematic and modulated phases coexist. Inset: the dispersion relation Ω_I (Eq. (5.11)) that controls the growth of order parameter fluctuations for $r < 1$ as a function of wavevector for three values of $|\tilde{\alpha}| = 10, 13.26, 17$ (from bottom to top). At the transition only one critical mode $q = q_c^I$ is unstable.

Above the transition the unstable modes lie in a band $q_-^I < q < q_+^I$.

which equates the cost of splay and bend deformations [34, 100]. The last term in Eq. (5.4) describes an effective surface tension of phenomenological strength κ , assumed isotropic for simplicity. This term provides stability at small length scales. The molecular field is then given by

$$\mathbf{H} = -A [1 - r + 2r \text{Tr} \mathbf{Q}^2] \mathbf{Q} + K \nabla^2 \mathbf{Q} - \kappa \nabla^4 \mathbf{Q}. \quad (5.5)$$

In the Stokes equation, Eq. (5.2), Γ is the friction from the substrate, η the shear

viscosity, and α is a measure of activity, with dimensions of stress: $\alpha > 0$ corresponds to contractile active stresses, as obtained for instance in monolayers of fibroblasts [29], while $\alpha < 0$ corresponds to extensile stresses, as obtained in suspensions of microtubule bundles [3] or *Bacillus subtilis* swimming in a nematic liquid crystal [44]. We have neglected elastic stresses that yield terms of higher order in the gradients of the alignment tensor.

We focus on the situation where frictional damping exceeds viscous forces, corresponding to length scales large compared to the hydrodynamic screening length $\ell_\eta = \sqrt{\eta/\Gamma}$. The Stokes equation can then be written as

$$\mathbf{v} \simeq \frac{\alpha}{\Gamma} \nabla \cdot \mathbf{Q}. \quad (5.6)$$

Using Eq. (5.6), the flow velocity \mathbf{v} can be eliminated from Eq. (5.1) to yield a description solely in terms of the dynamics of the order parameter field \mathbf{Q} ,

$$\begin{aligned} \partial_t \mathbf{Q} + \frac{\alpha}{\Gamma} [(\nabla \cdot \mathbf{Q}) \cdot \nabla] \mathbf{Q} &= -\frac{A}{\gamma} (1 - r + rS^2) \mathbf{Q} + \frac{K}{\gamma} \nabla^2 \mathbf{Q} \\ + \frac{\alpha\lambda}{2\Gamma} [\nabla (\nabla \cdot \mathbf{Q})]^{ST} + \frac{\alpha}{2\Gamma} \mathbf{\Omega}[\mathbf{Q}] - \frac{\lambda\alpha}{\Gamma} B(\mathbf{Q})\mathbf{Q} - \frac{\kappa}{\gamma} \nabla^4 \mathbf{Q}, \end{aligned} \quad (5.7)$$

where the superscript ST denotes the symmetric traceless part of a tensor, and we have used $\text{Tr } \mathbf{Q}^2 = S^2/2$. The antisymmetric tensor $\mathbf{\Omega}[\mathbf{Q}]$ arises from the coupling of alignment and vorticity and has components $\Omega_{ij} = Q_{ik} (\nabla_k \nabla_l Q_{lj} - \nabla_j \nabla_l Q_{lk}) - (\nabla_i \nabla_l Q_{lk} - \nabla_k \nabla_l Q_{li}) Q_{kj}$ and $B(\mathbf{Q}) = Q_{ij} \nabla^2 Q_{ij}/2$. In spite of the apparent complexity of Eq. (5.7), the role of activity is transparent. The first term on the second line of Eq. (5.7) is proportional to $\nabla \nabla \mathbf{Q}$. Hence to linear order in \mathbf{Q} , activity renormalizes the Frank constant K , rendering it anisotropic and, as we will see below, driving it to zero and even negative in a range of parameters. This results in the instability of homogeneous states and the onset of spatially modulated structures via a mechanism analogue to that of an equilibrium Lifshitz point [101, 50]. A negative value of the order parameter stiffness was assumed in

Refs. [17, 102, 92] as the mechanism responsible for driving pattern formation in continuum models of dry polar and nematic active fluids inspired by the Toner-Tu equations. Mechanisms that can lead to a negative stiffness have recently been identified for polar fluids [95, 96]. In particular, Ref [96] shows that hydrodynamic interactions mediated by active processes can drive a change in sign of the stiffness of a polar active fluid. Our work shows that in active nematic even screened flows in the overdamped limit can result in a negative nematic stiffness. Equation (5.7) has the structure of a generalized Swift-Hohenberg type equation for a tensorial order parameter, although it also includes nonlinearities usually neglected in the simplest models of this type. By examining various terms of Eq. (5.7), we identify two important length scales: the nematic correlation length $\ell_Q = \sqrt{K/|A(1-r)|}$ that diverges at the mean-field transition and the length $\ell_\kappa = \sqrt{\kappa/K}$ obtained by balancing order parameter stiffness and tension. In the following we examine the behavior of the system by tuning the parameter r that drives the system across the mean-field isotropic-nematic transition and the activity α . We choose $\ell_Q^0 = \sqrt{K/A}$ as unit of length and $\tau = \gamma/A$ as unit of time. Eq. (5.7) can then be written in terms of dimensionless quantities as

$$\begin{aligned} \partial_t \mathbf{Q} + \tilde{\alpha}[(\nabla \cdot \mathbf{Q}) \cdot \nabla] \mathbf{Q} = & - (1 - r + rS^2) \mathbf{Q} + \nabla^2 \mathbf{Q} \\ + \frac{\tilde{\alpha}\lambda}{2} [\nabla (\nabla \cdot \mathbf{Q})]^{ST} + \frac{\tilde{\alpha}}{2} \Omega[\mathbf{Q}] - \lambda \tilde{\alpha} B(\mathbf{Q}) \mathbf{Q} - \tilde{\kappa} \nabla^4 \mathbf{Q}. \end{aligned} \quad (5.8)$$

Several other groups have studied overdamped active nematics. We present a summary of previous work and comparison to our model in Section 5.5. Our minimal model of active nematics is controlled by only three dimensionless parameters: r , which controls the passive transition between uniform isotropic and ordered states, a dimensionless activity $\tilde{\alpha} = \alpha\gamma/\Gamma K$, and a dimensionless tension $\tilde{\kappa} = \kappa A/K^2 = (\ell_\kappa/\ell_Q^0)^2$. Additionally the behavior depends on the flow alignment parameter, λ . This microscopic parameter is controlled by molecular shape and

degree of nematic order, with $|\lambda| > 1$ corresponding to flow alignment of the nematic director in a shear flow and $|\lambda| < 1$ corresponding to flow tumbling [98]. Below we focus on elongated self-driven units, such as microtubule bundles or bacteria, where λ is positive, and consider the flow aligning case, hence restrict ourselves to $|\lambda| > 1$.

In the next section we examine the linear stability of both isotropic and nematic states and show that activity can render both unstable.

5.3 Linear stability of homogeneous states and “multicritical point”

In this section we examine the linear stability of the homogeneous, steady state solutions of Eq. (5.7) by considering the linear dynamics of fluctuations $\delta\mathbf{Q} = \mathbf{Q} - \mathbf{Q}^0$ of the order parameter from its uniform value, \mathbf{Q}_0 . The disordered state ($r < 1$) has $\mathbf{Q}^0 = 0$. In the ordered state ($r > 1$) we choose the x axis along the direction of broken symmetry, so that $Q_{ij}^0 = \frac{S_0}{2} (\delta_{ix}\delta_{jx} - \delta_{iy}\delta_{jy})$, with $S_0 = \sqrt{(r-1)/r}$. In this section we use dimensionful quantities to better highlight the physics of the various instabilities.

5.3.1 Isotropic state - $r < 1$

In this case $\mathbf{Q}^0 = 0$ and the linear dynamics of the fluctuations is controlled by the equation

$$\gamma\partial_t\delta\mathbf{Q} = -A(1-r)\delta\mathbf{Q} + K_I(\alpha)\nabla^2\delta\mathbf{Q} - \kappa\nabla^4\delta\mathbf{Q}, \quad (5.9)$$

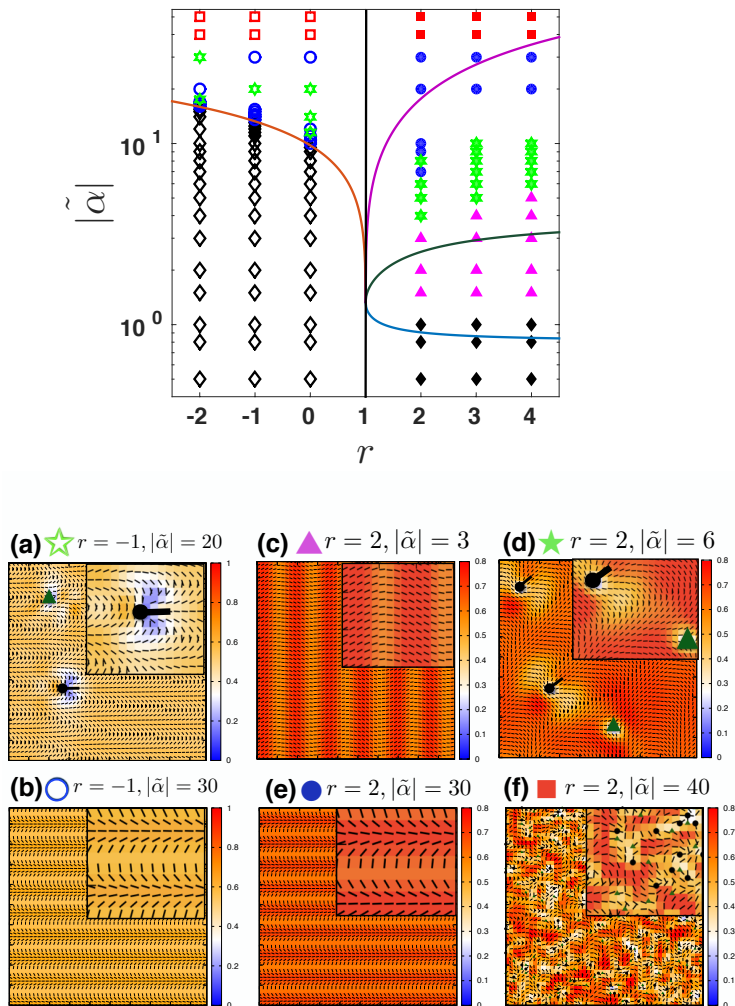


FIGURE 5.2: Numerical phase diagram and snapshots of the various steady states for $\tilde{\kappa} = 10$ and $\lambda = 1.5$. *Left panel*: Numerical phase diagram in the $(r, |\tilde{\alpha}|)$ plane. The vertical black line at $r = 1$ is the mean-field I-N transition from the isotropic ($r < 1$) to the nematic ($r > 1$) state. The symbols refer to various steady state configurations obtained by numerical solution of the nonlinear equations and quantified as described in the text. Open symbols are used for states with $r < 1$ and filled symbols for states with $r > 1$, as follows: uniform isotropic state (open black diamonds), uniform nematic (filled black diamonds), kink walls with defects (green stars), kink walls with no defects (blue circles), bend modulations (filled magenta triangles), turbulent state (red squares). The solid lines denote the various linear stability boundaries described in Fig. 5.1. Figures (a-f) show typical snapshots of the various states: kinks walls with (a and movie S1 in SI) and without (b and movie S2 in SI) defects for $r < 1$; (c and movie S3 in SI) bend modulations, (d and movie S4 in SI) kink walls with defects, (e and movie S5 in SI) kink walls with no defects, and (f and movie S6 in SI) turbulent state. Snapshots (c-f) are for $r > 1$. The color scale describes the magnitude of the order parameter S (the mean field value is $S_0 = 0.78$ in (c) to (f)). The black lines denote the direction of the director. Each snapshot also shows a blow up of the structure in the upper right corner. Disclination defects, when present, are denoted by green filled triangles ($-1/2$) and black filled circles ($+1/2$), with a short black solid line indicating the tail of the comet-like $+1/2$ defects move in the direction of the black dot.

where

$$K_I(\alpha) = K + \frac{\alpha\lambda\gamma}{2\Gamma} \quad (5.10)$$

is an effective elastic constant renormalized by activity. By expanding the fluctuation in Fourier components as $\delta\mathbf{Q} = \int_{\mathbf{r}} \mathbf{Q}_{\mathbf{q}}(t) \exp(i\mathbf{q} \cdot \mathbf{r})$, we immediately obtain the isotropic dispersion relation of the mode that controls the growth rate of fluctuations as

$$\Omega_I = - [A(1 - r) + K_I(\alpha)q^2 + \kappa q^4] / \gamma . \quad (5.11)$$

The evolution of the dispersion relation with activity is shown in the inset of Fig. 5.1. The effective stiffness K_I can become negative at large activity provided $\alpha\lambda < 0$, corresponding to either axially elongated active units ($\lambda > 0$) with extensile activity ($\alpha < 0$) or oblate active units ($\lambda < 0$) with contractile activity ($\alpha > 0$). The duality between elongated pushers and oblate pullers has been discussed before in ‘wet’ active fluids [13]. Here we will restrict ourselves to the case of elongated extensile swimmers with $\alpha\lambda < 0$. In this case the relaxation rate Ω_I becomes positive for $K_I < -K_c$, with $K_c = 2\sqrt{A|1 - r|\kappa}$, corresponding to

$$|\alpha| > \alpha_{cI} = \frac{2\Gamma}{\gamma\lambda} (K + K_c) , \quad (5.12)$$

and for a band of wave vectors $q_-^I \leq q \leq q_+^I$, with

$$q_{\pm}^I = \left[\frac{1}{2\kappa} \left(-K_I(\alpha) \pm \sqrt{[K_I(\alpha)]^2 - K_c^2} \right) \right]^{1/2} . \quad (5.13)$$

Note that K_c vanishes at the mean-field IN transition ($r = 1$). The wave vector of the fastest growing mode, corresponding to the maximum of the dispersion relation shown in the inset of Fig. 5.1, is $q_m^I = \sqrt{|K_I(\alpha)|/(2\kappa)} = \sqrt{K_c + \gamma\lambda(|\alpha| - \alpha_c)/(2\Gamma)} \sim (|\alpha| - \alpha_c)^{1/2}$, where the last approximate equality holds near the mean-field IN

transition, where $K_c = 0$. The fastest growing mode controls the length scale of the spatially modulated states. At onset ($|\alpha| = \alpha_c$) a single mode of wave vector $q_c^I = q_m^I(\alpha_c) = \sqrt{K_c/(2\kappa)}$ becomes unstable. Away from the onset of the instability, where $|K_I| > K_c$, we find $q_-^I \simeq \sqrt{A/|K_I|}$ and $q_+^I \simeq \sqrt{|K_I|/\kappa}$. The instability is driven by activity that softens the elastic energy cost of order parameter fluctuations, allowing the formation of ordered regions in the isotropic state. At long wavelengths ($q < q_-^I$) this destabilizing effect is balanced by the passive damping of the order parameter controlled by the rate A/γ . At short wavelengths ($q > q_+^I$) it is balanced by the surface tension κ associated with the creation of isotropic/nematic interfaces. The threshold for the instability shifts to higher magnitudes of activity as one moves deeper into the disordered state. This mechanism for pattern formation is formally analogue to that described in Ref. [103] for reproducing micro-organisms with a density-dependent diffusivity that can be driven to zero or even to negative values by the suppression of motility due to crowding. The instability of an isotropic suspension of pullers has been discussed before for polar swimmers [30], but it is a new result of this work in the context of nematics.

5.3.2 Ordered state - $r > 1$

We now examine the stability of the homogeneous ordered state for $r > 1$. We write directly linear equations for the Fourier components of δQ_{xx} and δQ_{xy} , given by

$$\gamma \partial_t Q_{xx}(\mathbf{q}) = - [2A(r-1) + K_S(\alpha)q^2 + \kappa q^4] Q_{xx}(\mathbf{q}) \quad (5.14)$$

$$\gamma \partial_t Q_{xy}(\mathbf{q}) = - [K_\theta(\alpha, \psi)q^2 + \kappa q^4] Q_{xy}(\mathbf{q}) + \frac{\alpha \gamma S_0}{\Gamma} q_x q_y Q_{xx}(\mathbf{q}), \quad (5.15)$$

Where

$$K_S(\alpha) = K + \frac{\alpha\lambda\gamma}{2\Gamma} \left(1 - \frac{S_0^2}{2}\right), \quad (5.16)$$

$$K_\theta(\alpha, \psi) = K + \frac{\alpha\gamma}{2\Gamma} (\lambda + S_0 \cos 2\psi), \quad (5.17)$$

with ψ the angle between the wave vector \mathbf{q} and the direction of order. The dynamics of fluctuations in the magnitude of the order parameter ($\sim Q_{xx}$) and the direction of broken symmetry ($\sim Q_{xy}$) are decoupled and the dispersion relation of the corresponding eigen-modes are given by

$$\Omega_S = - [2A(r-1) + K_S(\alpha)q^2 + \kappa q^4] / \gamma, \quad (5.18)$$

$$\Omega_\theta = - [K_\theta(\alpha, \psi)q^2 + \kappa q^4] / \gamma. \quad (5.19)$$

Once again, activity renormalizes the bare elastic constant K . At the mean-field transition at $r = 1$, $S_0 = 0$ and $K_S = K_\theta = K_I$, so that all three dispersion relations Ω_I , Ω_θ and Ω_S merge continuously. Both decay rates Ω_θ and Ω_S can become positive for flow aligning ($\lambda > 1$) extensile ($\alpha < 0$) nematics, signalling the instability of the homogeneous ordered state.

The decay rate of fluctuations in the direction of nematic order controlled by Ω_θ is positive when $K_\theta(\alpha, \psi) < 0$, corresponding to

$$|\alpha| > \alpha_c^\theta(\psi) = \frac{2K\Gamma}{\gamma(\lambda + S_0 \cos 2\psi)} \quad (5.20)$$

and the fastest growing wave vector is

$$q_{max}^\theta = \sqrt{\frac{|K_\theta(\alpha, \psi)|}{2\kappa}}. \quad (5.21)$$

The most unstable mode corresponds to bend fluctuations ($\psi = 0$), as expected for extensile systems, with $\alpha_c^{be} = \alpha_c^\theta(\alpha, \psi = 0) = 2K\Gamma/[\gamma(\lambda + S_0)]$.

The decay rate Ω_S is positive when $K_S(\alpha) < -\sqrt{2}K_c$, corresponding to

$$|\alpha| > \alpha_c^S = \frac{2\Gamma}{\gamma\lambda} \frac{2r}{r+1} \left(K + \sqrt{2}K_c \right). \quad (5.22)$$

The instability occurs for a band of wavevectors $q_-^S < q < q_+^S$, with

$$q_{\pm}^S = \pm \left[\frac{1}{2\kappa} \left(-K_S(\alpha) + \sqrt{[K_S(\alpha)]^2 - 2K_c^2} \right) \right]^{1/2} \quad (5.23)$$

and the wave vector of the fastest growing mode is $q_m^S = \sqrt{|K_S(\alpha)|/\kappa}$.

The linear stability phase diagram in the $(r, |\tilde{\alpha}|)$ plane is shown in Fig. 5.1 for an extensile system. All linear stability boundaries meet at $r = 1$ and $|\alpha| = 2K\Gamma/(\gamma\lambda)$. This represents a nonequilibrium multicritical point analogue to an equilibrium Lifshitz point, where ordered, disordered and modulated phases coexist. The blue line corresponds to the bend instability at $\alpha_c^\theta(\theta, \psi = 0)$. Also shown is the onset of instability $\alpha_c^\theta(\theta, \psi = \pi/2)$ of pure splay fluctuations (green line). This ‘*bend-to-splay*’ crossover has previously been identified as the mechanism of defect formation [20]. Finally, the purple line is the boundary α_c^S where fluctuations in the magnitude of the order parameter become linearly unstable. The modulated phase near onset is expected to have different structures for r above and below 1 because the instability is isotropic in wave vector for $r < 1$, but dominated by bend fluctuations for $r > 1$. As we will see below, this is borne out by the numerical solution of the nonlinear equations. In contractile systems, in contrast, the first linear instability is controlled by splay fluctuations.

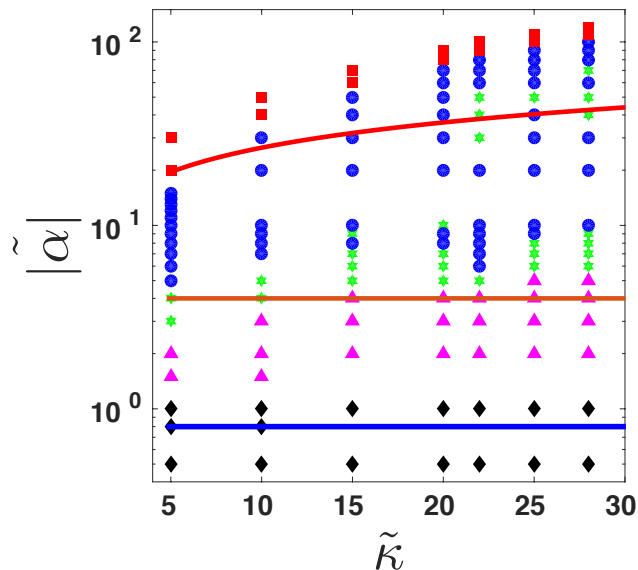


FIGURE 5.3: Numerical phase diagram in the $(\tilde{\kappa}, |\tilde{a}|)$ plane for $r = 2$. The lines are the linear stability boundaries discussed in section 5.3: bend instability (blue line), splay instability (orange line), instability of magnitude of order parameter (red line). The various symbols have same meaning as in Fig. 5.2.

5.4 Numerical results: kink walls, defect alignment and turbulence

We have integrated numerically Eq. (5.8) in a square box of side L with bi-periodic boundary conditions. The \mathbf{Q} dynamics is integrated numerically on a square domain of grid size $\Delta x = \Delta y = 1$ using predictor-corrector method with the central difference scheme and a time step $\Delta t = 10^{-3}$. We have considered system sizes $L = 50$ and $L = 100$. Most of the numerical results for $r > 1$ have been obtained by starting the system in a uniform nematic state ordered along the x -axis with some superimposed noise. We also have verified that our results are robust against the selection of initial conditions for all values of r .

We vary activity, the distance r from the mean-field order-disorder transition, and the tension $\tilde{\kappa}$. As activity is increased at fixed r or fixed $\tilde{\kappa}$, we obtain a succession

of increasingly disordered structures summarized in the phase diagrams shown in Figs. 5.2 and 5.3.

To characterize the various states we have measured the local and global degree of nematic order and the number of defects. We introduce two quantities to quantify nematic order

$$\langle S \rangle = 2\sqrt{\langle Q_{xx}^2 + Q_{xy}^2 \rangle}, \quad (5.24)$$

$$\langle Q \rangle = 2\sqrt{\langle Q_{xx} \rangle^2 + \langle Q_{xy} \rangle^2}, \quad (5.25)$$

where the brackets denote a spatial average over the system. Both quantities will of course be finite in a state with uniform nematic order. On the other hand, recalling that $Q_{xx} = (S/2) \cos 2\theta$ and $Q_{xy} = (S/2) \sin 2\theta$, it is easy to recognize that a state with large but randomly oriented nematic domains will be characterized by a finite value of $\langle S \rangle$ but a vanishing value of $\langle Q \rangle$ (in the limit of large system size). For this reason we refer to $\langle S \rangle$ as a measure of the amount of local order in the system, while $\langle Q \rangle$ characterizes global nematic order at the scale of the system size. Of course in a uniform nematic state $\langle S \rangle = \langle Q \rangle$.

Activity yields spatial structures: Activity drives uniform nematic states towards more disordered configurations and builds up local nematic order in uniform isotropic states. This is displayed in Fig. 5.4(a) that shows the evolution with activity of local nematic order $\langle S \rangle$ for values of r below (red curves) and above (blue curves) the mean field I-N transition. At low activity the system is in a homogeneous state and $\langle S \rangle$ has its mean-field value. For $r < 1$ $\langle S \rangle$ remains identically zero up to the value of activity corresponding to the linear instability of the isotropic state, and then grows with activity. The result that activity builds nematic order may seem surprising, but is consistent with recent results for wet systems, where flows induced by active stresses were shown to renormalize the

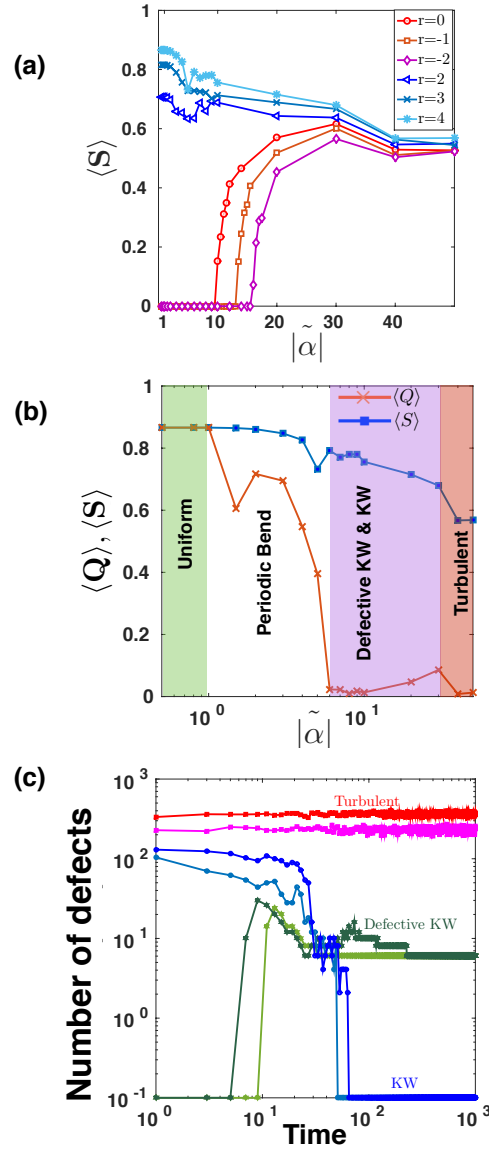


FIGURE 5.4: (a) $\langle S \rangle$ as a function of activity. The top three curves correspond to $r > 1$ and show the decay of $\langle S \rangle$ with increasing activity from its mean-field value $S_0 = \sqrt{(r-1)/r}$ at zero activity. The bottom three curves correspond to $r < 1$, where $\langle S \rangle$ ramps up sharply from its low activity value of zero at the onset $|\alpha_{cI}|$ of the linear instability. The curves through the data are a guide to the eye. (b) The evolution with activity of the two measure of nematic order $\langle Q \rangle$ (red crosses) and $\langle S \rangle$ (blue squares) for $r = 4$, $\tilde{\kappa} = 10$ and $\lambda = 1.5$. The shading denotes the various regimes as estimated from the numerics. At low activity the system is in a uniform nematic state (light green) and $\langle Q \rangle = \langle S \rangle = S_0 = 0.86$. In the region of bend modulations (white) $\langle S \rangle$ remains close to its maximum value, while $\langle Q \rangle$ drops sharply, remaining close to zero in all subsequent regimes. The slight increase of $\langle Q \rangle$ near the transition from KW to turbulence reflects the alignment of KW in this region. (c) Number of defects as a function of time for six values of activity for $r = 4$: $|\tilde{\alpha}| = 6, 7$, corresponding to KW with defects (green curves), $|\tilde{\alpha}| = 20, 30$, corresponding to defect-free KW (blue curves), and $|\tilde{\alpha}| = 40, 50$, corresponding to the turbulent state (red curves).

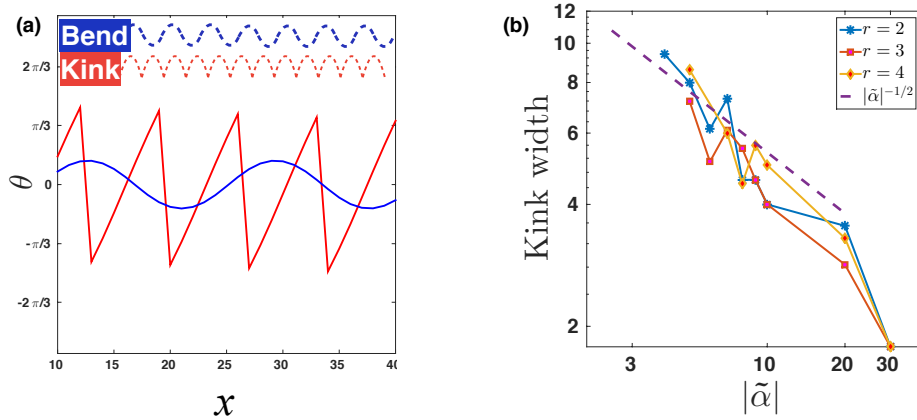


FIGURE 5.5: (a) Profiles of the angle θ of the director with the direction of mean order for *bend* (blue curve, $|\tilde{\alpha}| = 3$) and *kink walls* (red curve, $|\tilde{\alpha}| = 20$), $\tilde{\kappa} = 10$ and $\lambda = 1.5$. The director profiles for both deformations are shown at the top of the figure. (b) Width of kink walls versus activity for $r = 2, 3, 4$, $\tilde{\kappa} = 10$ and $\lambda = 1.5$. The dashed line has slope $-1/2$.

location of the IN transition [93].

For $r > 1$ the system is in a uniform nematic state at zero activity with $\langle S \rangle = \sqrt{(r-1)/r}$. Activity disorders the system driving the onset of spatial structures of increasing complexity, and $\langle S \rangle$ decreases continuously. At large activity where the system enters the turbulent regime, the distance r from the mean-field critical point ceases to provide a distinction between states and both sets of curves ($r > 1$ and $r < 1$) converge to the same value of $\langle S \rangle$. It should be stressed that of course the line of I-N transition is itself generally renormalized by activity via coupling to viscous flows [93]. These effects are however, not incorporated in our model that considers length scales much larger than the hydrodynamic screening length ℓ_η .

We now characterize the various regimes obtained by increasing activity.

Bend modulations: When $r > 1$ the uniform active nematic state becomes unstable to bend fluctuations (see movie S3 in SI) of the director at $|\alpha| > \alpha_c^{be}$. This yields a state with bands of alternating high and low value of the order parameter

S and associated bend deformations of the director, as shown in Fig. 5.2(c). The bands exhibit a high degree of smectic order. In wet systems this is the regime of spontaneous flow [6], and was reported in most previous studies with and without frictional damping [49, 16, 19], but not in Ref. [92]. The activity threshold found numerically matches well the value obtained from linear stability analysis, as evident from Figs. 5.2(a) and (b). The mean order parameter $\langle S \rangle$ is lower than its mean-field value but remains finite, as shown in Fig. 5.4(a), while $\langle Q \rangle$ quickly drops to 0, as evident from Fig. 5.4(b). Beyond the activity where the degree of global order $\langle Q \rangle$ drops to zero, the system does not have a memory of the direction of initial order. Hence, structures obtained at higher activity are expected to be the same for $r > 1$ and $r < 1$. This is also evident from the phase diagram of Fig. 5.2. We discuss these states in the following.

Kink walls (KW): Upon increasing activity, the magnitude of $\langle S \rangle$ decreases and director deformations become larger, acquiring a splay character (see movies S2 and S5 in SI). The system organizes in a structure of parallel kink walls, with large-scale smectic order, resembling the patterns seen in living liquid crystals of *B. subtilis* swimming in a passive nematic [44, 104]. The width and spacing of the kink walls is set by the length scale $\ell_{KW} \sim (q_m^S)^{-1} \sim \sqrt{\Gamma\kappa/(|\alpha|\gamma)} \sim |\alpha|^{-1/2}$, as shown in Fig. 5.5(b) and seen in experiments [44]. The activity range over which the aligned KW are observed is not, however, sufficient to establish scaling. To highlight the distinction between bands of bend modulation and kink walls, we show in Fig. 5.5(a) the director profile for the two structures. Due to the large splay deformation of the director and the associated suppression of the local value of S , defect pairs unbind and travel along the kink walls (Fig. 5.2 (c)). The majority of defect pairs annihilate at long times, as evident from the plot of number of defects versus time shown in Fig. 5.4(c) (dark and light green curves), resulting in a state with a small concentration of stable unbound defects (typically fewer than 10 for $L = 100$), as shown in Fig. 5.4(c). The few remaining $+1/2$ defects move along the

kink walls maintaining essentially parallel relative orientation (see movies S1 and S4 in SI), i.e. exhibit polar order as reported in [4, 91]. This behavior is observed in a very narrow range of activity and only for sufficiently large values of $\tilde{\kappa}$, as shown in the phase diagram in Fig. 5.3.

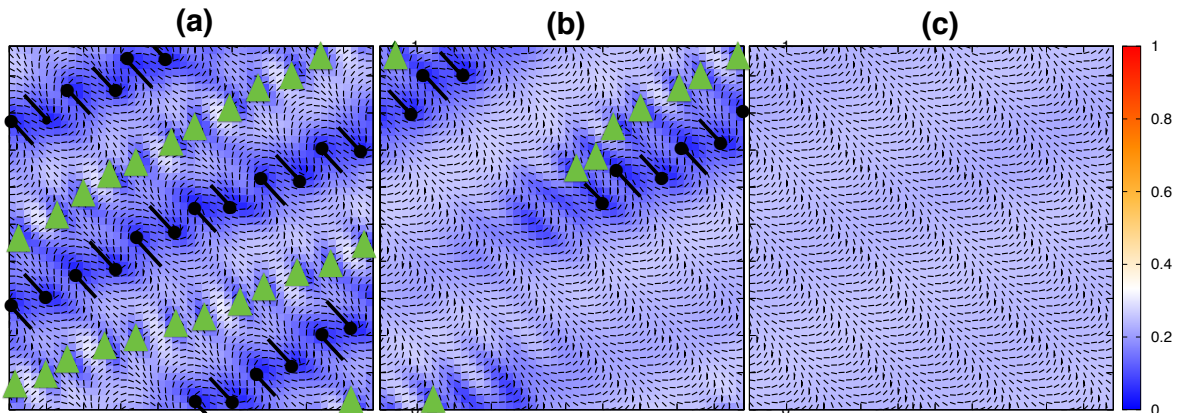


FIGURE 5.6: Snapshots at (a) $t = 92\tau$, (b) $t = 143\tau$ and (c) $t = 170\tau$ showing the transient nematic alignment of defects for $r = -1$, $|\tilde{\alpha}| = 14$, $\tilde{\kappa} = 10$ and $\lambda = 1.5$ (see movie S7 in SI). These structures are obtained for values of activity close to the boundary of linear stability of the uniform mean-field isotropic state, which is at $\alpha_{cI} = 13.2$ for the parameters used here. The defects are highlighted using the same convention as described in the caption of Fig. 5.2.

Defect ordering: As discussed in the Introduction, experiments have reported nematic order of the orientation of $+1/2$ defects in microtubule bundle suspensions [4]. Previous numerical work has observed both nematic [92] and polar [4, 91] order of the defects in dry systems and a lattice of flow vortices with rows of nematic-like ordered defects at the wet-to-dry crossover [94]. In our model we have observed two types of defect-ordered structures.

For $r < 1$, and in a very narrow range of activity near the linear stability boundary, we observe *nematic* alignment of the axes of the $+1/2$ defects similar to the one seen in numerical models of Refs. [92, 94], as shown in Fig. 5.6(a) and movie S7(in SI). Unlike previous work, we find, however, that these rows of defects are a transient state. At long times all the defects annihilate leading to a state of kink walls, with no unbound defects, as displayed in Fig. 5.6 for $r = -1$ and $|\tilde{\alpha}| = 14$.

Note that the work by Doostmohammadi *et al.* [94] included flow, suggesting that this may play a role in stabilizing these nematic defect rows. On the other hand, the work by Oza and Dunkel [92] is, like ours, a dry model. We have verified that the rows of nematically aligned defect are long lived for the parameter values used in Ref. [92] where many of the orientation-flow couplings are set to zero (see Appendix A). Clearly more work is needed to fully explore the very large parameter space of these rich models.

In addition, we observe stable *polar* order of the orientation of the $+1/2$ defects in the regime of defective kink walls displayed in Fig. 5.2(d) and more clearly evident in Supplementary movie S4. This type of order, with defects situated at the end of kink walls, is the same as observed previously in simulations of dry systems [4, 91].

Turbulent state: At even higher activity, when the width of the kink walls become of the order of ℓ_Q^0 , we find a turbulent state with proliferation of unbound defect (see movies S6 and S8 in SI). The evolution of the defect density with time is shown in Fig. 5.4(c) (red and orange curves).

5.5 Comparison to previous work

The theoretical literature on continuum models of the emergent dynamics of active nematic liquid crystals has seen a rapid growth in recent years, with several papers directly related to the work presented here. For this reason we think it useful to summarize in this section the relation of our work to a few others [94, 91, 92] that also discuss the elimination of the flow velocity in the overdamped limit by balancing frictional and active forces.

Perhaps most closely related to our work is the one by Putzig *et al.*, where the authors eliminate flow in favor of active stresses, but retain the dynamics of the density. In the density equation flow elimination leads to the curvature induced

currents that have been studied extensively in the literature [9]. Allowing for density variations yields the previously discussed phase separation in alternating bands of ordered and disordered regions in a very narrow region near the mean field isotropic-nematic transition [ref], but does not seem to affect the splay or bend instability of the order parameter which yields modulated states as found in our model. These authors retain general values for the various parameters that couple orientation and flow (see Appendix A for details) and find robust polar alignment of the orientation of the $+1/2$ defects and modulated kink walls structures. For our choice of such flow-orientation couplings, the same stable polar ordering of defects is obtained only in the narrow region of parameters identified by filled green stars in Fig. 5.1 and Fig. 5.2.

Finally, Putzig *et al.* do not discuss the complete phase diagram across both the mean field isotropic and nematic states, nor highlight the role of the negative effective stiffness as a generic pattern formation mechanism.

A \mathbf{Q} -only model similar to ours was recently proposed by Oza and Dunkel [92], who consider a compressible active nematic with constant density, but assume from the outset a negative value of the elastic stiffness. Additionally, these authors neglect the coupling of orientation to both shear flows ($\lambda = 0$) and vorticity (see also Appendix A). For this special parameter values they find stable nematic alignment of the $+1/2$ defects that persist in steady state at low activity. This is in contrast to our model where nematic defect ordering is always transient. The ad hoc assumption of negative stiffness (as opposed to a stiffness that is driven negative by activity) yields a phase diagram where the homogenous states are found to be unstable even for zero value of activity.

Finally, Doosmohammadi *et al.* consider an active nematic suspension with both

substrate friction and viscous flow. An intriguing result of this work is the observation of stable rows of aligned defects with nematic order of the $+1/2$ defects perhaps resembling the structures reported in suspensions of microtubules [4]. The ordering of defects is accompanied by an ordered lattice of flow vortices of alternating sign. While we observe similar states of rows of defects with nematic alignment as shown in Fig. 5.6, we find that these states are transient and the steady state is defect free in this regime of parameters. This suggests that flow may be needed to stabilize the nematic order of defects. These authors also state that when frictional damping is the dominant mechanism for dissipation, the system no longer exhibits spontaneous defect proliferation. This may follow from the fact that they examine behavior by increasing friction at *fixed activity*, which in the overdamped regime is equivalent to decreasing the effective activity α that enters in the combination α/Γ .

5.6 Conclusion and Discussion

We have shown that at length scales larger than the hydrodynamic screening length a compressible active nematic film can be described by a single equation for the tensor order parameter \mathbf{Q} . Activity renormalizes the elastic stiffness of the nematic and drives it to negative values, destabilizing *both* the ordered and disordered homogeneous states and providing a mechanism for pattern formation analogue to that at play at an equilibrium Lifshitz point. Activity plays different roles depending on the value of the parameter r that tunes the proximity to the mean field isotropic-nematic transition of the passive system. For $r < 1$, corresponding to a uniform passive isotropic state in mean-field, activity builds up local nematic order, while it disrupts it for $r > 1$, which corresponds to the ordered state in mean-field. In both cases a moderate activity yields spatial structures that are stabilized at small length scales by a surface tension that favors the formation

of isotropic/nematic interfaces. Our work provides a minimal model that unifies many previously presented results in a phase diagram that includes: (i) a regime of spontaneous bend deformations of the director field that corresponds to the spontaneous laminar flow state of wet systems; (ii) kink walls with unbound defects; (iii) defect-free kink walls; (iv) and finally chaotic dynamics with proliferation of topological defects. The regimes of bend deformations and kink walls both exhibit large-scale smectic order, similar to the one observed in suspensions of *Bacillus subtilis* swimming in cholesteric liquid crystals [44, 104], where substrate friction is indeed the dominant dissipation process.

Defect pairs unbind at the boundaries of kink walls, where nematic order distortion are largest, and zip along the walls, leaving large distortions in their trail (see SI movie S4). As activity increases, kink walls begin to meander. This eventually results in the loss of smectic order and the onset of the chaotic spatio-temporal dynamics that has been referred to as active turbulence, of the value of r . The finding that activity builds up nematic order in the regime where the passive system is isotropic was also reported in Ref. [93] for an active nematic where flow dominates over viscous dissipation. In this case it arises because flows due to active stresses effectively suppress the damping of the nematic order parameter, shifting the IN transition and enhancing the nematic correlation length. In our overdamped system the enhancement arises from nonlinear terms coupling the order parameter to active flows.

The effective equation for the order parameter obtained here is similar to a Swift-Hohenberg equation which is known to generically give rise to modulated phases. The additional nonlinearities and anisotropies present in our model as compared to conventional Swift-Hohenberg models do not affect the symmetry of the specific nonequilibrium structures, but only the parameter values controlling the crossover between the various regimes. In particular, the cubic nonlinearity in the term proportional to $\mathbf{B}(\mathbf{Q})$ on the right hand side of Eq. (5.3) is necessary to ensure

that local nematic order as quantified by $\langle S \rangle$ remain bounded. Our work therefore shows that the spatially modulated structures arising in active systems, especially the kink walls, are a generic consequence of the structure of the active hydrodynamic equations and identifies of the softening of the elastic stiffness due to activity as a generic mechanism for pattern formation in active systems dominated by frictional damping.

Using this model, we demonstrate that activity destabilizes not only the uniform ordered state, as well established in the literature, but also the mean-field disordered state. As well established, activity yields defect unbinding, but the proliferation of unbound defects does not grow monotonically with activity. This is evident from the sequence of steady states shown in the phase diagrams of Figs. 5.1 and 5.2 we find a state of kink walls with defects in a range of activity that give way to defect-free kink walls at higher activity. Defect proliferation is the result of two competing effects: the unbinding of defects pairs that occurs mainly along kink walls and increases with activity and the pair annihilation that is largely controlled by the speed of the $+1/2$ defects, and of course defect density. Both mechanisms depend on activity and our findings suggest that one may dominate over the other in different regions of parameter space. While defect unbinding in extensile systems has been associated with a transition to regime dominated by splay deformation of the order parameter, more work is needed for a quantitative understanding of how the creation and annihilation rate depend on activity and flow.

Finally, experiments in active microtubule suspension at an oil-water interface have reported a remarkable nematic alignment of $+1/2$ defect over large scales [4]. Both nematic and polar defect alignment have been reported in previous numerical studies of various models [4, 94, 92, 91]. Here we obtain both nematic and polar alignment of the orientation of the $+1/2$ defects in different regions of parameters. Unlike previous work, we find, however, that nematic order is always transient

when flow is completely screened by friction. Polar order is, however, stable, albeit in a narrow region of parameters.

A more subtle interplay of viscous and frictional dissipation may stabilize this defect-ordered state as obtained in [94] using a full hydrodynamic model, but more work remains to be done to understand the origin of this topological order.

5.7 Acknowledgments

We thank Ananyo Maitra and Sriram Ramaswamy for insightful discussions. This work was supported by National Science Foundation through award DMR-1305184, DGE-1068780 and by the Syracuse Soft Matter Program.

Appendix C

C.1 Overdamped nematic in $2d$: General equations

Here we present the general equations for the tensor order parameter \mathbf{Q} of an active nematic on a substrate. The presence of the substrate breaks Galilean invariance, removing the constraints that determine the sign and value of the coefficients of the co-rotational derivative that couple alignment and flow. In general, the equation for the \mathbf{Q} -tensor takes the form

$$\partial_t \mathbf{Q} + \lambda_C (\mathbf{v} \cdot \nabla) \mathbf{Q} - \lambda_R [\mathbf{Q}, \boldsymbol{\omega}] = \mathbf{S}(\mathbf{Q}, \nabla \mathbf{v}) + \frac{\mathbf{1}}{\gamma} \mathbf{H}, \quad (\text{C.1.1})$$

where

$$\begin{aligned} \mathbf{S} = & \lambda_1 \left[\mathbf{D} - \frac{1}{d} \text{Tr}(\mathbf{D}) \mathbf{1} \right] + \lambda'_2 \left[\mathbf{Q} \cdot \mathbf{D} + \mathbf{D} \cdot \mathbf{Q} - \frac{2}{d} \text{Tr}(\mathbf{Q} \cdot \mathbf{D}) \mathbf{1} \right] \\ & + \lambda_2 \frac{2}{d} \mathbf{Q} \text{Tr}(\mathbf{D}) - \lambda_3 \mathbf{Q} \text{Tr}(\mathbf{Q} \cdot \mathbf{D}), \end{aligned} \quad (\text{C.1.2})$$

with d the dimensionality, \mathbf{D} and $\boldsymbol{\omega}$ the symmetrized strain rate and vorticity defined in the main text after Eq. (5.3) and $[\mathbf{A}, \mathbf{B}] = \mathbf{A} \cdot \mathbf{B} - \mathbf{B} \cdot \mathbf{A}$. In system with

Galilean invariance the coefficients of the advective derivative and the orientation-vorticity coupling are constrained to have unit value, or

$$\lambda_C = \lambda_R = 1 . \quad (\text{C.1.3})$$

Additionally, in passive liquid crystals the other parameters coupling orientation and flow have been calculated [86] and are generally taken as

$$\begin{aligned} \lambda'_2 &= -\lambda_2 = 1 , \\ \lambda_1 &= \lambda_3 = \lambda . \end{aligned} \quad (\text{C.1.4})$$

In $2d$ the fact that \mathbf{Q} is a symmetric traceless tensor yields the identity

$$\mathbf{Q} \cdot \mathbf{D} + \mathbf{D} \cdot \mathbf{Q} - 1 \text{Tr}(\mathbf{Q} \cdot \mathbf{D}) = \mathbf{Q} \text{Tr}(\mathbf{D}) . \quad (\text{C.1.5})$$

Thus for a $2d$ active nematic on a substrate the matrix \mathbf{S} can be written without loss of generality as

$$\mathbf{S} = \lambda_1 \left[\mathbf{D} - \frac{1}{d} \text{Tr}(\mathbf{D}) \right] + \lambda_2 \mathbf{Q} \text{Tr}(\mathbf{D}) - \lambda_3 \mathbf{Q} \text{Tr}(\mathbf{Q} \cdot \mathbf{D}) . \quad (\text{C.1.6})$$

In order to reduce the number of parameters in our work we have taken $\lambda_C = \lambda_R = 1$, $\lambda_2 = 0$ and $\lambda_1 = \lambda_3 = \lambda$. We now make an explicit comparison between our model and the equations used in a few other recent works that are most directly relevant to ours.

Oza and Dunkel [92] : Like us, these authors have considered a compressible, overdamped active nematic with constant density. These authors have chosen $\lambda_C = -\lambda_2 = 1$ and $\lambda_1 = \lambda_3 = 0$. The parameter λ_R (denoted as κ in their work) is retained as arbitrary in the equations, but set to zero in the numerical calculations. As a result, the only term coupling orientation and flow is a convective term of

the form $\nabla \cdot (\mathbf{v}\mathbf{Q}) = (\mathbf{v} \cdot \nabla)\mathbf{Q} + \mathbf{Q}(\nabla \cdot \mathbf{v})$. The only active terms then come from eliminating the flow using Eq. (5.6). These terms cannot yield the activity-induced suppression of the nematic stiffness, which is therefore simply assumed to be negative from the outset. One issue with this formulation is that the model predicts that the homogeneous states are unstable even at zero activity.

Putzig et al. [91] : These authors consider an overdamped active nematic and eliminate flow using Eq. (5.6), but allow the density to vary, although it is a little unclear whether their density should be interpreted as the concentration of active units or the density of the suspension. They work in $2d$ and consider arbitrary values for the parameters coupling concentration and flow. Taking advantage of the identity (C.1.5), and denoting with a subscript P the parameters of Ref. [91] when different from ours, their equations correspond to the following choice: $\lambda_2 = \lambda_2^P - \lambda_C$, $\lambda_3 = 0$, with λ_1 , λ_C and λ_R allowed to have generic values.

Doostmohammadi et al. [94] : These authors consider an active nematic *suspension* in $3d$ and include both viscous flows and friction with a substrate. All the parameters coupling orientation and flow are assumed to have the value they would have in a passive system with Galilean invariance. They assume the total density of the suspension to be constant and require the flow to be incompressible, but allow the concentration of active particles to vary.

C.2 Linear Modes for general flow coupling parameters

In this Appendix we discuss the linear modes obtained by using the general form of the equations for an overdamped nematic as given in Eqs. (C.1.1) and (C.1.6) for both the case of compressible and incompressible flows.

Compressible overdamped nematic. In this case, after eliminating the flow using Eq. (5.6), the linearized equations for the Fourier amplitudes of the fluctuations of \mathbf{Q} about a uniform nematic state ($r > 1$) are given by

$$\begin{aligned}\partial_t Q_{xx} &= -\frac{1}{\gamma} [2A(r-1) + K^{xx}(\alpha, \psi)q^2 + \kappa q^4] Q_{xx} \\ &\quad - \frac{\lambda_2 \alpha}{2\Gamma} S_0 \sin 2\psi q^2 Q_{xy}, \\ \partial_t Q_{xy} &= -\frac{1}{\gamma} [K^{xy}(\alpha, \psi)q^2 + \kappa q^2] Q_{xy} + \frac{\lambda_R \alpha}{2\Gamma} S_0 \sin 2\psi q^2 Q_{xx},\end{aligned}\tag{C.2.1}$$

where

$$K^{xx}(\alpha, \psi) = K + \frac{\lambda_1 \alpha}{2\Gamma} + \frac{\lambda_2 \alpha}{2\Gamma} S_0 \cos 2\psi - \frac{\lambda_3 \alpha}{4\Gamma} S_0^2, \tag{C.2.2}$$

$$K^{xy}(\alpha, \psi) = K + \frac{\lambda_1 \alpha}{2\Gamma} + \frac{\lambda_R \alpha}{2\Gamma} S_0 \cos 2\psi, \tag{C.2.3}$$

with ψ the angle between the wave vector and the ordering direction. When $\lambda_2 = 0$ and $\lambda_1 = \lambda_3 = \lambda$, the above expressions reduce those given in Eqs. 5.16 and 5.17 of the main text. The effective stiffnesses K^{xx} and K^{xy} can always be driven negative at large extensile activities. Additionally, Eqs. (C.2.1) and (C.2.2) decouple for pure bend and splay deformations corresponding to $\psi = 0$ (bend) and $\psi = \pi/2$ (splay). Along these directions the instabilities of both director and order parameter magnitude have the same qualitative behavior as for the parameters used in the main text, with only quantitative differences. For general directions, the modes are coupled, but again the various instabilities and regimes are qualitatively unchanged.

Incompressible overdamped nematic. When the flow is incompressible, it is not possible to obtain a single closed nonlinear PDE for \mathbf{Q} . One can still, however, explicitly eliminate the velocity in the linearized equations for the fluctuations. The dynamics of the Fourier amplitude of fluctuations about the ordered state

($r > 1$) is then given by

$$\begin{aligned} \partial_t Q_{xx} = & -\frac{1}{\gamma} [2A(r-1) + K^{xx}(\alpha, \psi)q^2 + \kappa q^4] Q_{xx} \\ & + \frac{\alpha}{2\Gamma} \sin 2\psi [\lambda_1 \cos 2\psi - \lambda_3 S_0^2/2] q^2 Q_{xy} , \end{aligned} \quad (\text{C.2.4})$$

$$\begin{aligned} \partial_t Q_{xy} = & -\frac{1}{\gamma} [K^{xy}(\alpha, \psi)q^2 + \kappa q^4] Q_{xy} \\ & + \frac{\alpha}{2\Gamma} \sin 2\psi [\lambda_1 \cos 2\psi + \lambda_R S_0] q^2 Q_{xx} , \end{aligned} \quad (\text{C.2.5})$$

where

$$K^{xx}(\alpha, \psi) = K + \frac{\alpha\gamma}{2\Gamma} \sin^2 2\psi (\lambda_1 - \lambda_3 S_0^2/2) , \quad (\text{C.2.6})$$

$$K^{xy}(\alpha, \psi) = K + \frac{\alpha\gamma}{2\Gamma} \cos 2\psi (\lambda_1 \cos 2\psi + \lambda_R S_0) . \quad (\text{C.2.7})$$

Once again, the modes decouple for pure bend and splay fluctuations, with

$$K^{xx}(\alpha, \psi = 0) = K^{xx}(\alpha, \psi = \pi/2) = K , \quad (\text{C.2.8})$$

$$K^{xy}(\alpha, \psi = 0) = K + \frac{\alpha\gamma\lambda_1}{2\Gamma} \left(1 + \frac{\lambda_R S_0}{\lambda_1} \right) , \quad (\text{C.2.9})$$

$$K^{xy}(\alpha, \psi = \pi/2) = K + \frac{\alpha\gamma\lambda_1}{2\Gamma} \left(1 - \frac{\lambda_R S_0}{\lambda_1} \right) . \quad (\text{C.2.10})$$

The fastest growing unstable mode is along the direction corresponding to pure bend for extensile systems and to pure splay for contractile ones, as shown in Fig. B1 for extensile systems, and describes the growth of director fluctuations. However, in incompressible systems the mode controlling the dynamics of fluctuations in the order parameter amplitude is stable along these special directions and becomes unstable only in a narrow range of angles ψ centered around $\psi = \pi/4$ and in a narrow range of activity. This difference may lead to the suppression of defect formation in frictional systems reported in Ref. [94], but verifying this requires numerical investigations beyond the scope of the present work.

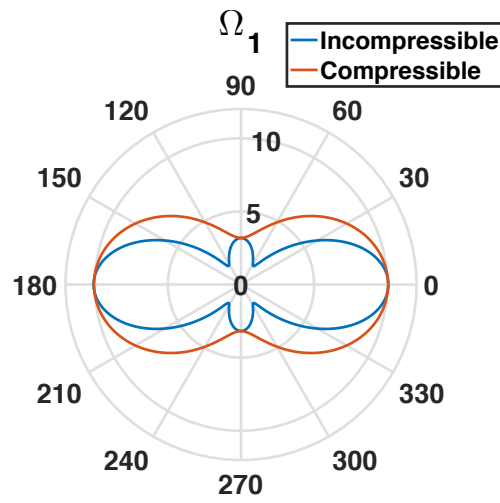


FIGURE B1: Polar plot of the growth rate of the most unstable mode (this is the mode that for $\psi = 0, \pi/2$ describes fluctuations in the director $\sim \Delta Q_{xy}$) as a function of the angle ψ for fixed $q = 0.7$, chosen such that all directions are unstable, and extensile systems. For both, incompressible (blue curve) and compressible (red curve) flows, the growth rate is largest for $\psi = 0, \pi$, corresponding to bend fluctuations. The parameter values used for the figure are $\lambda_1 = 1.5$, $\lambda_3 = 1.5$, $\lambda_R = 1$, $\lambda_C = 1$ and $\tilde{\alpha} = -20.0$, with units chosen as in the main text.

Bibliography

- [1] Gil Henkin, Stephen J. DeCamp, Daniel T. N. Chen, Tim Sanchez, and Zvonimir Dogic. [Tunable dynamics of microtubule-based active isotropic gels](#). *Philosophical Transactions of the Royal Society of London A: Mathematical, Physical and Engineering Sciences*, **372**, 0142, 2014.
- [2] M. C. Marchetti, J. F. Joanny, S. Ramaswamy, T. B. Liverpool, J. Prost, Madan Rao, and R. Aditi Simha. [Hydrodynamics of soft active matter](#). *Rev. Mod. Phys.*, **85**, 1143–1189, 2013.
- [3] Tim Sanchez, Daniel T. N. Chen, Stephen J. DeCamp, Michael Heymann, and Zvonimir Dogic. [Spontaneous motion in hierarchically assembled active matter](#). *Nature*, **491**, 431–434, 2012.
- [4] DeCamp Stephen J., Redner Gabriel S., Baskaran Aparna, Hagan Michael F., and Dogic Zvonimir. [Orientational order of motile defects in active nematics](#). *Nat Mater*, **14**(11), 1110–1115, nov 2015.
- [5] F. Nedelec, T. Surrey, AC. Maggs, and S. Leibler. [Self-organization of microtubules and motors](#). *Nature*, **389**, 305–308, 1997.
- [6] R. Voituriez, J. F. Joanny, and J. Prost. [Spontaneous flow transition in active polar gels](#). *Europhys. Lett.*, **70**, 404–410, 2005.

- [7] D. Marenduzzo, E. Orlandini, M. E. Cates, and J. M. Yeomans. [Steady-state hydrodynamic instabilities of active liquid crystals: Hybrid lattice Boltzmann simulations](#). *Phys. Rev. E*, **76**, 031921, 2007.
- [8] Luca Giomi, M. Cristina Marchetti, and Tanniemola B. Liverpool. [Complex Spontaneous Flows and Concentration Banding in Active Polar Films](#). *Phys. Rev. Lett.*, **101**, 198101, 2008.
- [9] S. Ramaswamy, R. Aditi Simha, and J. Toner. Active nematics on a substrate: Giant number fluctuations and long-time tails. *EPL (Europhysics Letters)*, **62**, 196, 2003.
- [10] Shradha Mishra and Sriram Ramaswamy. [Active Nematics Are Intrinsically Phase Separated](#). *Phys. Rev. Lett.*, **97**, 090602, 2006.
- [11] Vijay Narayan, Sriram Ramaswamy, and Narayanan Menon. [Long-lived Giant Number Fluctuations in a Swarming Granular Nematic](#). *Science*, **317**, 105, 2007.
- [12] Andrey Sokolov and Igor S. Aranson. [Reduction of viscosity in suspension of swimming bacteria](#). *Phys. Rev. Lett.*, **103**, 148101, Sep 2009.
- [13] Luca Giomi, Tanniemola B. Liverpool, and M. Cristina Marchetti. [Sheared active fluids: Thickening, thinning, and vanishing viscosity](#). *Phys. Rev. E*, **81**, 051908, May 2010.
- [14] Suzanne M. Fielding, Davide Marenduzzo, and Michael E. Cates. [Nonlinear dynamics and rheology of active fluids: Simulations in two dimensions](#). *Physical Review E*, **83**(4), 041910, 2011.
- [15] L. Giomi, L. Mahadevan, B. Chakraborty, and M. F. Hagan. [Excitable Patterns in Active Nematics](#). *Phys. Rev. Lett.*, **106**, 218101, 2011.

- [16] L Giomi, L Mahadevan, B Chakraborty, and M F Hagan. Banding, excitability and chaos in active nematic suspensions. *Nonlinearity*, **25**, 2245, 2012.
- [17] Henricus H. Wensink, Jörn Dunkel, Sebastian Heidenreich, Knut Drescher, Raymond E. Goldstein, Hartmut Löwen, and Julia M. Yeomans. [Meso-scale turbulence in living fluids](#). *Proceedings of the National Academy of Sciences*, **109**, 14308–14313, 2012.
- [18] Sumesh P. Thampi, Ramin Golestanian, and Julia M. Yeomans. [Velocity Correlations in an Active Nematic](#). *Phys. Rev. Lett.*, **111**, 118101, 2013.
- [19] Sumesh P. Thampi, Ramin Golestanian, and Julia M. Yeomans. Instabilities and topological defects in active nematics. *EPL (Europhysics Letters)*, **105**, 18001, 2014.
- [20] Sumesh P. Thampi, Ramin Golestanian, and Julia M. Yeomans. [Active nematic materials with substrate friction](#). *Phys. Rev. E*, **90**, 062307, Dec 2014.
- [21] Tong Gao, Robert Blackwell, Matthew A. Glaser, M. D. Betterton, and Michael J. Shelley. Multiscale modeling and simulation of microtubule/motor protein assemblies. *Phys. Rev. Lett.*, **114**, 048101, 2015.
- [22] Aparna Baskaran and M. Cristina Marchetti. [Hydrodynamics of self-propelled hard rods](#). *Phys. Rev. E*, **77**, 011920, Jan 2008.
- [23] John Toner, Yuhai Tu, and Sriram Ramaswamy. [Hydrodynamics and phases of flocks](#). *Annals of Physics*, **318**(1), 170 – 244, 2005. Special Issue.
- [24] John Toner and Yuhai Tu. [Long-range order in a two-dimensional dynamical XY model: How birds fly together](#). *Phys. Rev. Lett.*, **75**, 4326–4329, Dec 1995.

- [25] Tamás Vicsek, András Czirók, Eshel Ben-Jacob, Inon Cohen, and Ofer Shochet. [Novel type of phase transition in a system of self-driven particles](#). *Phys. Rev. Lett.*, **75**, 1226–1229, Aug 1995.
- [26] J. Elgeti, M. E. Cates, and D. Marenduzzo. [Defect hydrodynamics in 2d polar active fluids](#). *Soft Matter*, **7**, 3177–3185, 2011.
- [27] R. Voituriez, J. F. Joanny, and J. Prost. [Generic phase diagram of active polar films](#). *Phys. Rev. Lett.*, **96**, 028102, 2006.
- [28] R. Kemkemer, D. Kling, D. Kaufmann, and H. Gruler. [Elastic properties of nematoid arrangements formed by amoeboid cells](#). *The European Physical Journal E*, **1**(2), 215–225, 2000.
- [29] G Duclos, S Garcia, Yevick HG, and P Silberzan. [Perfect nematic order in confined monolayers of spindle-shaped cells](#). *Soft Matter*, **10**, 2346–2353, 2014.
- [30] David Saintillan and Michael J. Shelley. [Instabilities, pattern formation, and mixing in active suspensions](#). *Physics of Fluids*, **20**, 12, 2008.
- [31] Charles Wolgemuth, Egbert Hoiczyk, Dale Kaiser, and George Oster. [How myxobacteria glide](#). *Current Biology*, **12**, 369, March 2002.
- [32] John Toner and Yuhai Tu. [Flocks, herds, and schools: A quantitative theory of flocking](#). *Phys. Rev. E*, **58**, 4828–4858, Oct 1998.
- [33] Arshad Kudrolli, Geoffroy Lumay, Dmitri Volfson, and Lev S. Tsimring. [Swarming and swirling in self-propelled polar granular rods](#). *Phys. Rev. Lett.*, **100**, 058001, Feb 2008.
- [34] PG de Gennes and J Prost. *The Physics of Liquid Crystals*. Oxford University Press, 2 edition, 1993.

- [35] K. Kruse, J. F. Joanny, F. Jülicher, J. Prost, and K. Sekimoto. [Asters, Vortices, and Rotating Spirals in Active Gels of Polar Filaments](#). *Phys. Rev. Lett.*, **92**, 078101, 2004.
- [36] K. Kruse and F. Jülicher. [Dynamics and mechanics of motor-filament systems](#). *The European Physical Journal E*, **20**, 459–465, 2006.
- [37] J F Joanny, F Jlicher, K Kruse, and J Prost. Hydrodynamic theory for multi-component active polar gels. *New Journal of Physics*, **9**(11), 422, 2007.
- [38] L. M. Pismen. [Dynamics of defects in an active nematic layer](#). *Phys. Rev. E*, **88**, 050502, 2013.
- [39] Tanniemola B. Liverpool and M. Cristina Marchetti. *Hydrodynamics and Rheology of Active Polar Filaments*, pages 177–206. Springer New York, New York, NY, 2008.
- [40] S. A. Edwards and J. M. Yeomans. Spontaneous flow states in active nematics: A unified picture. *EPL (Europhysics Letters)*, **85**, 18008, 2009.
- [41] Shi Xia-qing and Ma Yu-qiang. [Topological structure dynamics revealing collective evolution in active nematics](#). *Nat Commun*, **4**, 1218, 2013.
- [42] Géza Tóth, Colin Denniston, and J. M. Yeomans. [Hydrodynamics of topological defects in nematic liquid crystals](#). *Phys. Rev. Lett.*, **88**, 105504, Feb 2002.
- [43] Felix C. Keber, Etienne Loiseau, Tim Sanchez, Stephen J. DeCamp, Luca Giomi, Mark J. Bowick, M. Cristina Marchetti, Zvonimir Dogic, and Andreas R. Bausch. [Topology and Dynamics of Active Nematic Vesicles](#). *Science*, **345**, 1135, 2014.

- [44] Shuang Zhou, Andrey Sokolov, Oleg D Lavrentovich, and Igor S Aranson. [Living Liquid Crystals](#). *Proc. Nat. Acad. Sci. U.S.A.*, **111**, 1265–1270, 2013.
- [45] M. Kleman and O. D. Lavrentovich. [Topological point defects in nematic liquid crystals](#). *Philosophical Magazine*, **86**, 4117–4137, 2006.
- [46] Lavrentovich O. Kleman M. *Soft Matter Physics: An Introduction*. New York: Springer, 2003.
- [47] O. Lavrentovich. [Topological defects in dispersed words and worlds around liquid crystals, or liquid crystal drops](#). *Liquid Crystals*, **24**(1), 117–126, 1998.
- [48] Thomas Surrey, François Nédélec, Stanislas Leibler, and Eric Karsenti. [Physical Properties Determining Self-Organization of Motors and Microtubules](#). *Science*, **292**, 1167–1171, 2001.
- [49] Luca Giomi, Mark J. Bowick, Xu Ma, and M. Cristina Marchetti. [Defect annihilation and proliferation in active nematics](#). *Phys. Rev. Lett.*, **110**, 228101, 2013.
- [50] P.M. Chaikin and Lubensky T.C. *Principles of Condensed Matter Physics*. Cambridge University Press, 1995.
- [51] S. Chandrasekhar. *Liquid Crystals*. Cambridge University Press, 2 edition, 1992.
- [52] Egbert F. Gramsbergen, Lech Longa, and Wim H. de Jeu. [Landau theory of the nematic-isotropic phase transition](#). *Physics Reports*, **135**(4), 195 – 257, 1986.
- [53] Colin Denniston. [Disclination dynamics in nematic liquid crystals](#). *Phys. Rev. B*, **54**, 6272–6275, Sep 1996.
- [54] Luca Giomi, Mark J Bowick, Prashant Mishra, Rastko Sknepnek, and M Cristina Marchetti. [Defect dynamics in active nematics](#). *Philosophical*

Transactions of the Royal Society of London A: Mathematical, Physical and Engineering Sciences, **372**, 0365, 2014.

- [55] Tanniemola B. Liverpool and M. Cristina Marchetti. [Instabilities of isotropic solutions of active polar filaments](#). *Phys. Rev. Lett.*, **90**, 138102, Apr 2003.
- [56] T. B. Liverpool and M. C. Marchetti. Bridging the microscopic and the hydrodynamic in active filament solutions. *EPL (Europhysics Letters)*, **69**(5), 846, 2005.
- [57] Issac Chuang, Bernard Yurke, Andrew N. Pargellis, and Neil Turok. [Coarsening dynamics in uniaxial nematic liquid crystals](#). *Phys. Rev. E*, **47**, 3343–3356, May 1993.
- [58] A. J. Bray. [Theory of phase-ordering kinetics](#). *Advances in Physics*, **51**(2), 481–587, 2002.
- [59] Harald Pleiner. [Dynamics of a disclination point in smectic-c liquid-crystal films](#). *Phys. Rev. A*, **37**, 3986–3992, May 1988.
- [60] G. Ryskin and M. Kremenetsky. [Drag force on a line defect moving through an otherwise undisturbed field: Disclination line in a nematic liquid crystal](#). *Phys. Rev. Lett.*, **67**, 1574–1577, Sep 1991.
- [61] E. I. Kats, V. V. Lebedev, and S. V. Malinin. [Disclination motion in liquid crystalline films](#). *Journal of Experimental and Theoretical Physics*, **95**(4), 714–727, 2002.
- [62] R. Di Leonardo, S. Keen, F. Ianni, J. Leach, M. J. Padgett, and G. Ruocco. [Hydrodynamic interactions in two dimensions](#). *Phys. Rev. E*, **78**, 031406, Sep 2008.
- [63] Lamb H. *Hydrodynamics, 6th edn*. New York: Dover Publications, 1945.

- [64] David K. Lubensky and Raymond E. Goldstein. [Hydrodynamics of monolayer domains at the airwater interface](#). *Physics of Fluids*, **8**(4), 843–854, 1996.
- [65] A. Bogi, P. Martinot-Lagarde, I. Dozov, and M. Nobili. [Anchoring screening of defects interaction in a nematic liquid crystal](#). *Phys. Rev. Lett.*, **89**, 225501, Nov 2002.
- [66] D. Sventšek and S. Žumer. [Hydrodynamics of pair-annihilating disclination lines in nematic liquid crystals](#). *Phys. Rev. E*, **66**, 021712, Aug 2002.
- [67] Andr M. Sonnet and Epifanio G. Virga. [Flow and reorientation in the dynamics of nematic defects](#). *Liquid Crystals*, **36**(10-11), 1185–1192, 2009.
- [68] I. Dierking, M. Ravnik, E. Lark, J. Healey, G. P. Alexander, and J. M. Yeomans. [Anisotropy in the annihilation dynamics of umbilic defects in nematic liquid crystals](#). *Phys. Rev. E*, **85**, 021703, Feb 2012.
- [69] W. Helfrich. [Alignment-inversion walls in nematic liquid crystals in the presence of a magnetic field](#). *Phys. Rev. Lett.*, **21**, 1518–1521, Nov 1968.
- [70] Alberto de Lózar, Wolfgang Schöpf, Ingo Rehberg, Daniel Sventšek, and Lorenz Kramer. [Transformation from walls to disclination lines: Statics and dynamics of the pincement transition](#). *Phys. Rev. E*, **72**, 051713, Nov 2005.
- [71] Buddhapriya Chakrabarti, Moumita Das, Chandan Dasgupta, Sriram Ramaswamy, and A. K. Sood. [Spatiotemporal rheochaos in nematic hydrodynamics](#). *Phys. Rev. Lett.*, **92**, 055501, Feb 2004.
- [72] Debarshini Chakraborty, Chandan Dasgupta, and A. K. Sood. [Banded spatiotemporal chaos in sheared nematogenic fluids](#). *Phys. Rev. E*, **82**, 065301, Dec 2010.

- [73] S. M. Fielding and P. D. Olmsted. [Spatiotemporal oscillations and rheochaos in a simple model of shear banding](#). *Phys. Rev. Lett.*, **92**, 084502, Feb 2004.
- [74] S. Ganapathy, R. Majumdar and A.K. Sood. [Spatiotemporal dynamics of shear induced bands en route to rheochaos](#). *Eur. Phys. J. B*, **64**, 537–542, 2008.
- [75] Peter D. Olmsted. [Perspectives on shear banding in complex fluids](#). *Rheologica Acta*, **47**, 283–300, 2008.
- [76] P. Manneville. [The transition to turbulence in nematic liquid crystals](#). *Molecular Crystals and Liquid Crystals*, **70**(1), 223–250, 1981.
- [77] Larson R. G. and Mead D. W. [The ericksen number and Deborah number cascades in sheared polymeric nematics](#). *Liquid Crystals*, **15**(2), 151–169, 1993.
- [78] Luca Giomi. [Geometry and topology of turbulence in active nematics](#). *Phys. Rev. X*, **5**, 031003, 2015.
- [79] Peter D. Olmsted and C.-Y. D. Lu. [Phase separation of rigid-rod suspensions in shear flow](#). *Phys. Rev. E*, **60**(4), 4397–4415, 1999.
- [80] E J Hemingway, Ananyo Maitra, Shiladitya Banerjee, M. Cristina Marchetti, Sriram Ramaswamy, Suzanne M. Fielding, and Michael E. Cates. [Active Viscoelastic Matter: From Bacterial Drag Reduction to Turbulent Solids](#). *Physical Review Letters*, **114**(9), 098302, 2015.
- [81] Dragan Huterer and Tanmay Vachaspati. [Distribution of Singularities in the Cosmic Microwave Background Polarization](#). *Phys. Rev. D*, **72**, 043004, 2005.
- [82] Sumesh P. Thampi, Ramin Golestanian, and Julia M. Yeomans. [Vorticity, defects and correlations in active turbulence](#). *Philosophical Transactions*

of the Royal Society of London A: Mathematical, Physical and Engineering Sciences, **372**, 0366, 2014.

- [83] Salima Rafai, Levan Jibuti, and Philippe Peyla. [Effective viscosity of microswimmer suspensions](#). *Phys. Rev. Lett.*, **104**, 1–4, 2010.
- [84] Poul M. Bendix, Gijsje H. Koenderink, Damien Cuvelier, Zvonimir Dogic, Bernard N. Koeleman, William M. Briehar, Christine M. Field, L. Mahadevan, and David A. Weitz. [A Quantitative Analysis of Contractility in Active Cytoskeletal Protein Networks](#). *Biophys. J.*, **94**(8), 3126–3136, 2008.
- [85] Jörn Dunkel, Sebastian Heidenreich, Knut Drescher, Henricus H. Wensink, Markus Bär, and Raymond E. Goldstein. [Fluid Dynamics of Bacterial Turbulence](#). *Phys. Rev. Lett.*, **110**, 228102, 2013.
- [86] H. Stark and T. C. Lubensky. [Poisson-bracket approach to the dynamics of nematic liquid crystals](#). *Phys. Rev. E*, **67**(6), 061709, Jun 2003.
- [87] N. Liron and S. Mochon. [Stokes flow for a stokeslet between two parallel flat plates](#). *Journal of Engineering Mathematics*, **10**(4), 287–303.
- [88] Tommaso Brotto, Jean-Baptiste Caussin, Eric Lauga, and Denis Bartolo. [Hydrodynamics of Confined Active Fluids](#). *Phys. Rev. Lett.*, **110**, 038101, Jan 2013.
- [89] Sriram Ramaswamy and Madan Rao. Active-filament hydrodynamics: instabilities, boundary conditions and rheology. *New Journal of Physics*, **9**(11), 423, 2007.
- [90] Hugo Wioland, Francis G. Woodhouse, Jörn Dunkel, John O. Kessler, and Raymond E. Goldstein. [Confinement Stabilizes a Bacterial Suspension into a Spiral Vortex](#). *Phys. Rev. Lett.*, **110**, 268102, Jun 2013.

- [91] Elias Putzig, Gabriel S. Redner, Arvind Baskaran, and Aparna Baskaran. [Instabilities, defects, and defect ordering in an overdamped active nematic.](#) *Soft Matter*, **12**, 3854–3859, 2016.
- [92] Anand U. Oza and Jörn Dunkel. Antipolar ordering of topological charges and universality in active liquid crystals. *arXiv:1507.01055*, 2016.
- [93] Sumesh P. Thampi, Amin Doostmohammadi, Ramin Golestanian, and Julia M. Yeomans. Intrinsic Free Energy in Active Nematics. *arXiv:1510.06929*, 2015.
- [94] Doostmohammadi, Amin and Adamer, Michael F. and Thampi, Sumesh P. and Yeomans, Julia M. [Stabilization of active matter by flow-vortex lattices and defect ordering.](#) *Nat Commun*, **7**, 10557, feb 2016.
- [95] Großmann, Robert, Pawel Romanczuk, Markus Bar, and Lutz Schimansky-Geier. [Vortex Arrays and Mesoscale Turbulence of Self-Propelled Particles.](#) *Phys. Rev. Lett.*, **113**, 258104, Dec 2014.
- [96] Sebastian Heidenrieck, John Dunkel, Sabine H.L. Klapp, and Bär, Markus. Hydrodynamic length-scale selection and effective viscosity in microswimmer suspensions. *arXiv:1509.08661*, 2015.
- [97] Kruse, K., Joanny, J. F., Jülicher, F., Prost, J., and Sekimoto, K. [Generic theory of active polar gels: a paradigm for cytoskeletal dynamics.](#) *Eur. Phys. J. E*, **16**(1), 5–16, 2005.
- [98] Dieter Forster. [Microscopic Theory of Flow Alignment in Nematic Liquid Crystals.](#) *Phys. Rev. Lett.*, **32**, 1161–1164, May 1974.
- [99] N Kuzuu and M Doi. Constitutive Equation for Nematic Liquid Crystals under Weak Velocity Gradient Derived from a Molecular Kinetic Equation. II. –Leslie Coefficients for Rodlike Polymers. *Journal of the Physical Society of Japan*, **53**(3), 1031–1038, March 1984.

- [100] Antony N. Beris and Brian J. Edwards. *Thermodynamics of Flowing Systems: with Internal Microstructure*. Oxford University Press, 1 edition, 1994.
- [101] A. Michelson. [Phase diagrams near the Lifshitz point. I. Uniaxial magnetization](#). *Phys. Rev. B*, **16**, 577–584, Jul 1977.
- [102] Jörn Dunkel, Sebastian Heidenreich, Markus Bär, and Raymond E Goldstein. Minimal continuum theories of structure formation in dense active fluids. *New Journal of Physics*, **15**(4), 045016, 2013.
- [103] M. E. Cates, D. Marenduzzo, I. Pagonabarraga, and J. Tailleur. [Arrested phase separation in reproducing bacteria creates a generic route to pattern formation](#). *Proceedings of the National Academy of Sciences*, **107**(26), 11715–11720, 2010.
- [104] Oleg D. Lavrentovich. [Active colloids in liquid crystals](#). *Current Opinion in Colloid & Interface Science*, **21**, 97–109, 2016.

Prashant Mishra

Curriculum Vitae

116 Remington Ave, Apt D
Syracuse NY 13210, United States of America
☎ mobile +1 315 751 0888
✉ pmishra@syr.edu

Education

- Ph.D. **Theoretical Soft Condensed Matter Physics**, *Physics Department, Syracuse University*, Syracuse NY, USA, August 2017.
- Masters **Dual BS-MS in Physics**, *Indian Institute of Science Education & Research (IISER)*, Mohali, India, graduated with Distinction in May 2012.

Teaching Experience

- **Certificate in University Teaching(CUT) by Future Professoriate Program(FPP)(April 2017):**
 - FPP provides structured professional development experience for aspiring faculty.
 - Selected candidates go through FPP seminar and workshops and get CUT after fulfilling departmental requirements.
- **Teaching Mentor (August 2016-Present):**
 - Selected for excellence in teaching and overall graduate study.
 - Participated in the development and implementation of TA Program activities throughout the academic year.
- **TA-Science and Computers (Fall 2016):**
 - Helped students with developing understanding the power of computation to solve physical problems.
 - Students developed simulations with visual animation for various physical systems like pendulum, strings etc.
- **Grader-Mathematical Methods (Fall 2016):**
 - Provided feedbacks to the fellow graduate students on their assignments in solving various PDEs analytically and computationally.
- **TA-General Physics I(Honors & Majors) (Spring 2016, Fall 2015, Spring 2015, Fall 2014, Fall 2013):**
 - Conducted recitation classes with the goal of providing them the insights of using the concepts learned in class into the daily life problems.
 - Encouraged the group discussion and collective problem solving activities.
 - Focused on conceptual learning rather than numerical solutions.
 - Held numerous office hours in order to better help students in understanding the class material.
 - Directed some of the students towards the research fields they were suitable for in the future.
- **Lab Instructor- Astronomy 101 Lab (Summer 2015):**
 - Conducted astronomy labs and guided students through The NAAP simulator.
- **Lab TA- General Physics I Lab(Honors & Majors) (Fall 2014, Fall 2013):**
 - Conveyed the power of experiments in any scientific field, by letting them test the theories they learned in the class.
 - Asked them to question and validate any new result they got instead of just writing that on their workbook.
 - Conducted group experiments and asked conceptual questions to each group member so that everyone is on board.
- **Lab TA- General Physics II Lab(Electricity, Magnetism and Light)(Spring 2014):**
 - Motivated students and made them understand the importance and power of Electromagnetism.
 - Let them know how experiments they were doing in lab relate to the work they do in their respective departments e.g. in Electron Microscope in medical fields, Ion channels in biological systems etc.
- **TA- General Physics I (Spring 2013):**
 - Held recitations for 4 sections and guided students through basic mechanics concepts and problems based on them.
- **Lab TA- Astronomy 101 (Fall 2012):**
 - Outdoor astronomy labs with star gazing.
 - Introduced them to the power of estimation in physics.

Teaching Interests:

- General Physics I & II Theory and Labs
- Advanced Course: Computational Physics for Advanced Undergraduates
- Proposed Course: Introductory Soft Matter Physics

Scholarships

- **Certificate in University Teaching** (April 2017) from Future Professoriate Program(FPP) Graduate School, Syracuse University
- **Future Professoriate Program(FPP) fellowship** (August 2015-Present) Graduate School, Syracuse University
- **Henry Levinstein Fellowship** (Summer 2013) for the academic excellence and promise of excellence in research at Physics Department, Syracuse University
- **INSPIRE Fellowship** (2007–2012) from DST(Department of Science & Technology India)

Research Experience

Research Assistant in Prof. Cristina Marchetti's Group May 2013 onward, Physics Department, Syracuse University, Syracuse, USA, Homepage: <https://mcmarche.expressions.syr.edu/>

Publications:

- **Negative stiffness and modulated states in active nematics**, Soft Matter, 2016,12, 8214-8225,together with Pragma Srivastava and M. Cristina Marchetti.
- **Correlation lengths in hydrodynamic models of active nematics**, Soft Matter, 2016,12, 7943-7952, together with Ewan J. Hemingway, M. Cristina Marchetti and Suzanne M. Fielding.
- **Defect Dynamics in Active Nematics**, Phil. Trans. R. Soc. A:2014372 20130365;DOI: 10.1098/rsta.2013.0365, together with Luca Giomi, Mark J Bowick,Rastko Sknepnek and M Cristina Marchetti.
- **Interaction of Silver Nanoparticles with a Lipid Bilayer Membrane and a Polymer Mesh**, May 2012, Prashant Mishra, unpublished dissertation to complete the BS-MS degree supervised by Dr Kavita Dorai, IISER Mohali

Presentations:

- **Defect dynamics and ordering in compressible active nematics**, APS March Meeting 2016, March 2016, Baltimore, Maryland, US (oral presentation)
- **Defect dynamics in active nematics**, APS March Meeting 2014, March 2014, Denver, CO, US (oral presentation)
- **Negative stiffness and modulated states in compressible active nematics**, International Conference Active and Smart Matter: a New frontier in Science and Engineering, June 2016, Syracuse university, Syracuse, NY (poster presentation)
- **Defect proliferation in active nematic suspension**, 14th NY Complex Matter Workshop, December 2014, Cornell University, Cornell, NY (poster presentation)
- **Defect proliferation in active nematic suspension**, Stevenson Biomaterials Lecture Series 2014, October 2014, Syracuse university, Syracuse, NY (poster presentation)
- **13th NY Complex Matter Workshop**, December 2012, Syracuse University, Syracuse, NY (attended)
- **Unifying Concepts in Materials: JA Krumhansl School & Symposium 2012**, December 2011, NCBS-TIFR, Bangalore, India (attended)

Research Interests:

- Theoretical and Computational Soft Condensed Matter Physics

Computer skills:

- **Programming languages:** MATLAB , Mathematica, Python, C++, C, R
- **Tools:** L^AT_EX, MS Office

References

Prof. Cristina Marchetti(Advisor)

Physics Department
Syracuse University
Syracuse (NY), 13244-1130

Tel: +1-315-443-2581
E-mail: mcmarche@syr.edu

Prof. Peter R. Saulson

Physics Department
Syracuse University
Syracuse (NY), 13244-1130

Tel: +1-315-443-5994
E-mail: psaulson@syr.edu

Prof. Britton Plourde(Faculty Mentor for FPP)

Physics Department
Syracuse University
Syracuse (NY), 13244-1130

Tel: +1-315-443-8967
E-mail: bplourde@syr.edu

Prof. Mark Bowick

Physics Department
Syracuse University
Syracuse (NY), 13244-1130

Tel: +1-315-443-5979
E-mail: mjbowick@syr.edu